University of Windsor
Scholarship at UWindsor

Electronic Theses and Dissertations | Theses, Dissertations, and Major Papers

10-5-2017

A MEMS BASED MICROWAVE PIXEL FOR UWB RADAR BASED 3-D DIAGNOSTIC IMAGING

Sujitha Vejella
University of Windsor

Follow this and additional works at: https://scholar.uwindsor.ca/etd

Recommended Citation
Vejella, Sujitha, "A MEMS BASED MICROWAVE PIXEL FOR UWB RADAR BASED 3-D DIAGNOSTIC IMAGING" (2017). *Electronic Theses and Dissertations*. 7303.
https://scholar.uwindsor.ca/etd/7303

This online database contains the full-text of PhD dissertations and Masters' theses of University of Windsor students from 1954 forward. These documents are made available for personal study and research purposes only, in accordance with the Canadian Copyright Act and the Creative Commons license—CC BY-NC-ND (Attribution, Non-Commercial, No Derivative Works). Under this license, works must always be attributed to the copyright holder (original author), cannot be used for any commercial purposes, and may not be altered. Any other use would require the permission of the copyright holder. Students may inquire about withdrawing their dissertation and/or thesis from this database. For additional inquiries, please contact the repository administrator via email (scholarship@uwindsor.ca) or by telephone at 519-253-3000ext. 3208.

A MEMS BASED MICROWAVE PIXEL FOR UWB RADAR BASED 3-D DIAGNOSTIC IMAGING

By

Sujitha Vejella

A Thesis
Submitted to the Faculty of Graduate Studies
through the Department of Electrical and Computer Engineering
in Partial Fulfillment of the Requirements for
the Degree of Master of Applied Science
at the University of Windsor

Windsor, Ontario, Canada

2017

© 2017 **Sujitha Vejella**

A MEMS BASED MICROWAVE PIXEL FOR UWB RADAR BASED 3-D DIAGNOSTIC IMAGING

by

Sujitha Vejella

APPROVED BY:

S. Das
Department of Civil and Environmental Engineering

K. Tepe
Department of Electrical and Computer Engineering

S. Chowdhury, Advisor
Department of Electrical and Computer Engineering

September 18, 2017

DECLARATION OF ORIGINALITY

I hereby certify that I am the sole author of this thesis and that no part of this thesis has been published or submitted for publication.

I certify that, to the best of my knowledge, my thesis does not infringe upon anyone's copyright nor violate any proprietary rights and that any ideas, techniques, quotations, or any other material from the work of other people included in my thesis, published or otherwise, are fully acknowledged in accordance with the standard referencing practices. Furthermore, to the extent that I have included copyrighted material that surpasses the bounds of fair dealing within the meaning of the Canada Copyright Act, I certify that I have obtained a written permission from the copyright owner(s) to include such material(s) in my thesis and have included copies of such copyright clearances to my appendix.

I declare that this is a true copy of my thesis, including any final revisions, as approved by my thesis committee and the Graduate Studies office and that this thesis has not been submitted for a higher degree to any other University or Institution.

ABSTRACT

A MEMS-based microwave Pixel has been developed for use with an Ultra-wideband (UWB) radar probe for high-resolution 3-D non-contact, non-ionizing tomographic diagnostic imaging of the thorax. In the proposed system, an UWB radar transmits a 400 ps duration pulse in the frequency range of 3.1 GHz to 5.1 GHz. The transmitted pulse penetrates through the tissues and is partially reflected at each tissue interface characterized by a complex permittivity change. A suitable microwave lens focuses the reflected wavefront on a 2-D array of MEMS-based microwave Pixels to illuminate each Pixel to a tiny 2-D section of the reflected wavefront. Each Pixel with a footprint area of 595 x 595 μm^2 is designed to have 144 parallel connected microfabricated inductors, each with an inductance of 12.439 nH, and a single 150 µm×150 µm microfabricated deformable diaphragm based variable capacitor to generate a voltage which is the dielectric signature of the respective tissue section. A 2-D array of such Pixels can be used to generate a voltage map that corresponds to the dielectric property distribution of the target area. The high dielectric contrast between the healthy and diseased tissues, enable a high precision diagnostics of medical conditions in a non-invasive non-contact manner. This thesis presents the analytical design, 3-D finite element simulation results, and a fabrication process to realize the proposed microwave imaging Pixel. The proposed Pixel with total inductance of 86.329 pH and capacitance tuning range of 1.68:1, achieved a sensitivity of 4.5 aF/0.8 $\mu A.m^{-1}$ to generate tomographic coronal imaging slices of human thorax deep upto 4.2 cm enabling a theoritical lateral resolution of 0.59 mm.

DEDICATION

To my parents

The reason for what I am today, thank you for your constant support and encouragement to follow my dreams. Thank you for teaching me to believe in lord Sai Baba who gave me a lot of strength because faith in God is not just a belief it is a confidence.

To my husband

Without whom I won't be able to complete this thesis. Thanks for your love, understanding, overwhelming support morally and financially.

To my sister & In-laws

Thank you for being with me, all your encouragement made this thesis possible.

ACKNOWLEDGEMENTS

I would like to give my sincere thanks to my supervisor Prof. Dr. Chowdhury. Thank you for giving me the opportunity to carry out my thesis under your supervision and I really enjoyed the way you guide me throughout this project. Under your supervision, I understood what actually a research is and your words to enjoy the research, always encouraged me. The skills I gained through this master's program, enhanced my ability to think towards a problem analyzing and solving.

I would like to thank my committee members, Prof. Dr. Tepe, Prof. Dr. Das and thank you for all the comments and suggestions on my project. Prof. Dr. Rashid for allowing me to use the RCIM lab facility. I specially want to say thank you to Frank for helping me out in few lab experiments and for his administrative support. I want to give my heartful thanks to Andria and Lorraine for their administrative support. I would like to acknowledge the support, motivation, and ideas from my lab mates, colleagues, and friends Weiying, Rayyan, Varshitha, and Sreejit. I am very thankful to you all, you have been a moral support to me.

I would like to extend my thanks to my friends Sreya, Priya, Sindhu, Kalyan, Hemanth, Suresh, Madhu, Swathi and Sravya who supported me through out my thesis. I would like to thank each and every one who directly or indirectly had an influence in the completion of this thesis.

TABLE OF CONTENTS

DECLARATION OF ORIGINALITY iii

ABSTRACT iv

DEDICATION v

ACKNOWLEDGEMENTS vi

LIST OF TABLES ix

LIST OF FIGURES x

LIST OF APPENDICES xiv

LIST OF ABBREVIATIONS xv

NOMENCLATURE xvii

Chapter 1 INTRODUCTION 1

1.1 Goals 1

1.2 Background 5

1.2.1. Existing technologies 5

1.2.2. Need for new-transformative in medical imaging systems 7

1.3. Principal Results 8

1.4. Organization of Thesis 11

Chapter 2 UWB RADAR FOR MICROWAVE IMAGING 13

2.1. UWB Radar for Medical Application 13

2.2 Microwave Imaging for Human Tissues 17

2.2.1. Safety concern 17

2.2.2. Tissue properties 19

2.2.3. Contrast between healthy tissues and cancerous tumors 24

2.3. UWB Radar system with Proposed Microwave Pixel Array 25

Chapter 3 MEMS MICROWAVE PIXEL DESIGN 28

3.1. Microwave Pixel Operation 28

3.2 Pixel Inductor /Antenna Design 29

3.2.1. Equivalent circuit parameters of the loop inductor 30
3.3. Pixel Capacitor Design 34
3.3.1. Mathematical formulation of the Pixel capacitor operation 37

Chapter 4 HUMAN THORAX IMAGING 40
4.1. Human Thorax Anatomy 40
4.2. Analytical Model to Determine the Propagation Loss 41
4.3. FDTD Simulation of Thorax Model 47
4.3.1. Analytical model validation 50

Chapter 5 MEMS PIXEL DESIGN FOR HUMAN THORAX IMAGING 51
5.1. Determination of Power Levels that to be Detected by the Proposed Pixel 51
5.2 MEMS Microwave Pixel Design Specifications 55
5.2.1. Circuit Operation 56
5.2.2. Design specifications of Pixel inductor 61
5.2.3. Design specifications of the Pixel capacitor 67

Chapter 6 FABRICATION OF PROPOSED MICROWAVE PIXEL 77
6.1. Fabrication steps 77

Chapter 7 CONCLUSIONS AND FUTURE WORK 89
7.1. Discussions and Conclusions 89
7.2. Future work 91

APPENDICES 94

Appendix A MATLAB® code for UWB signal attenuation in human tissues 94

REFERENCES/BIBLIOGRAPHY 99

VITA AUCTORIS 105

LIST OF TABLES

Table 1.1 Electrical property contrast for successive tissues in human thorax model at 4.1 GHz. 10

Table 2.1 General public exposure level to EM fields. 19

Table 4.1 Complex permittivity of few of the human thorax tissues in UWB frequency range. 42

Table 4.2 Propagation and echo time of UWB signal through thorax model. 48

Table 5.1 Case 1: Power transmitted P_t = 5 mW. 54

Table 5.2 Case 2: Power transmitted P_t = 50 mW. 54

Table 5.3 Case 3: Power transmitted P_t = 500 mW. 55

Table 5.4. Resonant frequency at different N values. 58

Table 5.5 Comparison of loop Inductance, loop resistance and loop current of various combinations for the same total area at 4.1 GHz frequency. 65

Table 5.6 Design parameters of Pixel inductor. 66

Table 5.7 Pull-in voltage at different diaphragm thickness. 67

Table 5.8 Pull-in voltage with respect to airgap. 68

Table 5.9 State-of-the-art capacitance sensing readout circuits. 69

Table 5.10 Pixel capacitor design parameters. 70

Table 5.11 Material properties. 70

Table 5.12 Pixel voltage and capacitance corresponding to the tissue interface reflections at 5 mW,50 mW and 500 mW. 76

Table 7.1 Pixel detectability analysis for transmit power of 5mW, 50mW, 500mW. 90

LIST OF FIGURES

Figure 1.1. Statistics of leading causes of death in Canada [1]. 2

Figure 1.2. MEMS Microwave Pixel. 3

Figure 1.3. Basic Principle of medical diagnostic imaging. 6

Figure 1.4. Estimated Pixel array size of 14 × 14 inch to image FOV of 32.8 × 32.8 cm. 9

Figure 2.1. a) & b) Permittivity vs Frequency and Conductivity vs Frequency curves for few tissues of human digestive system, c) & d) Permittivity vs Frequency and Conductivity vs Frequency curves for few tissues of human brain. 22

Figure 2.2. a) & b) Permittivity vs Frequency and Conductivity vs Frequency curves for few tissues around cervix in women reproductive system, c) & d) Permittivity vs Frequency and Conductivity vs Frequency curves for few tissues of human thorax. 23

Figure 2.3. Frequency dependence of relative permittivity and conductivity for skin, tumor and healthy breast tissue [27]. 24

Figure 2.4. Block diagram of UWB radar system. 26

Figure 2.5. Sub-wavelength capturing of incident signal at different time intervals. 27

Figure 2.6. Conceptual 3D tomographic image generation using the MEMS based Pixel array. 27

Figure 3.1. MEMS Microwave Pixel. 29

Figure 3.2. a) Equivalent circuit of loop inductor, b) Loop inductor with labeled physical parameters. 31

Figure 3.3. a) Equivalent inductance of the loop inductor as a function of number of turns, b) Equivalent resistance of the loop inductor as a function of number of turns. 33

Figure 3.4. a) Equivalent inductance of the loop inductor as a function of loop length, b) Equivalent resistance of the loop inductor as a function of loop length. 33

Figure 3.5. a) Equivalent inductance of the loop inductor as a function of conductor width, b) Equivalent capacitance of the loop inductor as a function of conductor

width, c) Equivalent resistance of the loop inductor as a function of conductor width. 34

Figure 3.6. a) Top view of MEMS Pixel capacitor, b) Cross sectional view of the capacitor, c) Electrical equivalent circuit of the Pixel capacitor..... 36

Figure 4.1. Horizontal section of human thorax. 41

Figure 4.2. Human thorax model indicating the depth of the tissues [35]. 41

Figure 4.3. Gaussian pulse representation in (a) time domain and,(b) frequency domain..... 43

Figure 4.4. a) Human Thorax model, b) A wave propagation path with different dielectric materials analogues to transmission line model with varying impedance [34]. 45

Figure 4.5. Mathematical model predicted one -way attenuation of UWB signal propagating into human thorax model at 4.1 GHz. 46

Figure 4.6. Analytical attenuation results for human thorax model at different interfaces with frequency. 46

Figure 4.7. Simulation setup of human thorax model in Remcom® XFdtd®. 47

Figure 4.8. Magnetic field distribution. a) at t=0.205 ns, b) at t=0.35 ns, c) at t=0.97 ns, d) t=1.4 ns..... 49

Figure 4.9. Analytical and simulated results for attenuation of UWB signal propagating into the human thorax model. 50

Figure 5.1. Thorax model assuming heart as a sphere of diameter 12 cm..... 53

Figure 5.2. Normalized backscattered RCS for a perfectly conducting sphere [37]. 53

Figure 5.3. Electrical equivalent circuit of the proposed microwave Pixel..... 57

Figure 5.4. Frequency response of the loop inductors with different N values. . 57

Figure 5.5. Equivalent circuit of wideband loop inductor..... 59

Figure 5.6. Frequency response of the loop inductor with and without damping resistance. 60

Figure 5.7. Voltage generated across the loop inductor, shunted with a resistance, as a function of N..... 62

Figure 5.8. Parallel crossed loops with their current direction..... 63

Figure 5.9. 12×12 Sub-Pixel matrix showing their connections (dimensions are not to scale). 64

Figure 5.10. Diaphragm deflection with voltage, a) at different diaphragm thickness, b) at different airgap. 67

Figure 5.11. a) Pull-in voltage curve of the Pixel capacitor, b) Deflection of the diaphragm at pull-in voltage. 69

Figure 5.12. a) Diaphragm deflection when 1mV AC voltage at 45.75 KHz (mode1) is applied, b) Diaphragm deflection when 1mV AC voltage at 101.08 KHz (mode 2) is applied, c) IntelliSuite® capture showing Pixel capacitor's three modes of frequency. 71

Figure 5.13. The deflection of the diaphragm when applied AC voltage (1 mV amplitude) is at, a) 3.1 GHz, b) 4.1 GHz, c) 5.1 GHz. 72

Figure 5.14. Diaphragm deflection with inductor induced AC voltage. 73

Figure 5.15. Capacitance generated with loop inductor induced voltage. 74

Figure 5.16. The voltage induced across the Pixel capacitor corresponding to the reflections from skin/fat, fat/muscle, muscle/cartilage, cartilage/lung and lung/heart when the transmit power is, a) 5 mW, b) 50 mW, c) 500 mW. 75

Figure 6.1. Glass wafer after cleaning. 77

Figure 6.2. Metal deposition. 78

Figure 6.3. a) Spin on photoresist & exposure to UV with contact mask aligner, b) Photoresist develop, c) Ion beam etch of gold and titanium layers, d) Strip photoresist. 79

Figure 6.4. Cross-sectional view, a) Spin deposited BCB, b) after Planarization. 79

Figure 6.5. a) Photoresist exposure to UV, b) Photoresist develop, c) RIE etch of BCB, d) Removal of photoresist. 80

Figure 6.6. a) Deposition of SiO_2, b) Photoresist and UV exposure, c) Pattern photoresist, d) RIE etch of sacrificial layer. 81

Figure 6.7. a) Deposition of 20 nm chromium, b) E-beam evaporation of gold, c) Photoresist spin and UV exposure, d) Photoresist develop, e) Etching of gold and chromium, f) Removal of photoresist. 82

Figure 6.8. Release of diaphragm. 83

Figure 6.9. Silicon wafer spin deposited with BCB at the bottom, b) RIE etch of BCB layer. 84

Figure 6.10. a) Deposition of SiO_2, b) Spin photoresist and UV exposure, c) Pattern photoresist, d) Removal of photoresist. 84

Figure 6.11. a) Deposition of chromium as seed layer, b) E-beam evaporation of gold, c) Spin photoresist and UV exposure, d) Pattern photoresist, e) patterning of gold, f) Strip photoresist. 85

Figure 6.12. Release of 12×12 Pixel inductor array. 86

Figure 6.13. Deposition of Fe-Co-B film. 87

6.14. a) Spin photoresist and UV exposure with contact mask aligner, b) Develop photoresist, c) Etch magnetic core, d) Strip photoresist. 88

Figure 6.15. BCB- BCB adhesive bonding. 88

Figure 7.1. Laser light reflection from a) a non-deflected diaphragm b) a deflected diaphragm. 92

LIST OF APPENDICES

Appendix A. MATLAB® code for UWB signal attenuation in human tissues ···94

LIST OF ABBREVIATIONS

UWB – Ultra-wideband

Radar – Radio Detection and Ranging

MEMS – Microelectromechanical Systems

3-D – Three Dimensional

EM – ElectroMagnetic

DC – Direct Current

AC – Alternating Current

RF – Radio Frequency

BW - Bandwidth

RMS - Root Mean Square

RCS - Radar Cross-Section

FDTD - Finite-Difference Time-Domain method

FEM - Finite Element Method

MRI – Magnetic Resonance Imaging

CT - Computed Tomography

PET - Positron Emission Tomography

PET-CT - Positron Emission Tomography- Computed Tomography

SPECT - Single Photon Emission Computed Tomography

FCC - Federal Communications Commission

ECG – Electrocardiogram

MWT - Microwave Tomography

HR - Heart Rate

VHR - Variable Heart Rate

SAR - Specific Absorption Rate

ICNIRP - International Commission on Non-Ionizing Radiation Protection

ADC - Analog to Digital Converter

DSP - Digital Signal Processer

VCO - Voltage-Controlled Oscillator

PRP - Pulse Repetition Period

BCB - Benzo-Cyclo-Butene

Spice – Simulation Program with Integrated Circuit Emphasis

DI – De-ionized water

RIE - Reactive Ion Etch

PECVD - Plasma-Enhanced Chemical Vapor Deposition

CPD - Critical Point Drying

TEOS – Tetraethoxysilane

SCCM - Standard Cubic Centimeters per Minute

FOV - Field of View

NOMENCLATURE

f_H = Upper frequency of the -10dB emission point

f_L = Lower frequency of the -10dB emission point

W = Energy of the photon

h = Planck's constant

f = Frequency of the EM field

λ = Wavelength of EM wave

ε_{r_i} = Complex permittivity

ϕ = Magnetic flux

V_{oc} = Open circuit voltage of the loop inductor

H_{rms} = RMS value of the magnetic field intensity

μ_0 = vacuum permeability

μ_r = Relative permeability of the medium

N = Number of turns

A = Area of each turn

θ = Angle between the magnetic flux lines and the plane normal to the loop surface.

R_{AC} = AC resistance of the loop inductor

R_{Rad} = Radiation resistance

R_{DC} = Conductor. resistance

L_{loop} = Inductance of the square loop

L_{wire} = Inductance of the conductor

C_{loop} = Parasitic capacitance of the loop.

w = Length of the square loop

l = Length of the winding

d = Width of the conductor.

ρ = Resistivity of the conductor

c = Velocity of EM wave in free space

C_{MEMS} = Capacitance of the MEMS variable capacitor

R_{series} = Resistance of the capacitive sensor

V_{DC} = DC bias voltage applied to MEMS capacitor

V_{AC} = AC voltage applied to MEMS capacitor

ε_0 = Permittivity of vacuum

ε_r = Relative Permittivity

ε_{ri} = Permittivity of the insulating layer

A_e = Area of the electrode

d_c = Thickness of the diaphragm

d_i = Thickness of the insulation layer

g = Thickness of the air gap

x = Deflection of the membrane

$F_{electrostatic}$ = Electrostatic force

V_{rms} = RMS voltage

ω = Angular frequency

T_i = Transmission matrix

γ = Propagation constant

G_1 = Gain of transmitting antenna

P_t = Transmit power

R_1 = Distance from the human target to transmit antenna

σ = Radar cross-section

A_t = Projected area of the target

Γ = Reflectivity of the target

G_t = Antenna-like gain of the target.

z = Propagation impedances

R_2 = Distance from microwave Pixel array to the human target

Γ = Reflectivity of the target

L = Propagation loss

R_d = Damping resistance

I_{loop} = Loop current

E = Young's modulus

ν = Poisson ratio

ΔC = Capacitance change

CHAPTER 1

INTRODUCTION

This chapter presents the objectives of this thesis, explaining the importance of the present work and its outcome. A summary of present imaging techniques and the need for new transformative medical imaging systems is clearly explained. The operating principle of a proposed novel microwave imaging Pixel, a MEMS transducer, designed to integrate with an UWB radar system for medical tomographic imaging is presented. Next to this, the principal results of this research work are listed and finally, the thesis organization is presented.

1.1 Goals

According to the cause of death database of Statistics Canada [1], cancer being the lead cause with a percentage of 29.8, heart diseases and heart stroke accounts 19.8% and 5.3%. The bar chart depicting these numbers is shown in Figure 1.1. The survival rate in the case of top four diseases can be increased by an effective diagnostic imaging system, which is quick with real time results, is less expensive and is operable at doctor's room. Moreover, an imaging system which is completely safe with no ionization is essential for frequent screening programs aiming for early detection of any abnormalities.

This goal can be realized by combining radar techniques with microwave technology resulting in a promising new imaging technique called microwave radar tomography [2]. Tomography is defined as any method which sectionalize the

target volume at different depths to get a better insight of the target. The motivation behind this research comes from the fact that microwaves can travel through the human tissues as a function of tissue electrical properties like permittivity and conductivity. Any change in these properties alters the absorption, transmission, reflection, and refraction of the microwave signal when passed through that tissue. The specific goal of this thesis is to design and simulate a microwave imaging transducer, named as a microwave imaging Pixel, that captures the spatial distribution of the reflected microwave energy and affects a capacitance change corresponding to the strength of the signal incident on the Pixel.

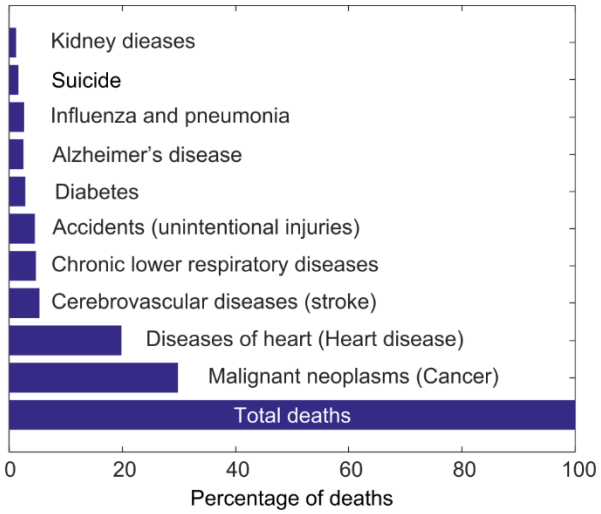

Figure 1.1. Statistics of leading causes of death in Canada [1].

The basic operating principle of the developed MEMS microwave imaging Pixel can be explained using a conceptual geometry as shown in Figure 1.2. The Pixel is comprised of a microfabricated spiral inductor (acting as a small loop antenna) and a microfabricated vibrating diaphragm variable capacitor shown in

Figure 1.2. The sensor is operated when the microwave radiation, reflected from the human tissues, is picked up by the microfabricated spiral inductor. This generates a voltage across the inductor corresponding to the magnetic energy level of the reflected portion of the wavefront. This voltage is applied across the electrodes of a MEMS capacitive sensor formed by a deformable diaphragm and a fixed backplate. Being charged with a constant DC bias voltage, the capacitance of the device is changed proportional to the RMS (root mean square) voltage of the radiated signal captured by the Pixel [3]. This capacitance change is converted to a voltage signal using an appropriate transimpedance amplifier as shown in Figure 1.2.

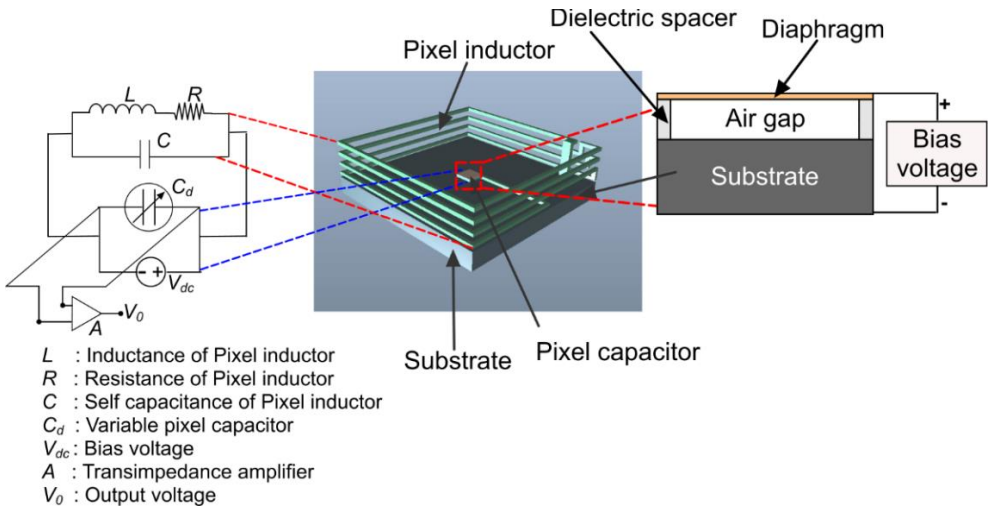

Figure 1.2. MEMS Microwave Pixel.

The objectives of this thesis are to develop a mathematical model for determining the attenuation and duration of the microwave signal passing through the human tissues while considering various propagation losses in the tissues. To record the spatial distribution of the reflected microwave energy, a MEMS based microwave Pixel, that collects weak microwave signals and generates a

capacitance in response to the signal strength of the reflected signal is designed. The microwave Pixel operation is simulated using MATLAB®, OrCAD® PSpice®, and InstelliSuite®.

In summary, this thesis investigates the design and development of novel microwave Pixel for human thorax imaging, specifically, the goals of this thesis are as follows:

1) To design a MEMS based microwave Pixel that can be used as an integral part of an ultra-wideband radar to generate a tomographic image of the human thorax. The developed Pixel device should be compact in size (far less than the wavelength of operation), sensitive enough to collect the weak reflections from the deeper human tissues and should be frequency independent over the UWB frequency range of 3.1 GHz – 5.1 GHz.
2) To study the effect of microwave radiation on various human tissues and to understand their frequency dependent electrical characteristics like complex permittivity and conductivity using the models developed in [24], [25], [26].
3) To develop an accurate analytical model to calculate the attenuation of an UWB signal as it propagates through the human body where the human body is modeled as a layered structure in which each layer is characterized by its complex dielectric properties with specific transmission and reflection coefficients.
4) To carry out FDTD simulation of the proposed human thorax model, to study the time behavior of the pulse propagated through the tissues and to

determine the propagation time and estimated echo time.

5) To study the operation of the Pixel circuit, which comprises of a loop inductor connected in parallel to a MEMS vibrating diaphragm variable capacitor, to obtain a flat frequency response over a 2 GHz bandwidth and to carry out the lumped element circuit model simulation of the Pixel circuit using OrCAD® PSpice® to determine the design parameters of the Pixel loop inductor.
6) To carry out finite element modeling of Pixel capacitor to optimize the device geometry while achieving the desired sensitivity and frequency independent operation.
7) To develop a fabrication process to fabricate the proposed microwave Pixel.

1.2 Background

1.2.1. Existing technologies

A brief review of existing technologies and technology trends is required to clearly understand the necessity of a new transformative drive in diagnostic data acquisition technologies. The basic principle of bio-medical diagnostic imaging system is to expose the target biological tissue with a permissible amount of energy such as electromagnetic (EM), magnetic, ultrasound, nuclear, etc. and then collect the signal interaction response data of the tissue using appropriate sensors/transducers/detectors placed around/on/near the target. The collected data is processed using suitable algorithms to produce an image of the target organ/tissue. Present techniques for diagnostic imaging such as X-ray, ultrasound, Computed Tomography (CT), Positron Emission Tomography (PET), PET-CT,

Single Photon Emission CT (SPECT), radioactive isotopes, and Magnetic Resonance Imaging (MRI) produce a visual display or representation of anatomical and functional information of the organs inside the human body [4]. Figure 1.3 provides an illustration of typical medical diagnostic imaging techniques.

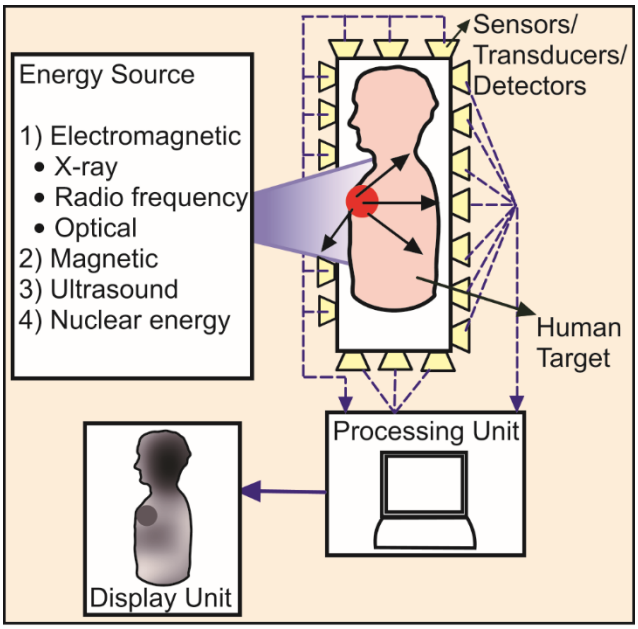

Figure 1.3. Basic Principle of medical diagnostic imaging.

Each of these techniques has its relative advantages and disadvantages. For example, ultrasound imaging is non-invasive and non-ionizing, but has difficulty in penetrating through the bones and the accuracy highly depends on the operator. Also, it has the risk of false positive results leading to unnecessary biopsies. On the other hand, X-ray provides higher resolution images but it exposes the body to harmful radiation. In terms of cost, MRI, PET, and SPECT are expensive. Although CT presents excellent spatial resolution, CT is less informative in soft-tissue functional imaging than PET [5]. However, PET cannot compete with CT in terms of spatial resolution. Commercial high speed 640 slice

CT scanners with an ability to capture a complete high-resolution image of the heart muscle in less than one-third of a second are available [6]. Available high-resolution CT scanners allow the clinicians to acquire and reconstruct images with 0.625 mm to 1.25 mm thin slices [7]. The new 11.75 T INUMAC MRI is able to image an area of about 0.1 mm, or 1000 neurons, and help us to see changes occurring as fast as one-tenth of a second [8]. This is far superior to the standard MRI resolution of 1 mm per second [8]. There are also some emerging high-resolution imaging techniques that work on the level of molecules and genes and can reveal pathological processes at work long before they become apparent on the larger scale such as information of tumors [9].

1.2.2. Need for new-transformative in medical imaging systems

Despite the stunning progress in diagnostic technologies in last two decades which resulted in significantly improved accuracies and image qualities, one thing that has not changed is patient experience, which has never been friendly. Invasiveness, risk of infection, risk of ionizing radiation exposure, lengthy procedure, long waiting time, lengthy waits for the result (except in the case of ultrasound), uncomfortable, embarrassing, etc. are few common complaints from the patients about their experiences. A review of the existing medical diagnostics systems concludes that, “There is, at present, no technique for the imaging of internal structures of the human body which is universally applicable to all tissues, has high-resolution, is inexpensive, uses non-ionizing radiation, creates images in real-time, and can be carried out in the office of a physician or dentist” [2]. Consequently, it is of paramount importance to develop low cost portable high-

resolution, real-time, non-invasive, non-ionizing, and non-contact diagnostic imaging solutions to facilitate their use in primary care offices for faster diagnosis and treatment. Though the digital technology enables the processing of the diagnostic data using advanced image processing algorithms to obtain sharper high contrast images, the outcome or the efficiency of the entire imaging system in fact is limited by the capabilities of the transducer (imaging) hardware.

In this context, this thesis presents the design of a MEMS microwave Pixel that can be used in an ultra-wideband (UWB) radar to enable 3-D high-resolution biomedical diagnostic imaging at a lower cost. The scientific basis behind the proposed approach is to exploit the interaction and backscattering properties of microwave energies with biological tissues using emerging MEMS based devices to generate superior performance high-resolution 3-D diagnostic images. Due to miniature size and batch fabrication capability of the MEMS technology, the proposed technique has a high potential to develop a hand-held imaging system in near future. Having a non-radiation imaging alternative is particularly attractive in children and pregnant women.

1.3. Principal Results

The principal results of this research work are summarized as follows:

1) A MEMS based microwave Pixel of footprint size 595 µm × 595 µm, operating in the UWB frequency range of 3.1 GHz - 5.1 GHz is designed for use in an UWB radar to image a human thorax deep upto to 4.2 cm, from a standoff distance of 4.8 cm from the human target. The designed Pixel is

capable enough to detect the magnetic component of the tissue reflected electromagnetic signal with a strength as low as 0.8 μAm^{-1} to affect a Pixel capacitance change of 4.5 aF.

2) The proposed radar system transmits a 400 ps gaussian pulse having a pulse repetition period (PRP) of 1.8 ns and a spectral distribution of 3.1 - 5.1 GHz, onto the human thorax. The field of view (FOV) is the section of the human thorax that is necessary to be imaged. FOV of the present application is 32.8 cm × 32.8 cm as shown in Figure 1.4. A matrix array of approximately 360000 Pixel elements would be required to provide a sufficient cross-sectional view of human thorax, with each Pixel size of 595 µm and a Pixel array of size 14 inch × 14 inch and a theoretical lateral resolution of 0.59 mm.

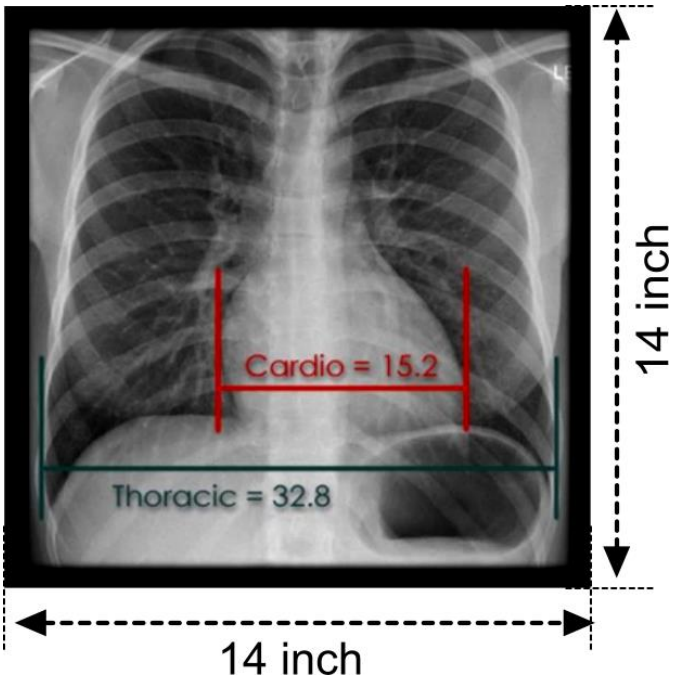

Figure 1.4. Estimated Pixel array size of 14 × 14 inch to image FOV of 32.8 × 32.8 cm.

3) A study on frequency dispersion of human tissues, using the models developed in [24], [25], [26], showed the contrast between the successive tissues of the human thorax as in Table 1.1. This contrast supports the idea of UWB radar based human thorax tomographic imaging.

TABLE 1.1 ELECTRICAL PROPERTY CONTRAST FOR SUCCESSIVE TISSUES IN HUMAN THORAX MODEL AT 4.1 GHz.

Successive tissues	Relative dielectric contrast	Conductivity contrast
Skin, Fat	7.1:1	13.4:1
Fat, Muscle	1:10	1:17.2
Muscle, Cartilage	1.4:1	0.97:1
Cartilage, Lung	1.8:1	2.4:1
Lung, heart	1:2.7	1:2.8

4) An analytical model proposed in [34] for biomedical implant has been implemented in this work using MATLAB® and the one-way attenuation of the UWB signal to go 4.2 cm deep into the human thorax is calculated to be 33.46 dB and it shows an excellent agreement with the FDTD model of the thorax presented in [35].
5) The circuit level simulation of the Pixel inductor circuit has been done using OrCAD® PSpice®, and the Pixel capacitor is simulated using Finite element method (FEM) using IntelliSuite®. The optimized Pixel design for human thorax application is comprised of 595 µm × 595 µm inductance area and 150 µm × 150 µm variable capacitance area with the total inductance of

86.382 pH and tuning capacitance range of 1.68:1. The inductance area is composed of cross-parallel connected 12×12 array of square geometry sub-Pixel inductors with side length of 45 μm and 12.439 nH inductance.

6) The fabrication steps of the proposed microwave Pixel are developed.

1.4. Organization of Thesis

The thesis is organized as follows. Chapter 2 concisely summarizes the available literature of UWB radar for medical applications. The safety concern of microwave imaging is discussed and the effect of microwave radiation on various human tissues and their frequency dependent electrical properties like complex permittivity and conductivity are explained in detail. Lastly, the operation of an UWB radar system with the proposed microwave Pixel has been illustrated.

Chapter 3 presents the detailed operation of the proposed microwave Pixel. The theoretical background of loop inductor and its equivalent circuit has been presented. Following that, the design of the Pixel capacitor and its mathematical formulation are presented in detail.

Chapter 4 starts with a description of the human thorax anatomy and introduces the target application of this thesis, i.e., a coronal scanning of the human thorax to detect chest wall abnormalities and Pneumothorax condition. An analytical model implemented in MATLAB®, to determine the attenuation of UWB signal through human multilayered thorax model has been described. In the following section, an FDTD simulation of the planar thorax model using Remcom® XFdtd® software is discussed. Lastly, the analytical model results have been

compared with the FDTD simulation results to validate the design.

Chapter 5 presents the feasibility analysis of the proposed microwave Pixel for human thorax imaging application. A mathematical model to determine the power level of the reflected signals from each tissue interface is presented. The circuit level simulation of Pixel inductor in OrCAD® PSpice® and the Finite Element Method (FEM) simulation of Pixel capacitor are presented. Lastly, the performance specifications of the proposed Pixel are presented.

Chapter 6 presents a tentative fabrication process to fabricate the proposed microwave Pixel. A step by step description of the major process steps are presented with cross-sectional views.

Chapter 7 presents the concluding remarks and suggests some future directions.

CHAPTER 2

UWB RADAR FOR MICROWAVE IMAGING

This chapter covers a review of the existing literature on UWB radar for medical applications. The safety concern of using microwaves for human tissue imaging and the frequency dependency of tissue electrical properties are discussed in detail. The rest of the chapter presents the operating principle of the proposed microwave Pixel array based UWB radar for medical diagnostic imaging.

2.1. UWB Radar for Medical Application

An UWB device is defined as any device where the fractional bandwidth is greater than 20% [10] or has a UWB bandwidth equal to or greater than 500 MHz, regardless of the fractional bandwidth. The fractional bandwidth is defined as $2(f_H - f_L)/(f_H + f_L)$, where f_H is the upper frequency of the -10 dB emission point and f_L is the lower frequency of the -10 dB emission point. [10]

An UWB radar transmits a sequence of impulse-like signals over a large bandwidth that satisfies the UWB criteria. The typical pulsewidth is in the range of 100s of picoseconds to several nanoseconds and the rise time is as fast as 50 picoseconds [11]. Extremely short duration pulse generates a very wide bandwidth. Since the energy of the pulse is distributed across many frequencies, the power spectral density is much lower in magnitude than a narrowband system. Since, the pulse length of UWB signal is comparable to the target size, the reflected pulses changes with the structural and electrical nature of the target. These

changes in the pulse shape give useful information about the shape and material properties of the target. The Federal Communications Commission (FCC) frequency band assigned to UWB medical systems extends from 3.1 GHz to 10.6 GHz, i.e. a bandwidth of 7.5 GHz centered at 6.85 GHz [10].

As the generated series of short duration UWB microwave pulses propagate through a human body, in addition to suffering from propagation losses due to wave attenuation, absorption, and scattering, they also interact with the biological tissue molecules [12]. The frequency dependent dispersive characteristics of the biological tissues alter the bulk dielectric properties of the tissues [12] and in turn, change the reflection coefficient. Hence, unlike the narrowband signals, the different frequency components of the UWB signal undergo a different level of attenuation and dispersion within the tissue medium. Consequently, this alters the waveform and power spectral density of the transmitted pulse as it gets reflected from a tissue boundary, such as fat, muscle, blood, cartilage, bone, etc. Thus, the received signal inherits a unique signature of the interacting tissue. Deciphering this information using appropriate signal processing provides the exact characteristics of the tissues. A range gate can be used to sample received signals at specific time intervals [13]. The receiver window size corresponds to the time window for sampling. Choosing a small window allows greater axial resolution; however, faster sampling circuits are necessary. Such two-dimensional images can be cascaded to form a 3-D radar based high-resolution images similar to computed tomography.

UWB impulse can pass through biological materials including skin, muscle,

fat, bone, and clothes. This enables non-contact and non-invasive penetration of UWB signals to image deep internal body organs without any ionizing radiation or contrast agent. UWB radar techniques can be used to detect and identify small, low contrast objects from their shape, composition and return spectrum characteristics [13]. The UWB can operate in radar mode, in tomography mode, or a novel unique combination of both to generate dynamic very high-resolution 3D functional images [14]. Remote sensing of the body and inner organ motion by UWB radar is a promising alternative to electrocardiogram (ECG) based gating of several diagnostic imaging and image guided therapy modalities, e.g. cardiac MRI and high energy particle therapy [14]. In [14] it has been mentioned that “By monitoring the cardiac mechanics rather than the electric functionality, the UWB method is more favorable to prevent distortions in high-resolution medical imaging by motion artifacts”. Another advantage in using UWB technology is that the UWB transceiver is simple and occupies a very small chip area as it does not require complicated frequency recovery system as in the narrow bandwidth transceiver [15]. In [16], it has been mentioned that microwave tomography (MWT) might present a safe, portable, and cost-effective supplement to current imaging modalities for acute and chronic assessment of cerebral vascular diseases including stroke that can be made widely available at the “bedside” in the emergency department or to the first response paramedic services. In [17] it has been mentioned that UWB radars and ultrasound are in fact very similar and many of the signal processing techniques used in ultrasonic systems can be applied to UWB systems. In [13], it has been mentioned that UWB radar based scanners

could provide small medical clinics with imaging and diagnostic capabilities currently available in hospitals.

Despite being an emerging technology, some UWB radar based health systems are already developed by few research institutes. A handheld UWB sensor has demonstrated the feasibility of detecting the presence of traumatic internal injuries including intracranial hematoma and pneumothorax [13]. Experimental evidence presented in [2] shows that microwave returns from within several superimposed yet distinct layers of different dielectric materials when transformed to the time domain indicate the exact depth at which the layer changes and propagation characteristics distinct to each layer traversed. The significance of this experiment is that it proves the basic theory of radar tomography that it is possible to record different densities or dielectrics, of materials at predetermined depths of study. As a result, one can ‘see into’ the depths of the stacked materials and the information can be displayed in a graphical format. It has also been demonstrated that as tissue malignancies, blood supply, hypoxia, acute ischemia, and chronic infarction change tissue dielectric properties, microwave imaging offers the potential for the diagnosis of functional and pathological tissue conditions, including perfusion and perfusion-related injuries [16]. In [18] the authors used a signal processing technique to extract the ECG signal from the blood pressure data. As an UWB radar is able to detect the blood pressure in a non-contact mode with a very high accuracy [19], a suitable signal processing technique can be developed to extract the ECG signal from a non-contact blood pressure measurement using the UWB radar and display it on a monitor.

In [20], some experimental results were published from a few Russia and Taiwan based hospitals using UWB systems. The experimental data shows that a 5.75-7.35 GHz UWB radar with a transmit pulse power of 9 mW and pulse repetition frequency of 2 MHz was able to detect the thorax movement of as minimum as 100 micrometers from a distance of 0.6-3.5m. The authors in [20] studied several hundred-comparative radar and ECG measurements of HR (heart rate) and VHR (variable heart rate) to find out that the average deviation of the radar data from ECG data was only 1.52% while the averaged correlation coefficient was 0.915.

The author in [2] suggested using a matrix filter to realize a 2D energy map of the returned radar signal. He estimated that a resolution of 0.25 mm can be achieved and a cross-sectional area of 15 cm x 15 cm was needed for visualization of the heart in function. For the matrix filter to map the backscattered energy, he proposed to use narrow tubes of microwave absorbing materials in a fashion similar to a modulated scatter method as was used in [21]. In [13], a bed panel UWB radar from Sensiotec has been reported for measuring heart and respiration rates. The bed panel UWB radar has a 4 GHz center frequency with a ~2 ns pulse length and ~50 nanowatts radiated power. Another device from Sensiotec called Pneumoscan™ uses UWB radar to detect bleeding within the chest cavity [13].

2.2 Microwave Imaging for Human Tissues

2.2.1. Safety concern

The present research is focused on the microwave frequencies of the electromagnetic(EM) spectrum. The heating effect due to Propagation of

microwave frequencies through human tissues is determined by their electrochemical behavior of the cells, its cellular structure and on inter-cellular fluid [12]. At lower frequencies, the cell membrane exhibits capacitance and a potential difference across it, so the current flow around the cell but at high frequencies, current may penetrate the cell [12]. So, application of electric field to the tissue causes a displacement of charge, which leads to relaxation phenomenon and results in the heat generation. More importantly these kinematics gives rise to the frequency dependence of its bulk dielectric properties. The main dosimetry quantity used to measure the level of interaction with the tissue is Specific Absorption Rate (SAR). SAR can be defined as the rate of absorbed non-ionizing radiation per unit mass of the tissue. Based on different studies, International Commission on Non-Ionizing Radiation Protection (ICNIRP) established exposure limits of time-varying electric, magnetic and EM fields to protect from adverse health effects [22] as shown in Table 1.

According to [23], the other effects of EM radiation on any material it is exposed to is ionization and molecule cracking but this occurs at several KV/mm, which is far away from the limiting levels of microwave imaging. The next effect on human tissues due to EM radiation is photon energy. But this energy is harmful only at high frequencies, this can be proved by a simple calculation. Considering the particle nature of EM wave, the energy of the photon (*E*) can be calculated as,

$$E = h\nu \tag{2.1}$$

where h is Planck constant which is equal to $4.13 \times 10^{-15}\, eV\, s$ and f is the

frequency of the EM field. Thus, the photon energy of harmless, human eye sensitive visible light of 500 THz frequency is nearly about 2.065 eV While, the photon energy of 4 GHz microwave frequency is about 16.52 μeV which is 10^6 orders less.

TABLE 2.1 GENERAL PUBLIC EXPOSURE LEVEL TO EM FIELDS.

Frequency range	E-field strength	H-field strength	B-field strength	Equivalent plane wave Power density, S_{eq} ($W.m^{-2}$)	Whole-body average SAR ($W.\ Kg^{-1}$)
10-400 MHz	28	0.073	0.092	2	0.08
400-2000 MHz	$1.375\ f^{1/2}$	$0.0037\ f^{1/2}$	$0.0046\ f^{1/2}$	f/200	0.08
2 – 300 GHz	61	0.16	0.20	10	0.08

This shows that microwave medical imaging is absolutely safe and the intuition of general public to use microwave frequencies for medical imaging as a health hazard can be ruled out, as long as ICNIRP exposure limits are followed [22].

2.2.2. Tissue properties

Human tissues are classified as soft tissues and hard tissues based on their molecular composition. Soft tissues are made of high water content and traces of inorganic material whereas hard tissues contain less water content and high inorganic content. Depending on the amount of the fluid content in the tissue, the frequency behavior of the tissue varies. Using UWB signal has an advantage of getting enough information to distinguish different tissues, because some tissues may have same characteristics at certain frequencies, but operating in the wide

range of frequency makes it more distinguishable. The knowledge of the dielectric properties of various biological tissues at microwave frequencies is of much significance in deriving useful information in this kind of imaging. From the knowledge of dielectric constant, tissue properties can be characterized in the microwave frequency range. As it is known, the dielectric constant is the parameter which characterizes the ability of the tissue to store electrical charges compared to free space, and the conductivity is a measure of the ability to transport charges with the field. These two parameters solely characterize the electrical characteristics of the matter.

Hence the motivation for using microwaves to image a human biological body is the fact that microwave signals are sensitive to the dielectric changes in their propagation channel. The human body is made of inhomogeneous lossy dielectric layers and can be modeled as a multilayered dielectric structure, each layer is associated with its own dielectric property electrical conductivity and mass density as a function of frequency. From [24] Gabriel et al. experimentally measured the electrical properties of different human tissues over a wide frequency range. The parameterization developed by them are used in this thesis, to estimate the dielectric properties of the tissues over the desired UWB range.

According to Debye's equation and four Cole-Cole models [25] [26], the complex permittivity of a tissue ε_{r_i} at different frequencies is calculated following (2.2) as,

$$\varepsilon_{r_i}(\omega) = \varepsilon_{\infty} + \sum_{m=1}^{4} \frac{\Delta\varepsilon_m}{1+(j\omega.\tau_m)^{(1-\alpha_m)}} + \frac{\sigma_{\text{static}}}{j\omega.\varepsilon_0} \quad (2.2)$$

where, ε_{∞} is the complex permittivity in the terahertz frequency range, α_m is the distribution parameter, σ_{static} is the static ionic conductivity, τ is the relaxation time and $\Delta\varepsilon_m$ is the magnitude of dispersion. The permittivity and conductivity curves of 22 different human tissues are shown in Figures 2.1(a-d) and 2.2(a-d) for UWB frequency range of 3.1 GHz to 10.6 GHz. For a better understanding of the significance of these curves, the tissues are grouped and shown in four different Figures based on their position in the body.

The first group consists of few tissues of a human digestive system like liver, gallbladder, stomach, spleen, small intestine, and colon. Their permittivity and conductivity curves are shown in Figure 2.1a and 2.2b. It is observed that the relative permittivity of the tissues is decreasing with increase in frequency while, the conductivity is increasing with frequency. At high frequencies, distinguishing the colon and small intestine seems difficult as their permittivity is approaching very close to each other. Relative permittivity mapping at lower frequency and conductivity mapping at higher frequency seems to be beneficial.

The second group consists of few tissues of human brain like grey matter, white matter, cerebellum, dura, and nerve. Their permittivity and conductivity curves are shown in Figure 2.1c and 2.1d. The permittivity of these tissues can be well differentiated. The conductivity of grey matter and cerebellum are very close around 5 - 7 GHz frequency band but can be distinguished at other frequencies.

This shows the importance of UWB range of operation, for medical diagnostic imaging.

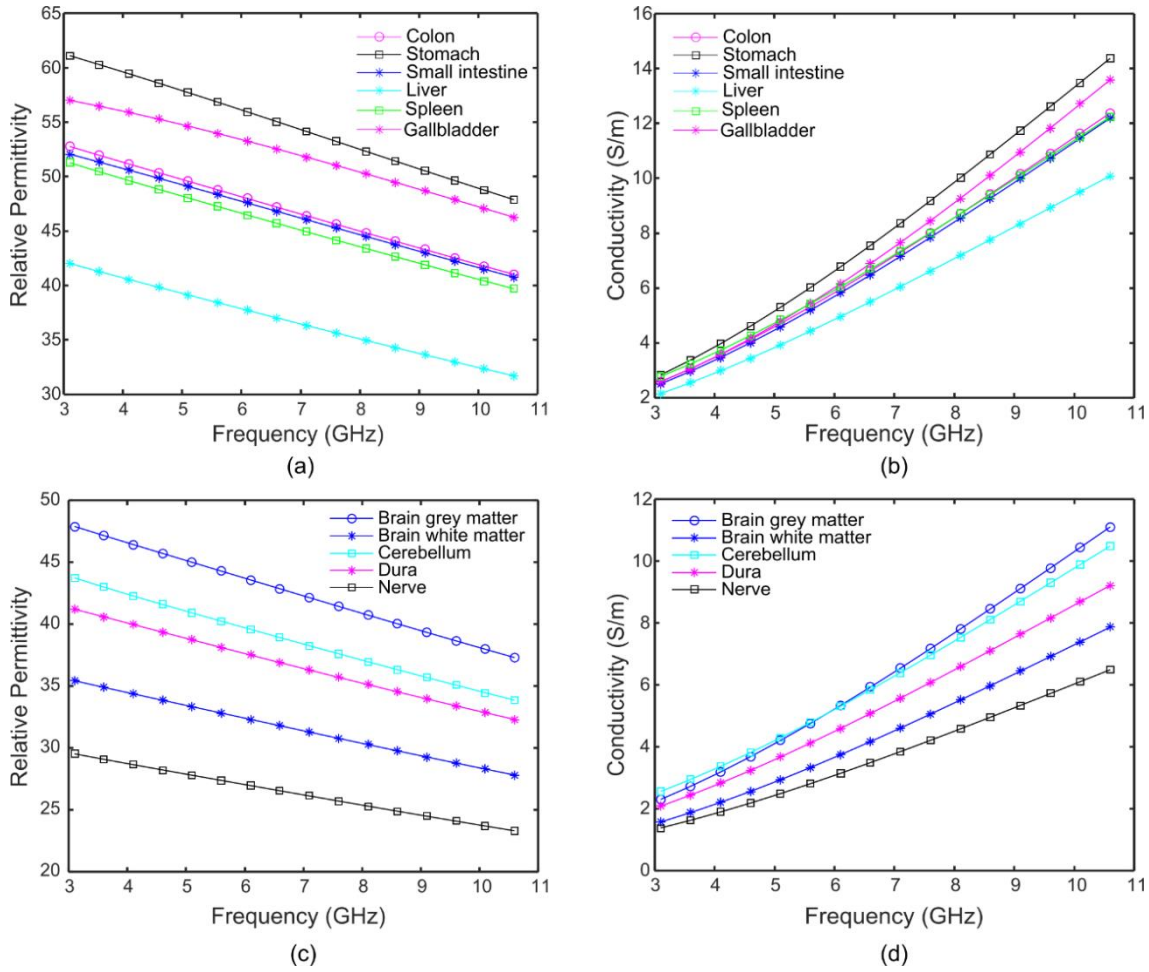

Figure 2.1. a) & b) Permittivity vs Frequency and Conductivity vs Frequency curves for few tissues of human digestive system, c) & d) Permittivity vs Frequency and Conductivity vs Frequency curves for few tissues of human brain.

Figure 2.2a and 2.2b includes the permittivity and conductivity of third group consists of bladder, cervix, uterus, and ovaries that involve in diagnosing cervical cancer in women. it is shown that all the permittivities are well differentiated when compared to the conductivity curves. It is observed that around 9 GHz the conductivities of ovary and cervix are almost same and cannot be distinguished.

The fourth group consists of few tissues of human thorax like heart, aorta, Lungs both inhaled and exhaled, muscle, cartilage, blood, fat etc. Their permittivity and conductivity curves are shown in Figures 2.2c and 2.2d. From Figure 2.2c it is observed that all the permittivities of muscle, fat and inflated lungs are decreasing less fast with frequency when compared to other tissues. With the increase in frequency, the permittivity curves of heart and muscle are approaching close to each other making them indistinguishable. But inferring to Figure 2.2d the

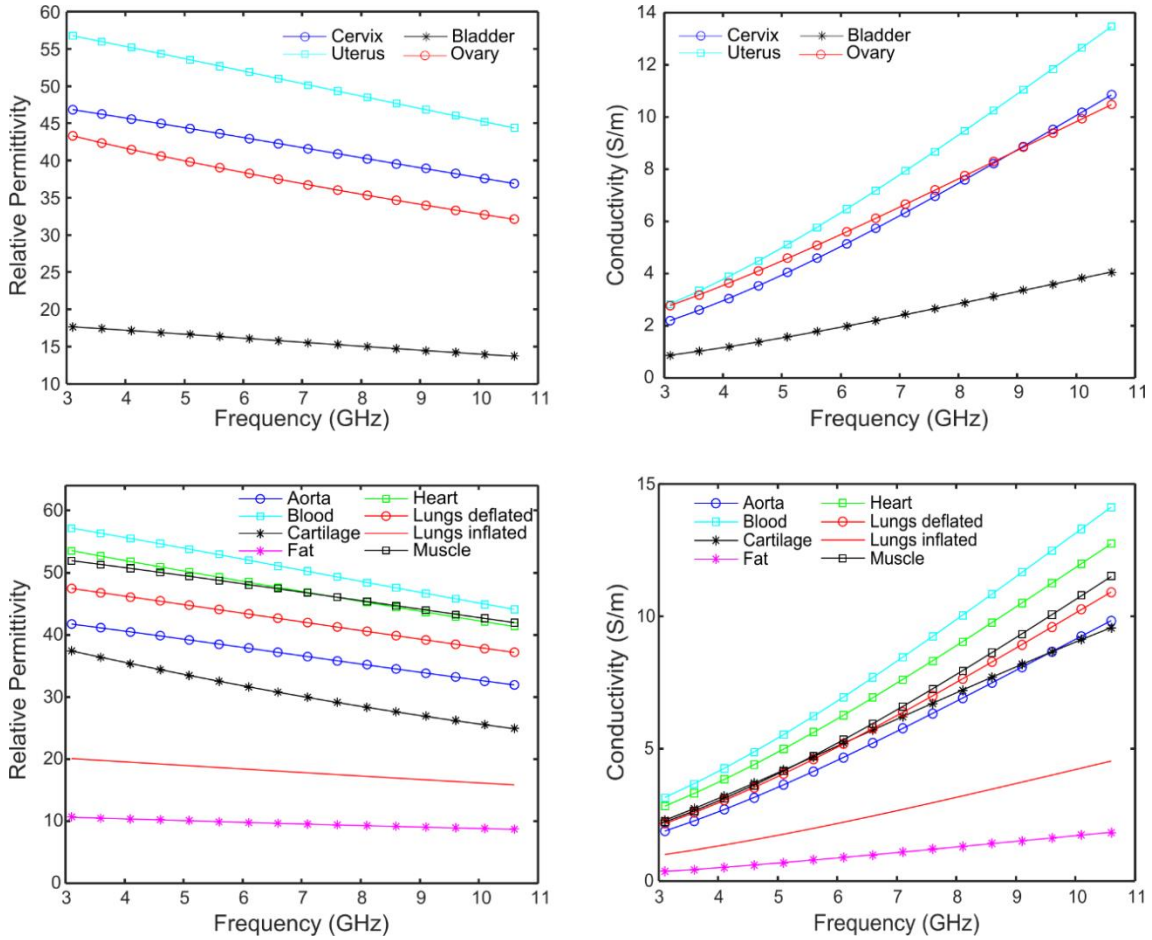

Figure 2.2. a) & b) Permittivity vs Frequency and Conductivity vs Frequency curves for few tissues around cervix in women reproductive system, c) & d) Permittivity vs Frequency and Conductivity vs Frequency curves for few tissues of human thorax.

conductivity map of heart and muscle should have a considerable difference. So, the best way to image the human thorax using UWB microwaves is by extracting information both from conductivity and permittivity maps of the tissues (in simple complex permittivity map) for accurately distinguishing them.

From Figures 2.1 and 2.2, hard tissues such as bone, fat, lung(deflated) have lower permittivity values due to their low water content when compared to soft tissues such as muscle, blood, brain, and other internal organs. By comparing the generated maps with these curves, the tissue can be identified and also the diseased tissue can be differentiated from the healthy tissue. Though a lot of research needs to be done, to study the usefulness of these maps generated for detecting any malignancy or deficiency, this mode of imaging sounds beneficial both conceptually and technically.

2.2.3. Contrast between healthy tissues and cancerous tumors

The main motivation of using UWB microwave imaging for cancer detection is the high contrast in the complex permittivity and conductivity of malignant tumor

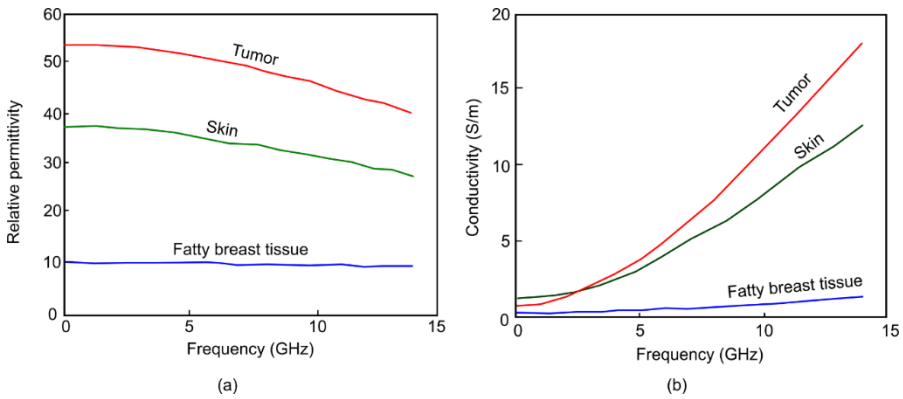

Figure 2.3. Frequency dependence of relative permittivity and conductivity for skin, tumor and healthy breast tissue [27].

and healthy tissue. For the case of breast cancer, according to [27] the dielectric contrast is about 5:1 and conductivity contrast is 10:1 for malignant and normal breast tissue as shown in Figure 2.3. According to [28], UWB imaging for breast cancer detection has the advantage of differentiating malignant tissue and benign tissue. This is because, the contrast between the benign and normal breast tissue is not same as the contrast between the malignant and normal breast tissue.

2.3. UWB Radar system with Proposed Microwave Pixel Array

A conceptual block diagram of the proposed MEMS microwave Pixel based UWB radar is shown in Figure 2.4. The radar operates in the frequency range of 3.1 GHz to 5.1 GHz. The operation of transmit module of UWB radar system starts with a trigger signal generated by timing and control unit to initiate the first pulse from a pulse generator. This instantaneously enables a delay generator that commences waiting for a certain time until a second trigger is activated [29]. Concurrently, the sensor electronics are activated to collect and then store the Pixel array processed output for the further stage of processing before the generation of the second pulse.

The receiving section of the radar system comprises an optional microwave focussing lens to converge the received signal energy on to the proposed MEMS based microwave Pixel array. Each Pixel in the array is illuminated by a section of the received signal wavefront and generates a corresponding voltage. Sensor electronics involves the readout circuitry which sequentially fed the voltage across the individual Pixels generated at different frames to the Analog to digital converter

(ADC). The sampled output from ADC is processed by suitable algorithms in a digital signal processor to generate a voltage map corresponding to the dielectric properties of the respective tissue layer.

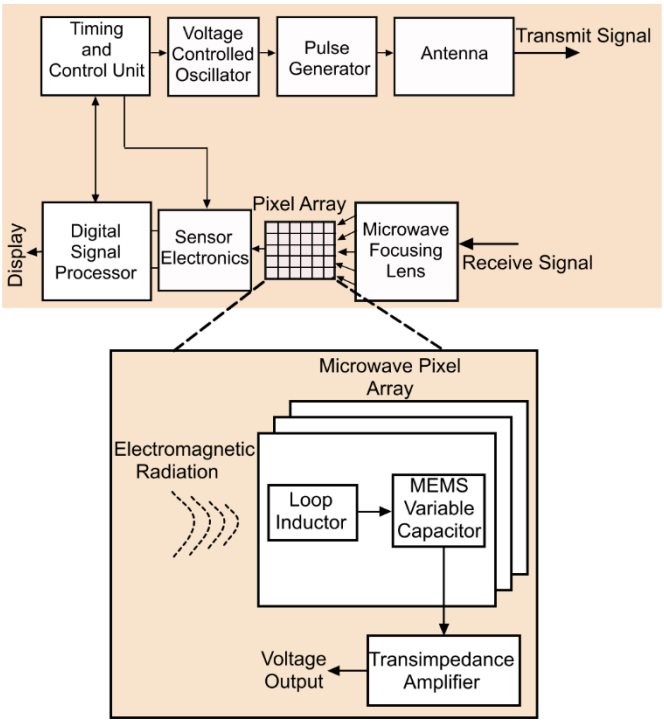

Figure 2.4. Block diagram of UWB radar system.

The resolution of the conventional imaging system is dependent on the signal's wavelength. To overcome the limitation of the wavelength on Pixel size, the proposed Pixel array is designed to operate at subwavelength. An optional microwave focusing lens can also be used to illuminate a smaller geometry Pixel to increase the resolution further. The concept is illustrated in Figure 2.5.

As an UWB signal changes its shape unlike narrowband sinusoidal signals during its propagation through the human tissues, this way of capturing is more suitable as the radiation at different time intervals are captured continuously to scan the specific area of the target at specific depth. This enables the generation

of voltage map at each time interval ($t_1, t_2, t_3, \ldots t_7$) as shown conceptually in Figure 2.5. A 3D voltage map of the whole target thus can be obtained by cascading the 2D maps generated at different time intervals as shown in Figure 2.6.

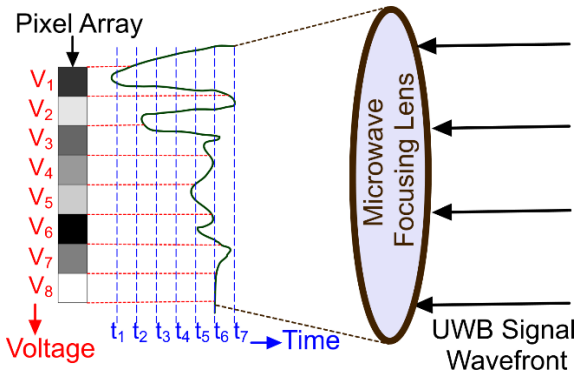

Figure 2.5. Sub-wavelength capturing of incident signal at different time intervals.

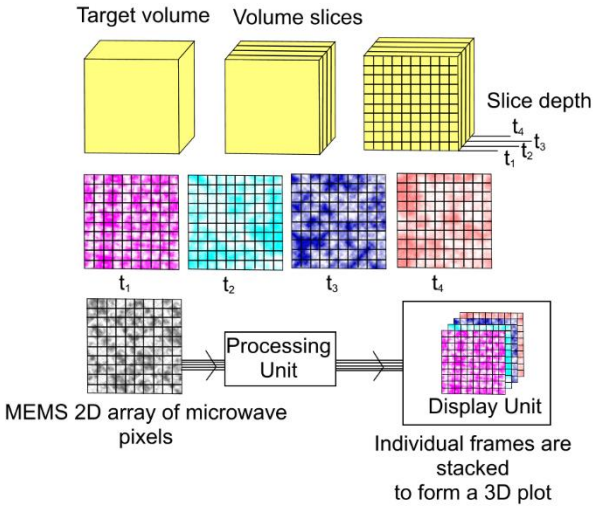

Figure 2.6. Conceptual 3D tomographic image generation using the MEMS based Pixel array.

CHAPTER 3

MEMS MICROWAVE PIXEL DESIGN

This chapter focuses on the basic operating principle of the proposed novel microwave Pixel. A theoretical analysis of the loop inductor/loop antenna, its equivalent circuit and design parameters are discussed in detailed. And then the discussion extends to the design of the MEMS vibrating diaphragm variable capacitor and its mathematical formulation.

3.1. Microwave Pixel Operation

A conceptual geometry of the developed MEMS microwave imaging Pixel is shown in Figure 3.1. The front end of the designed Pixel is a microfabricated spiral inductor (acting as a small loop antenna) which is connected across a microfabricated vibrating diaphragm variable capacitor. When the Pixel is placed in a radiation field in which it is designed to operate, the inductor acts as a loop antenna to generate a voltage following Faraday's law of electromagnetic induction. This voltage appears across the electrodes of the microfabricated vibrating diaphragm capacitor to generate an electrostatic attraction force between the capacitor electrodes. This deforms the diaphragm further from its initial offset deformation due to a DC bias to affect a change in capacitance between the capacitor electrode. The higher the magnetic field linkage with the Pixel inductor, the higher the capacitance change in the variable Pixel capacitor. This capacitance change is converted to a voltage signal using an appropriate transimpedance amplifier.

The combination of the Pixel inductor (loop antenna) and the Pixel capacitor basically is an LC parallel circuit resonating at a desired frequency. Following [30], it is possible to design a wideband loop antenna operating in the UWB frequency range corresponding to the target diagnostic imaging application. A combination of such a wideband loop antenna and the variable capacitor thus would be able to generate a frequency independent voltage signal over the desired UWB frequency range. The Pixel capacitor is not limited to be one, it can be replaced by an array of capacitors connected in parallel/series, similarly, the loop inductor can be a single loop inductor or group of loop inductors connected in series/parallel based on the application. Thus, it is possible to design a wideband Pixel operating at UWB frequency range to generate a desired voltage output.

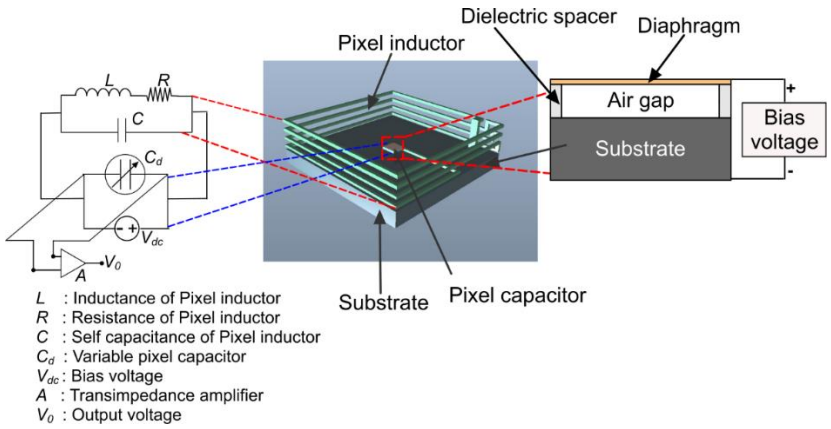

Figure 3.1. MEMS Microwave Pixel.

3.2 Pixel Inductor /Antenna Design

The main goal of microwave imaging Pixel inductor/antenna is to convert EM radiation into a voltage. In this proposed work, a small magnetic square loop inductor is used due to its smaller size of about less than one tenth of the

wavelength of operation. A loop inductor is sensitive to the magnetic component of the electromagnetic radiation. According to Faraday's law of electromagnetic induction, the open circuit voltage induced across the loop which is placed in the magnetic field is equal to the time rate of change of magnetic flux through it.

$$V_{oc}(t) = -\frac{d\phi(t)}{dt} \tag{3.1}$$

where V_{oc} is the induced open circuit voltage of the loop inductor in Volts and ϕ is the magnetic flux linking with the loop in Weber. As the Pixel is exposed to the microwave radiation reflected from a tissue layer at a certain depth inside the human body, following equation 3.1, a voltage is generated across the inductor in response to the varying magnetic component of the incident electromagnetic field. The induced RMS voltage as a function of the magnetic field can be expressed as [30]:

$$V_{oc\text{-}rms} = 2\pi\mu_0\mu_r NAfH_{rms}\cos\theta \tag{3.2}$$

where H_{rms} is the RMS value of the magnetic field intensity (Am^{-1}), μ_0 is the vacuum permeability (Hm^{-1}), μ_r is the relative permeability of the medium, N is the number of coil turns, A is the area of each turn (m^2), f is the frequency of the magnetic field (Hz), and θ is the angle between the magnetic flux lines and the plane normal to the loop surface.

3.2.1. Equivalent circuit parameters of the loop inductor

To determine the actual voltage generated across the inductor V_{AC} (i.e., the

voltage applied between the capacitor electrodes) the inherent resistive, inductive and capacitive elements of the antenna are to be considered. The equivalent circuit of the antenna including those inherent parameters can be modeled as shown in Figure 3.2a. where R_{AC} represents AC resistance in the circuit, R_{Rad} is the radiation resistance corresponding to the losses in the antenna during the

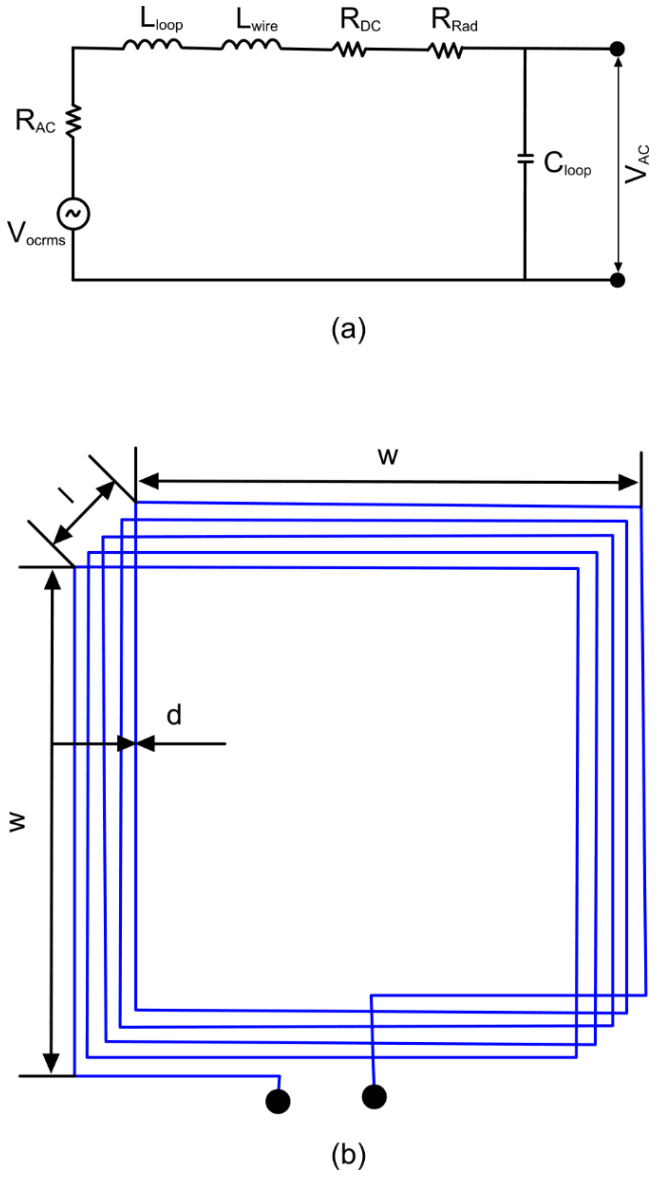

Figure 3.2. a) Equivalent circuit of loop inductor, b) Loop inductor with labeled physical parameters.

transformation of EM energy and R_{DC} represents the loss due to the resistance of the conductor. L_{loop} is the inductance of the square loop, L_{wire} is the inherent inductance of the conductor and C_{loop} is the parasitic capacitance of the square loop. These parameters are modeled using the following relations [30] in terms of inductor physical parameters shown in Figure 3.2b, where w is the length of the square loop, l is the length of the winding and d is the width of the conductor.

$$R_{Rad} = \frac{32\pi^4 10^{-7}}{3c^3}\left(N\mu_r A\right)^2 f^4 \tag{3.3}$$

$$R_{AC} = \left(\frac{4Nw}{\pi d}\right)\sqrt{\pi\mu_0 f \rho} \tag{3.4}$$

$$R_{DC} = \frac{(4Nw)\rho}{\pi d^2/4} \tag{3.5}$$

$$L_{loop} = \frac{N^2\mu_0\mu_r}{\pi}\left(\begin{array}{l} -2(w+l) + 2\sqrt{l^2+w^2} - \dfrac{l\ln\left(1+\sqrt{l^2+w^2}\right)}{w} \\ -\dfrac{w\log\left(w+\sqrt{l^2+w^2}\right)}{l} + l\log\left(\dfrac{4l}{d}\right) + w\log\left(\dfrac{4w}{d}\right) \end{array}\right) \tag{3.6}$$

$$L_{wire} \approx 2.10^{-7}(4Nw)\left(2.303\log\left(\frac{16Nw}{d}\right) - 0.75 + \left(\frac{d}{8Nw}\right)\right) \tag{3.7}$$

$$C_{loop} \approx 3.9685.10^{-13}\sqrt[3]{\frac{\left(\frac{400w}{\pi}\right)^4}{100l}} \tag{3.8}$$

where, ρ is the resistivity of the conductor and c is the velocity of EM wave in free space. The inherent inductance, capacitance and resistance of the loop inductor as a function of physical shape and size are shown in Figures 3.3, 3.4 and 3.5.

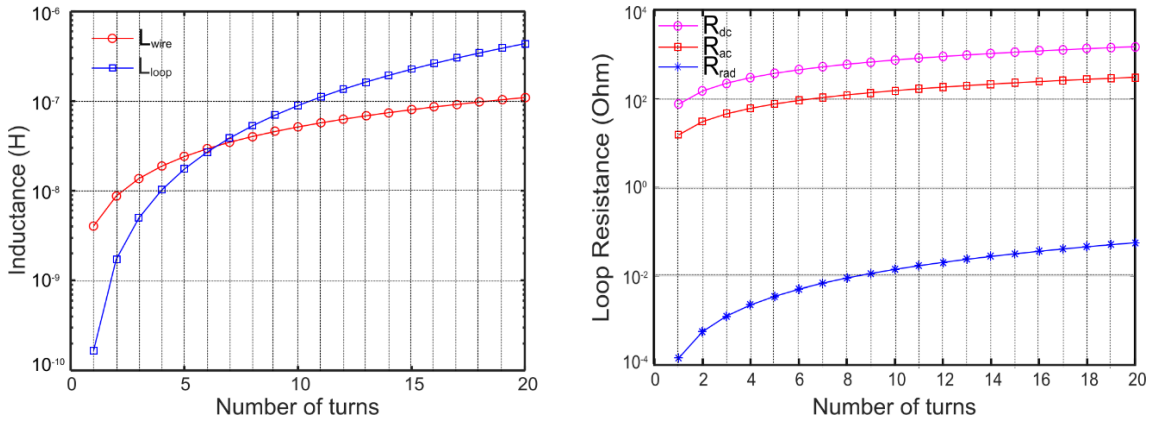

Figure 3.3. a) Equivalent inductance of the loop inductor as a function of number of turns, b) Equivalent resistance of the loop inductor as a function of number of turns.

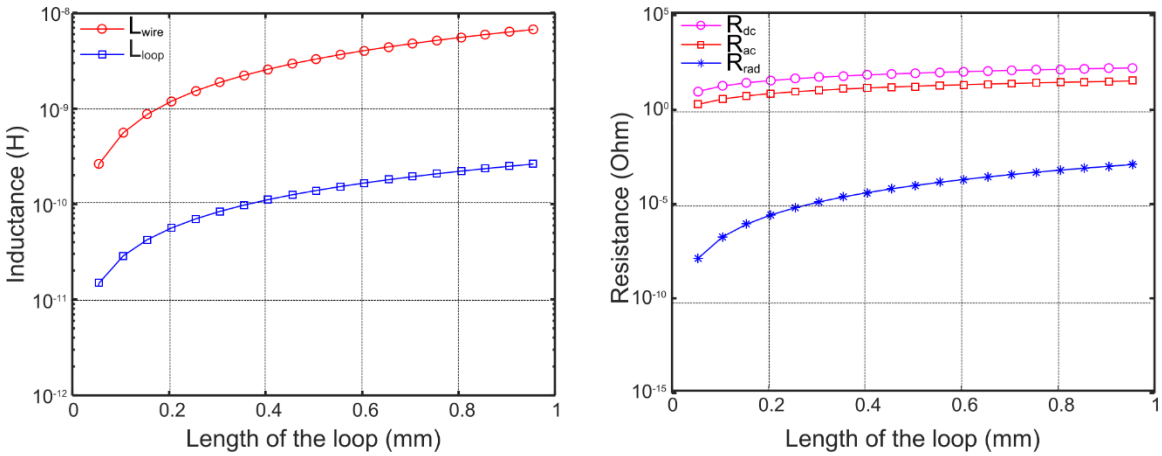

Figure 3.4. a) Equivalent inductance of the loop inductor as a function of loop length, b) Equivalent resistance of the loop inductor as a function of loop length.

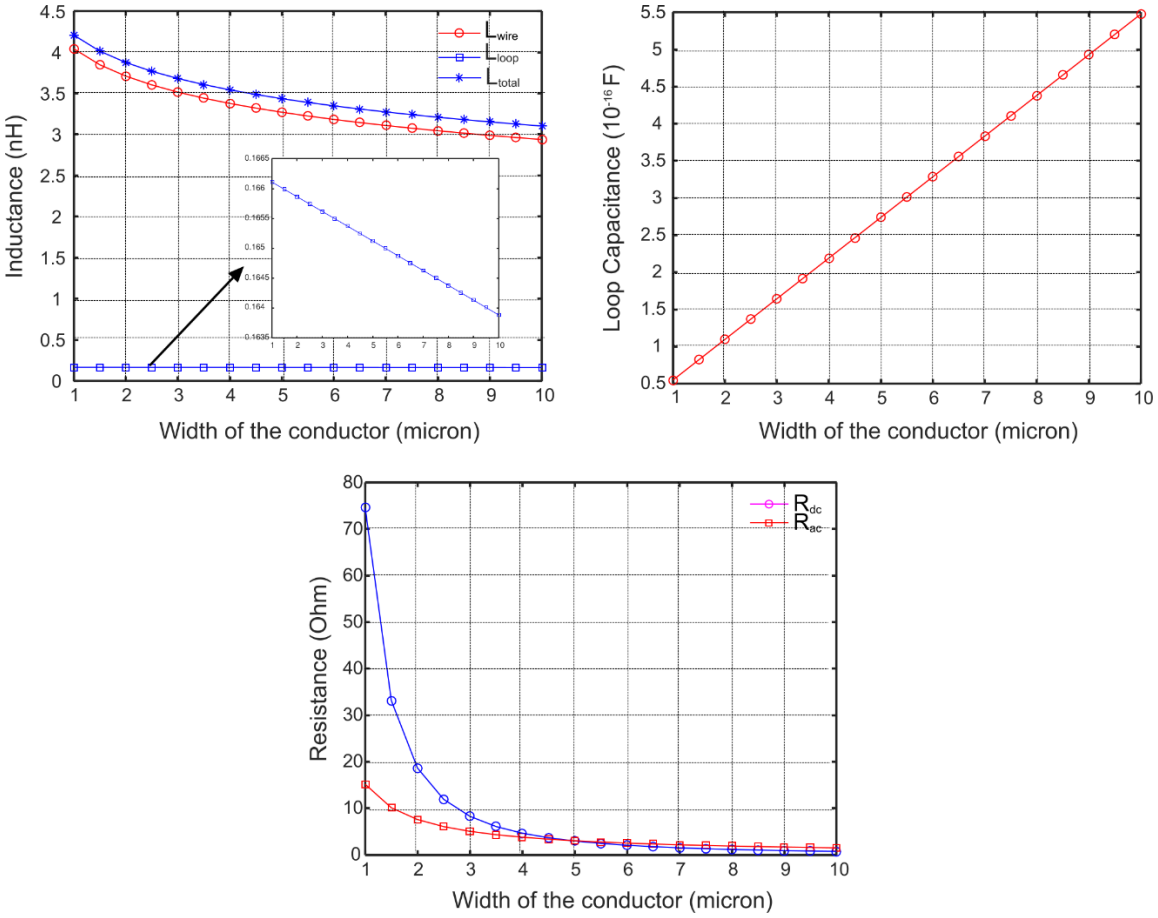

Figure 3.5. a) Equivalent inductance of the loop inductor as a function of conductor width, b) Equivalent capacitance of the loop inductor as a function of conductor width, c) Equivalent resistance of the loop inductor as a function of conductor width.

3.3. Pixel Capacitor Design

The proposed MEMS based Pixel capacitive sensor is realized using a thin square diaphragm which is separated by an air gap from a glass substrate patterned with a metal layer. This sensor operates as a parallel plate capacitor with one of the capacitor plates as a movable diaphragm making it a variable capacitor. The capacitance variation can be attained and controlled, by controlling a voltage across the plates or by controlling the charge on the capacitor plates. Thus, this

sensor measures the applied voltage/ or current by measuring the deflection of diaphragm using a capacitance readout device. The advantage of MEMS capacitors at microwave frequencies is the mechanical inertia of the structure preventing the modulation of the capacitance with the signal frequency [31].

To minimize the ohmic losses and parasitic capacitances, a thin layer of gold has been deposited and patterned on a glass substrate. Glass features excellent dielectric properties and low loss over the wide operating frequency range and temperature range. Also, glass substrates support micromachining of structures with well-defined features and it's low dielectric constant ease the fabrication of circuits at radio frequency (RF) and microwave frequencies [32]. Due to excellent electrical and mechanical properties of BCB, a low K polymer from Dow Chemical Company, has been selected as the dielectric layer on top of the gold layer (fixed electrode) to avoid a short circuit in the event of a pull-in [33]. BCB is also used as the dielectric spacer to define the membrane-electrode gap which can be realized by depositing a silicon dioxide as a sacrificial layer. A schematic of MEMS variable capacitor and its simplified equivalent circuit is as shown in Figure 3.6. The internal equivalent circuit of the Pixel capacitor is the combination of the variable capacitor C_{MEMS} between the movable diaphragm and the bottom electrode and the equivalent series resistance of the capacitive sensor R_{series} which includes the inherent resistance of the electrodes. To minimize R_{series}, gold has been selected as the diaphragm material.

Basically, the designed sensor is a voltage controlled electrostatic actuator.

Thus, to enhance the coupling between the weak AC input voltage variations induced by the loop inductor, and the mechanical movement of the diaphragm, the Pixel capacitor is charged with an offset DC bias voltage V_{DC} as shown in Figure 3.6c. The sensitivity S_c of the Pixel capacitive sensor can be defined as the ratio of the output capacitance change to the change in input voltage of the capacitor.

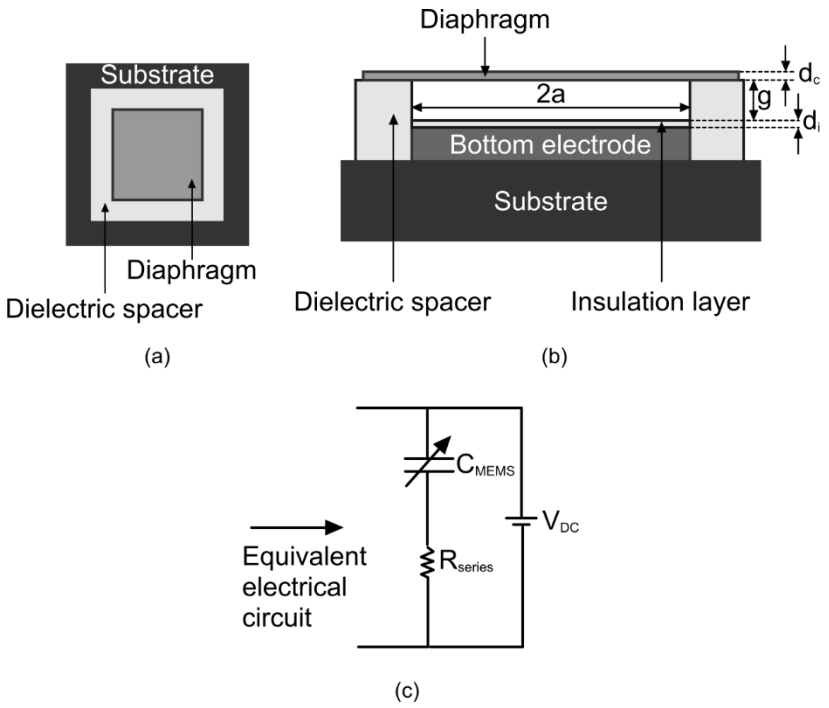

Figure 3.6. a) Top view of MEMS Pixel capacitor, b) Cross sectional view of the capacitor, c) Electrical equivalent circuit of the Pixel capacitor.

The design of the proposed Pixel capacitor should address two important goals. Firstly, to obtain adequate sensitivity to sense a very low voltage induced by the inductor and secondly, to obtain a flat and wide frequency response of the Pixel. These conditions are explained in detail in Chapter 5.

3.3.1. Mathematical formulation of the Pixel capacitor operation

The operation of this parallel plate actuator is based on the electrostatic attraction force between the bottom electrode and the suspended diaphragm. The capacitor is charged with a constant DC bias voltage, for better coupling between the voltage generated by the loop inductor and the diaphragm deflection. The combination of applied DC and AC voltage results in the electrostatic force acting on the diaphragm and can be written as (3.9)

$$F_{electrostatic} = \frac{\varepsilon_0 A_e \left(V_{DC} + V_{AC}\right)^2}{2\left(\frac{d_i}{\varepsilon_{ri}} + \left(g - x\right)\right)^2} \tag{3.9}$$

where, V_{DC}, V_{AC} are the applied DC and AC voltages, ε_0 and ε_{ri} are the permittivity of vacuum and the insulating layer, A_e is the area of the electrode, d_c and d_i are the thickness of the diaphragm and the insulation layer, g is the thickness of the air gap as shown in Figure 3.6b and x is the deflection of the diaphragm. Considering an AC voltage induced by the inductor as (3.10),

$$V_{AC} = \sqrt{2} V_{rms} \cos \omega t \tag{3.10}$$

Where, V_{rms} is the RMS voltage of the AC component and ω is the angular frequency in rad/sec. The electrostatic force can be expressed as (3.11),

$$F_{electrostatic} = \frac{\varepsilon_0 A_e \left(V_{DC}^2 + V_{rms}^2 + 2\sqrt{2} V_{DC} V_{rms} \cos \omega t + V_{rms}^2 \cos 2\omega t\right)}{2\left(\frac{d_i}{\varepsilon_{ri}} + \left(g - x\right)\right)^2} \tag{3.11}$$

The first term is the electrostatic force generated due to the DC bias voltage, the second term due to the RMS voltage of AC component, third and fourth terms are the force exerted by the voltage oscillating at the frequency equal to and twice the frequency of incident signal. As the operating frequency is well above the mechanical resonant frequency, the mechanical inertia of the diaphragm highly degrades any high-frequency vibration, hence, the signal does not modulate the diaphragm capacitance at microwave frequencies but the RMS value of the signal influences the capacitance [3]. So, the third and fourth terms can be neglected. Then the electrostatic force can be simplified as (3.12),

$$F_{electrostatic} = \frac{\varepsilon_0 A_e \left(V_{DC}^2 + V_{rms}^2\right)}{2\left(\frac{d_i}{\varepsilon_{ri}} + \left(g - x\right)\right)^2} \tag{3.12}$$

From equation (3.12), it is obvious that, to obtain measurable deflection due to applied AC voltage apart from the deflection due to constant DC voltage, values of V_{rms} and V_{DC} must be comparable. The capacitance generated [34] between the electrodes can be calculated using (3.13)

$$C = \frac{\varepsilon_0 A_e}{\frac{d_m}{\varepsilon_{rm}} + \frac{d_i}{\varepsilon_{ri}} + \left(g - x\right)} \tag{3.13}$$

From (3.9) and (3.13), it is observed that the capacitance between the plates can be measured from the diaphragm deformation caused by the inductor induced voltage. According to [34], for small diaphragm parallel plate capacitors, the

contribution of fringing field capacitance is as high as 9% of the capacitance. The total capacitance taking fringing field into account can be expressed as [34],

$$C_{MEMS} = C(1 + C_{ff}) \tag{3.14}$$

Where, C is the capacitance generated from (3.13) and C_{ff} is the fringing field factor [34] and can be expressed as (3.15),

$$C_{ff} = \frac{0.385}{a}\left[\frac{d_i}{\varepsilon_{ri}} + g\right] + 1.06\left[\frac{1}{2a}\left(\frac{d_i}{\varepsilon_{ri}} + g\right)\right]^{0.75} \tag{3.15}$$

where, a is the half side length of the square diaphragm. The capacitance contributed by the fringing field can be assumed to be constant as the diaphragm edges are rigidly fixed. Thus, the total capacitance generated by the Pixel capacitor due to the voltage induced across the inductor because of an incident signal after reflection from a tissue interface can be calculated using (3.14).

CHAPTER 4

HUMAN THORAX IMAGING

In this chapter, a multi-section transmission line model is used to analytically calculate the attenuation of an UWB radar signal as it propagates through the different tissue layers in a human thorax. The analytical model is validated with the FDTD simulation results published in [37]. The model has been used to investigate the feasibility of using the proposed MEMS microwave Pixel based UWB radar for a coronal scanning of human thorax to detect chest wall abnormalities and Pneumothorax condition.

4.1. Human Thorax Anatomy

In this section, the feasibility of using the proposed MEMS microwave Pixel for coronal scanning of human thorax to detect chest wall (which includes skin, fat, muscles, and the thoracic skeleton) abnormalities and for detecting Pneumothorax, a critical condition that occurs when air enters pleural cavity (the space between the chest wall and the lung) has been investigated. Thorax scanning for diagnosing various stages of Pneumothorax requires the UWB signal to penetrate deep into the human body until it reaches the cartilage/lung interface. Presence of air in pleural cavity changes the amount of signal reflected and the mapping of reflected signals can determine the stage of the disease. A horizontal section of the human thorax anatomy highlighting different tissue layers is shown in Figure 4.1.

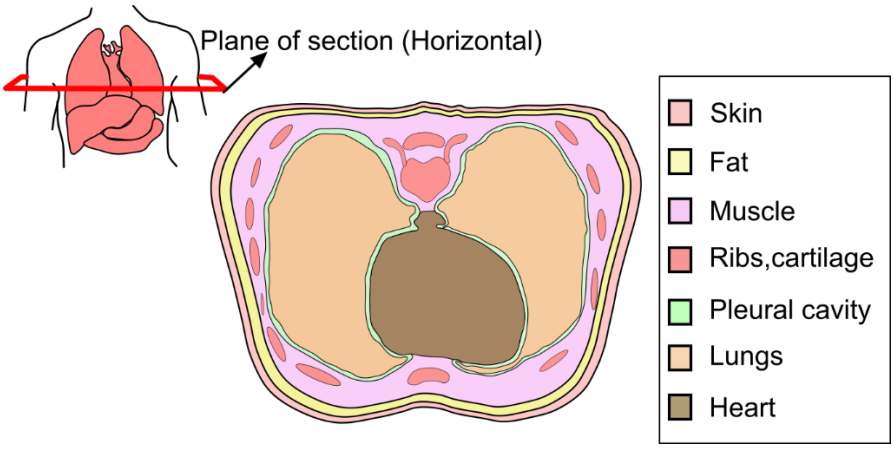

Figure 4.1. Horizontal section of human thorax.

The author in [35] discussed a more accurate thorax model determining the propagation path for UWB signal to reach the heart wall via skin-fat-muscle-cartilage-lung as shown in Figure 4.2. The thicknesses (depth) of these tissue layers as shown in Figure 4.2 correspond to that of an average adult [35]; however, in reality, they may vary from person to person.

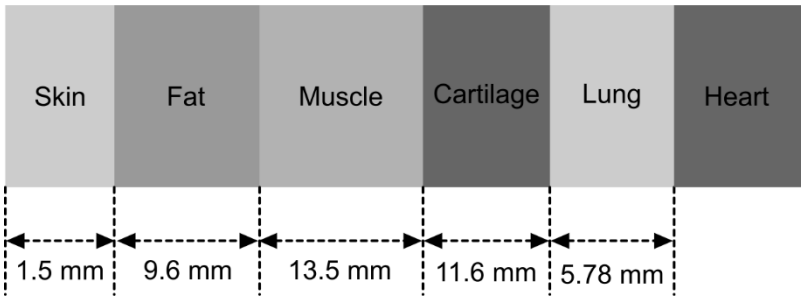

Figure 4.2. Human thorax model indicating the depth of the tissues [35].

4.2. Analytical Model to Determine the Propagation Loss

As discussed in chapter 2, the frequency dependent complex permittivities of various human tissues are the key parameters to determine the level of interaction and attenuation of a propagating UWB signal as it travels through the

thorax [12]. The frequency dependent complex permittivities of various tissues in the human thorax model in the frequency range of 3.1 GHz to 10.6 GHz are listed in Table 4.1.

TABLE 4.1 COMPLEX PERMITTIVITY OF FEW OF THE HUMAN THORAX TISSUES IN UWB FREQUENCY RANGE.

Frequency (GHz)	Skin	Fat	Muscle	Cartilage	Lung	Heart
3.1	37.36-j10.41	5.21-j0.78	51.94-j12.88	37.40-j13.28	20.07-j5.81	53.552-j16.36
4.1	36.51-j10.55	5.12-j0.83	50.69-j13.64	35.36-j14.05	19.48-j5.95	51.79-j16.79
5	35.77-j11.00	5.03-j0.87	49.54-j14.54	33.63-j14.69	18.97-j6.19	50.27-j17.48
6	34.95-j11.66	4.94-j0.92	48.22-j15.58	31.79-j15.26	18.39-j6.49	48.62-j18.34
7	34.08-j12.37	4.85-j0.96	46.87-j16.59	30.07-j15.68	17.82-j6.81	46.99-j19.18
8	33.18-j13.09	4.76-j0.99	45.49-j17.52	28.47-j15.97	17.26-j7.09	45.37-j19.97
9	32.25-j13.77	4.68-j1.03	44.13-j18.36	26.99-j16.14	16.69-j7.34	43.79-j20.67
10	31.29-j14.49	4.60-j1.05	42.76-j19.10	25.63-j16.22	16.15-j7.56	42.24-j21.27

From Table 4.1, it is evident that the complex permittivities of different thorax tissues vary significantly at different UWB frequencies. This variation can be exploited effectively to realize an UWB radar based thorax imaging system. In the proposed scheme, the signals reflected back from the different tissue layers in

the thorax as shown in Figure 4.2 will illuminate a 2D array of MEMS microwave Pixels incorporated in the UWB radar to generate a corresponding 2D voltage map which is characteristic of the complex permittivities of the respective tissue layer. To determine the strength of the reflected UWB signal, that is going to illuminate the MEMS microwave Pixel array, it is necessary to consider the transmission loss, absorption loss, and reflection loss associated with the propagating UWB signal. A mathematical model developed in [36] for UWB signal attenuation in tissues for biomedical implant communication has been extended to the present application of thorax imaging. In this method, classical transmission line theory has been used to model the human thorax as shown in Figure 4.2. Each tissue layer is modeled as a transmission line and the results are combined to generate a cascaded transmission line model of the multilayered thorax. [36].

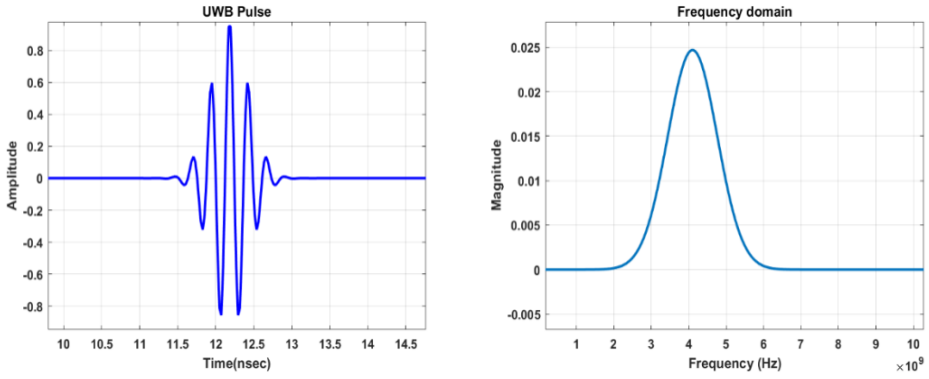

Figure 4.3. Gaussian pulse representation in (a) time domain and,(b) frequency domain.

The proposed UWB system operates in the frequency range of 3.1 GHz to 5.1 GHz, with center frequency at 4.1 GHz. Typically, the signals used for UWB applications are a step-like pulse, impulse, rectangular pulse, monocycle and polycycle pulse. Here, a Gaussian pulse of 400 ps pulsewidth (half maximum point)

with a center frequency of 4.1 GHz and pulse repetition period (PRP) of 1.8 ns is employed. The time domain and frequency domain representation of generated Gaussian pulse is shown in Figure 4.3.

A transmission line model as shown in Figure 4.4 has been used to determine the propagation loss as the transmitted signal travels through the thorax to reach the lung/heart interface. As the signal travels from a source to a load via transmission lines with varying impedances as shown in Figure 4.4b, it suffers reflection at each discontinuity (impedance variation). To avoid the complexity of calculating multiple wave reflections at each discontinuity, it is more straightforward to calculate voltage and current at each discontinuity in terms of voltage and current at the next discontinuity [36] using

$$\begin{bmatrix} V_i \\ I_i \end{bmatrix} = [T_i] \begin{bmatrix} V_{i+1} \\ I_{i+1} \end{bmatrix} = \begin{bmatrix} A & B \\ C & D \end{bmatrix} \begin{bmatrix} V_{i+1} \\ I_{i+1} \end{bmatrix} \tag{4.1}$$

Where, V_i and I_i represents the voltage and current at $i\text{th}$ discontinuity in the direction of the source to load. T_i represents the transmission matrix (also referred as ABCD matrix) of the $i\text{th}$ section of the transmission line.

The same solution approach is applied to microwave signal propagation through human tissues considering electric field component E and magnetic field component H as analogues to voltage V and current I [36]. This analogy can be used to model Individual homogeneous tissue layers as transmission lines in the form of $ABCD$ matrices using (4.2). The cascaded $ABCD$ matrix of individual layers represents the entire non-homogeneous layered sandwich structure as in

(4.3).

$$\begin{bmatrix} E_i \\ H_i \end{bmatrix} = \begin{bmatrix} T_i' \end{bmatrix} \begin{bmatrix} E_{i+1} \\ H_{i+1} \end{bmatrix} \tag{4.2}$$

$$[T_{total}] = [T_1][T_2][T_3][T_4][T_5][T_6] \tag{4.3}$$

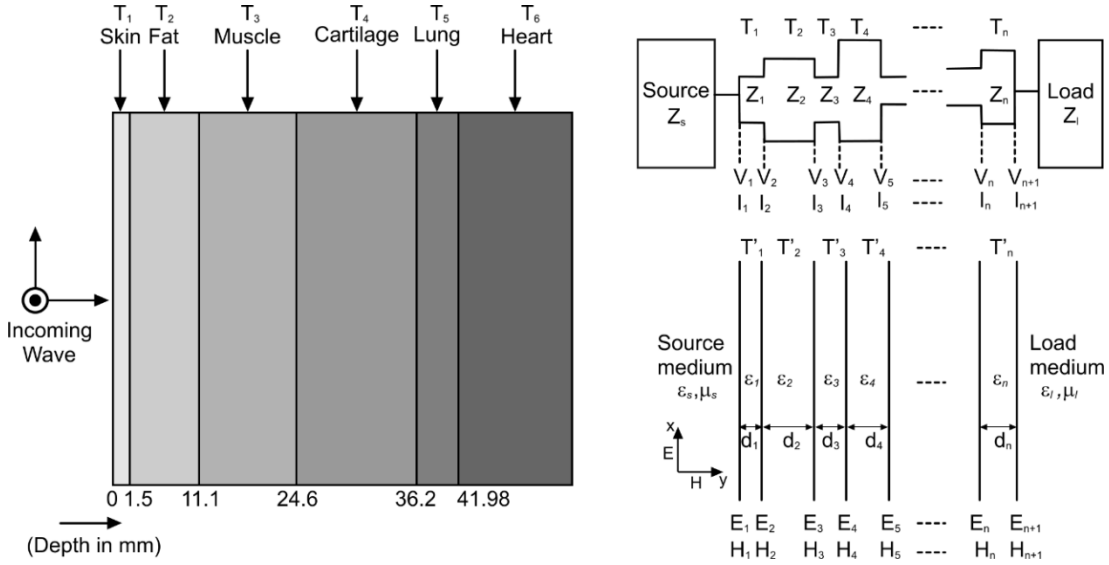

Figure 4.4. a) Human Thorax model, b) A wave propagation path with different dielectric materials analogues to transmission line model with varying impedance [34].

The transmission matrix of ith layer (4.2) depends on its propagation constant, thickness and characteristic impedance according to (4.4) where γ_i is the complex propagation constant of the ith layer, d_i is the thickness of the ith layer, and η_i is the complex impedance of the ith medium.

$$\left[T_i'\right]=\begin{bmatrix}A_i & B_i\\ C_i & D_i\end{bmatrix}=\begin{bmatrix}\cosh\gamma_i d_i & \eta_i\sinh\gamma_i d_i\\ \dfrac{\sinh\gamma_i d_i}{\eta_i} & \cosh\gamma_i d_i\end{bmatrix} \tag{4.4}$$

This mathematical model is implemented in MATLAB® to predict the attenuation of an incident UWB radar signal as it makes its way to reaching the lung/heart interface via different dielectric layers of the Thorax model. It has been

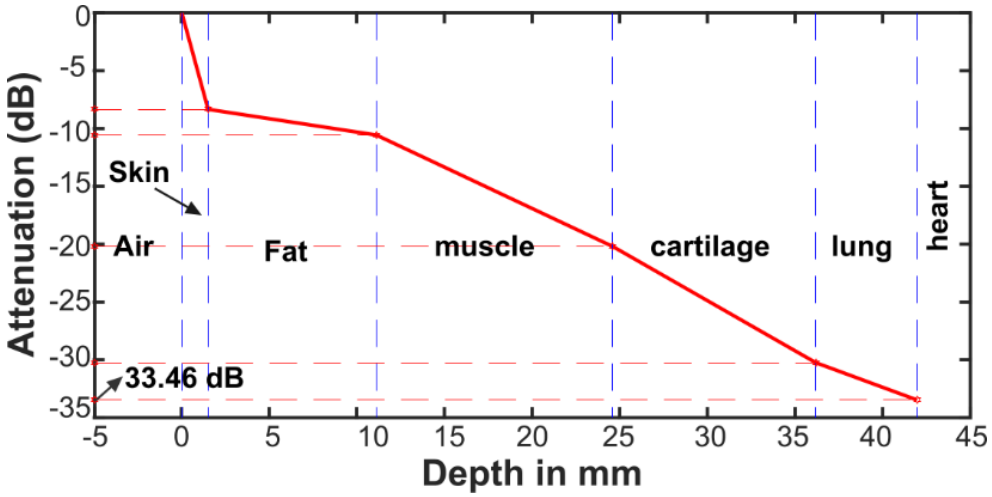

Figure 4.5. Mathematical model predicted one -way attenuation of UWB signal propagating into human thorax model at 4.1 GHz.

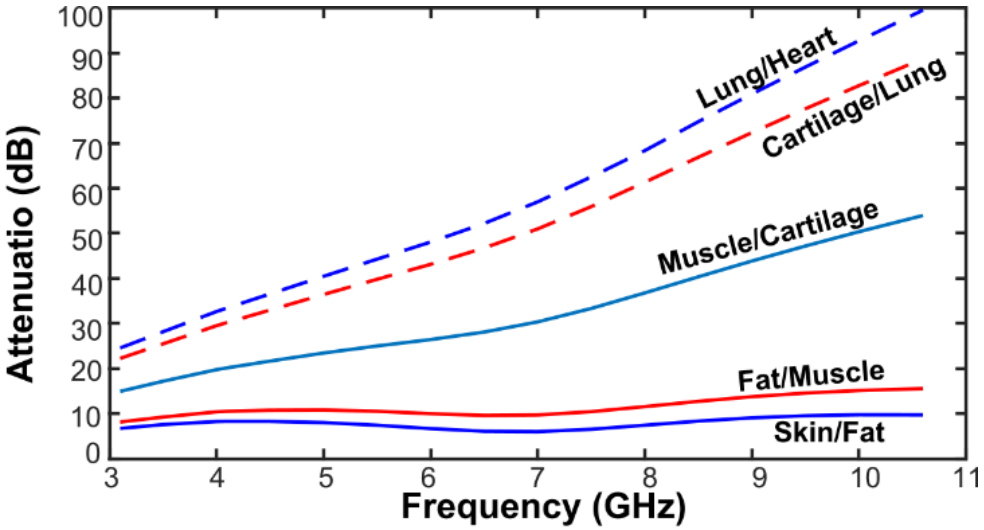

Figure 4.6. Analytical attenuation results for human thorax model at different interfaces with frequency.

calculated that for an UWB signal with the center frequency at 4.1GHz faces an attenuation of 66.93 dB in its round trip from the skin to the lung/heart interface as shown in Figure 4.5. Figure 4.6 shows that higher frequency components of UWB signal undergoes significant attenuation by human tissues and the attenuation by deeper tissues are more dependent on frequency.

4.3. FDTD Simulation of Thorax Model

The same sandwich geometric configuration of human thorax model discussed in the previous section is simulated using Remcom® Xfdtd®, an electromagnetic simulator. The designed model is excited with a Gaussian pulse

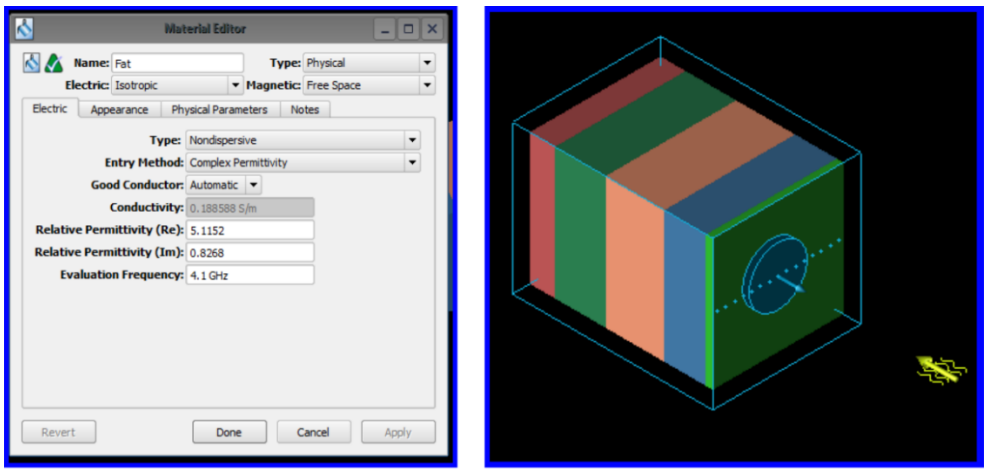

Figure 4.7. Simulation setup of human thorax model in Remcom® XFdtd®.

of 0.4ns pulsewidth, with pulse repetition period of 1.6 ns. and an electric field of 1 Vm^{-1}. Remcom® Xfdtd® software allows to observe the time evaluation patterns of both Electric and magnetic fields at any user defined point in simulation space. The stacked multilayered model simulated is shown in Figure 4.7b and the material

editor corresponding to fat layer is shown in Figure 4.7a.

As the electromagnetic wave generated by the planewave source placed in front of the human thorax passes through the different tissue interfaces it gets reflected at dielectric boundaries at the interfaces of adjacent layers. The energy density associated with electric and magnetic fields is defined by a vector called Poynting vector (S). It represents the rate of energy transfer per unit area (Wm^{-2}). Also, the direction of the Poynting vector defines the direction of propagation of wave energy. By observing the Poynting vector distribution and direction at each interface, the strength and the direction of signal propagation can be determined. In the simulation, the signal is propagating in the positive X axis direction, electric field in direction of negative Y axis and the magnetic field in positive Z direction. The Poynting vector component is represented as,

$$S_x = E_y \times H_z \tag{4.5}$$

TABLE 4.2 PROPAGATION AND ECHO TIME OF UWB SIGNAL THROUGH THORAX MODEL.

Tissue Interface	Propagation time		Time for the echo to reach the sensor placed outside the skin (μs)
	Analytical (ps)	Xfdtd® (ps)	
Skin/Fat	107.7134	102.551	0.000205102
Fat/Muscle	180.5134	177.565	0.00035513
Muscle/Cartilage	506.5634	487.118	0.000974236
Cartilage/Lung	745.0934	701.716	0.001403432

The time taken by the UWB radar signal to reach each interface is calculated as

shown in Table 4.2, It is observed that the variation from the analytical model increases as the signal penetrates deeper into the body. The reflected signal at each interface is expected to return at twice the one-way propagation time as shown in Table 4.2. The magnetic field distribution at a perpendicular plane placed at 2mm outside the air/skin interface at the expected echo time according to the Table 4.2 are plotted as shown in Figure 4.8.

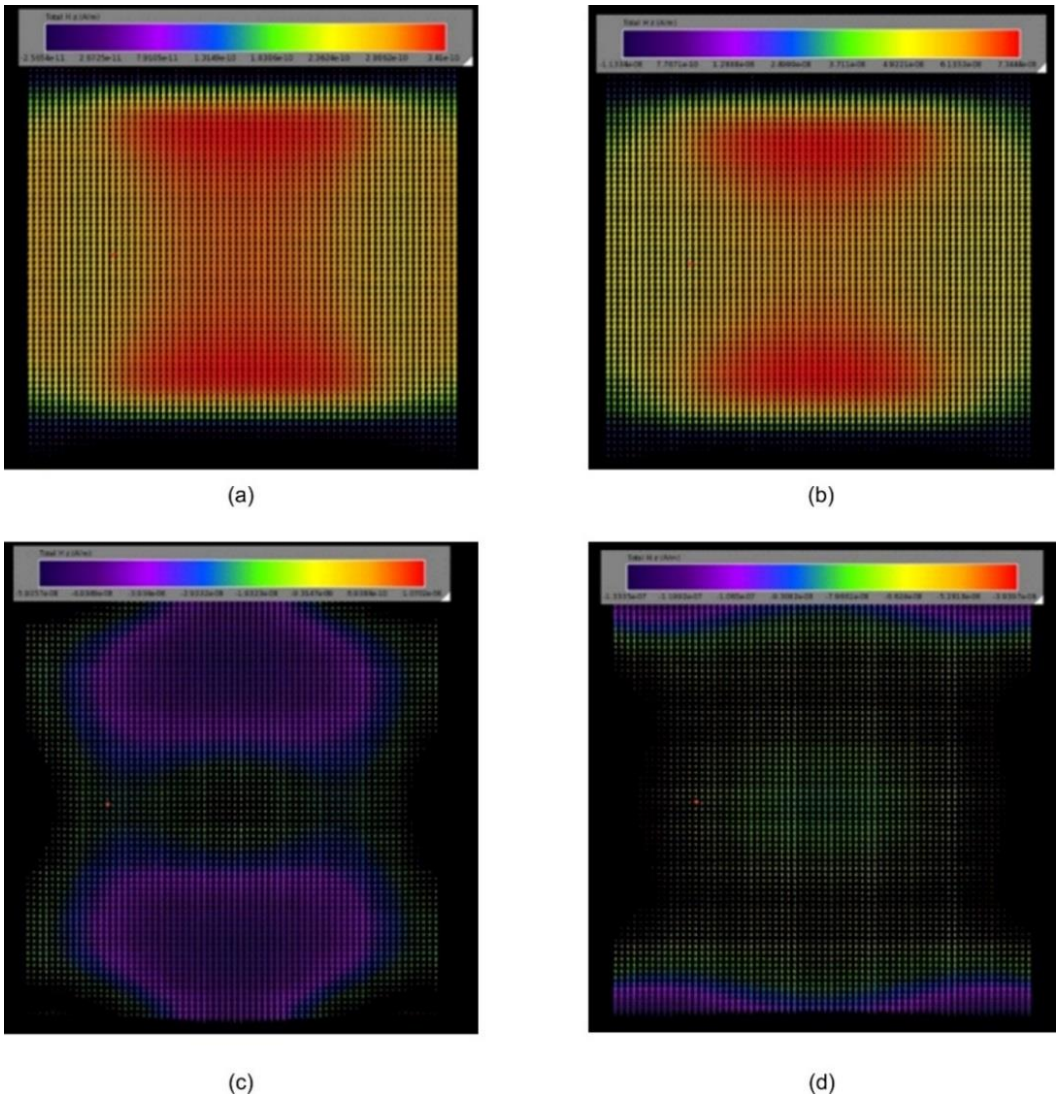

Figure 4.8. Magnetic field distribution. a) at t=0.205 ns, b) at t=0.35 ns, c) at t=0.97 ns, d) t=1.4 ns.

From Figure 4.8, it is observed that the signals reflected from the deeper tissues are quite harder to detect due to high signal attenuation.

4.3.1. Analytical model validation

Results obtained from the above mathematical models are validated with Finite Difference Time Domain (FDTD) simulation results presented in [37]. The total one-way attenuation of an UWB signal as it propagates through the thorax deep to the lung/heart interface was obtained around 31dB using FDTD simulation as presented in [37]. The attenuation calculated from the present analytical model is about 33.46 dB as shown in Figure 4.9. Both the results are in excellent agreement with a maximum deviation of 7.9%. This validates the accuracy of the developed analytical method.

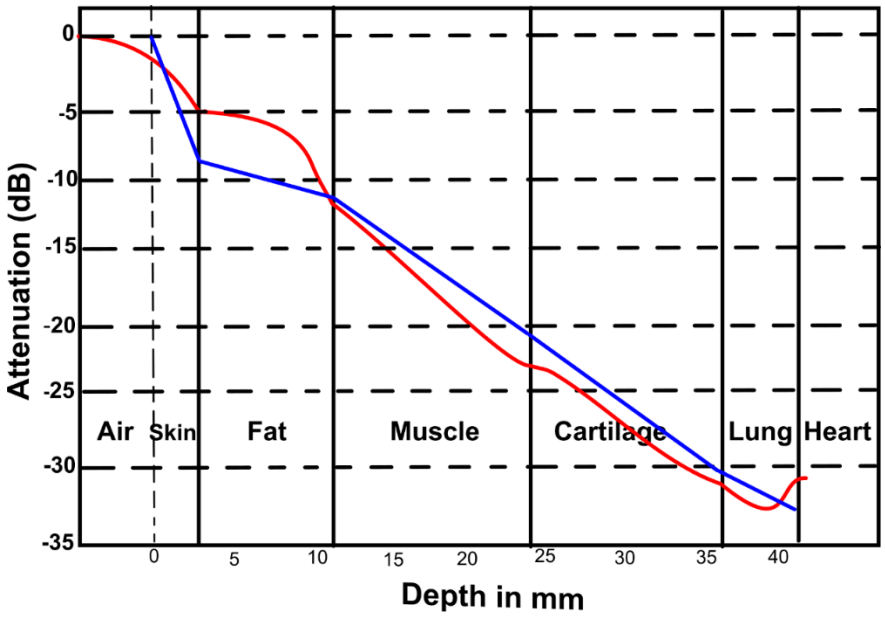

Figure 4.9. Analytical and simulated results for attenuation of UWB signal propagating into the human thorax model.

CHAPTER 5

MEMS PIXEL DESIGN FOR HUMAN THORAX IMAGING

This chapter presents the design of the developed microwave Pixel for human thorax imaging application. A mathematical model to determine the power level of the reflected signals from each tissue interface is presented. The circuit level simulation of Pixel inductor in OrCAD® PSpice® and the FEM simulation of Pixel capacitor are presented. Finally, the design and performance specifications of the developed microwave Pixel are presented.

5.1. Determination of Power Levels that to be Detected by the Proposed Pixel

It has been assumed that an UWB radar as shown in Figure 2.4 is placed sufficiently far away from the thorax to enable a far field approximation. The radar is radiating an output power P_t (Watts) through a transmitting antenna with a gain G_1. The transmitted power density at a distance R_1 (the standoff distance from the thorax), can be expressed as (5.1),

$$P = \frac{P_t}{4\pi R_1^2} G_1 \tag{5.1}$$

The human heart can be modeled as a spherical isotropic radiator which reflects a spherical wave with same incident wave polarization [38]. The typical adult heart has a size of 12 cm in length, 8-9 cm in breadth and 6 cm in thickness. Thus, assuming the heart as a sphere of 12 cm diameter as shown in Figure 5.1, the

signal reflected off the heart depends on the radar cross-section (RCS) σ which depends on the area of the target, its reflectivity and gain of the target [38].

$$\sigma = \left| A_t . \Gamma . G_t \right| \tag{5.2}$$

In (5.2) A_t is the projected area of the target, Γ is the reflectivity of the target, G_t is the antenna-like gain of the target. A heart with 12 cm diameter is comparable to the wavelength of the incident signal at 4.1 GHz. Hence, following [39], a sphere of 12 cm falls in the region of Mie or Resonance region of sphere RCS. From the graph in Figure 5.2, $(\sigma/\pi r^2)$ is approximately equal to 0.9 when $(2\pi r/\lambda)$ equals 5.16. Therefore, the projected area of heart from radar perspective is about 0.9 times the area of the human heart which equals to 0.01 m^2. The reflectivity (Γ) of lung/heart interface is obtained from (5.3) where Z_{Heart} and Z_{Lung} are the propagation impedances of the heart and the lung where the propagation impedance is calculated following (5.4). The complex permittivity ε of the heart and the lung at 4.1 GHz are determined in Table 4.1.

$$Y = \frac{z_{Heart}}{z_{Lung}} \; ; \Gamma = \frac{Y-1}{Y+1} \tag{5.3}$$

$$Z = \sqrt{\frac{\mu_0}{\varepsilon_r \varepsilon_0}} \tag{5.4}$$

Assuming gain as 1, the reflectivity at heart/lung interface is calculated to be 0.23. The RCS of the heart can be calculated following (5.2) as 0.0023. The received

power available at the microwave Pixel array placed at a distance of R_2 from the human target can be calculated following

$$P_r = \left(\frac{P_t G_t}{4\pi R_1^2}\right)\left[\frac{\sigma}{4\pi R_2^2}\right]\frac{1}{L} \tag{5.5}$$

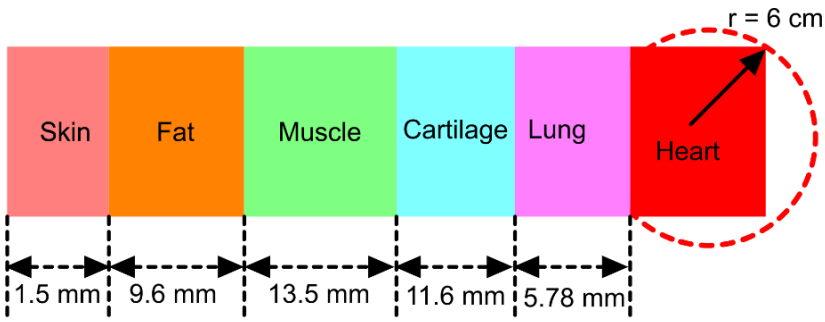

Figure 5.1. Thorax model assuming heart as a sphere of diameter 12 cm.

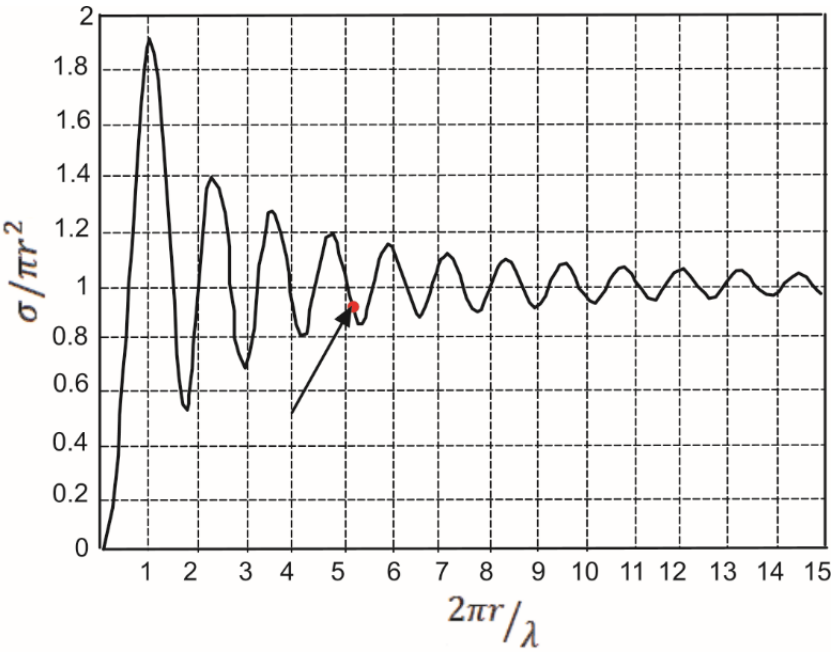

Figure 5.2. Normalized backscattered RCS for a perfectly conducting sphere [37].

where, L represents the propagation loss which includes reflection, absorption losses of the signal when propagated through Skin, fat, muscle, cartilage and lung.

TABLE 5.1 CASE 1: POWER TRANSMITTED P_t = 5 mW.

Depth	Power Received ($\mu W/m^2$)	Magnetic field Strength of received signal ($\mu A/m$)
Skin/Fat	19.58	227.91
Fat/Muscle	8.01	145.75
Muscle/Cartilage	0.016	6.6
Cartilage/Lung	0.00026	0.836
Lung/heart	0.000097	0.507

TABLE 5.2 CASE 2: POWER TRANSMITTED P_t = 50 mW.

Depth	Power Received ($\mu W/m^2$)	Magnetic field Strength of received signal ($\mu A/m$)
Skin/Fat	195.833	720.73
Fat/Muscle	80.086	460.9
Muscle/Cartilage	0.164	20.85
Cartilage/Lung	0.0026	2.646
Lung/heart	0.00097	1.602

The total two-way propagation loss is calculated to be twice the 33.46875 dB from the analytical model as shown in Figure 4.5, which is equal to 66.9375 [dB]. The thorax is placed at a distance of 10 cm from the transmitting antenna and 4.8 cm

from the Pixel array. The estimation of power available for Pixel array at three different transmitted power levels is calculated using (5.5), as shown in Tables 5.1, 5.2 and, 5.3. When Pt = 500 mW, the incident power density on skin which is 10 cm from antenna is calculated to be 3.979 W/m^2 which is well below the radiation safety limit of 10 W/m^2 [22].

TABLE 5.3 CASE 3: POWER TRANSMITTED P_t = 500 mW.

Depth	Power Received (W/m^2)	Magnetic field Strength of received signal (mA/m)
Skin/Fat	0.00196	2.279
Fat/Muscle	0.0008	1.457
Muscle/Cartilage	1.64×10^{-6}	0.0669
Cartilage/Lung	2.64×10^{-8}	0.0084
Lung/heart	9.68×10^{-9}	0.0051

5.2 MEMS Microwave Pixel Design Specifications

According to the present application of thorax imaging using UWB radar operating in the frequency range of 3.1 GHz to 5.1 GHz, the Pixel inductor must be capable of detecting the magnetic field of intensity ranging from 10^{-2} Am^{-1} to 10^{-7} Am^{-1} as per Tables 5.1, 5.2 and 5.3 for the considered transmit power levels. Any change in voltage induced across the loop inductor, generates a corresponding capacitance change (ΔC) across the MEMS capacitor, which is placed in parallel to the loop inductor. A major limitation on the Pixel design, for imaging deeper

tissues of human thorax, is imposed by the sensitivity of the readout circuitry which senses this capacitance change.

5.2.1. Circuit Operation

To understand the behavior of the loop inductor connected in parallel to the designed capacitive sensor, a combined electrical equivalent circuit as shown in Figure 5.3 is simulated in OrCAD® PSpice®. The Pixel circuit parameters are swept and iteratively calculated using equations (3.3) – (3.8), to determine the optimal set of parameters that would generate a detectable and a flat response of the voltage across the capacitor over the desired bandwidth.

The self-inductance and self-capacitance of the loop inductor determine its self-resonant frequency and it is supposed to be lower than the operating frequency, for the ensured inductive behaviour of the loop inductor. The frequency response of the loop inductor as a function of N keeping other parameters as constant is as shown in Figure 5.4. The self-resonant frequencies (marked as $f_1, f_2, f_3 \ldots\ldots f_{10}$ in Figure 5.4) of loop inductor with different N values are listed in Table 5.4. From Figure 5.4, it is observed that the voltage induced across the loop inductor is directly proportional to the number of turns and it is observed that the frequency response curve shows sharper resonant peaks with an increase in number of turns, N. It is observed that the loop inductor with less number of loops shows high resonant frequency, this can be justified by the fact that the inductance of the loop decreases with a decrease in N value. From Table 5.4, a decrease of 99.7% of bandwidth is observed, when N is increased from 1 to 2. This shows that for the wideband operation of loop inductor the number of turns should be as

low as possible.

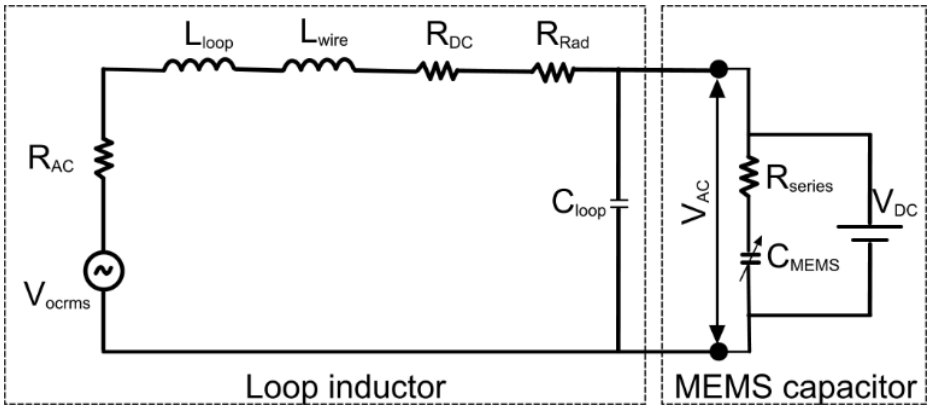

Figure 5.3. Electrical equivalent circuit of the proposed microwave Pixel.

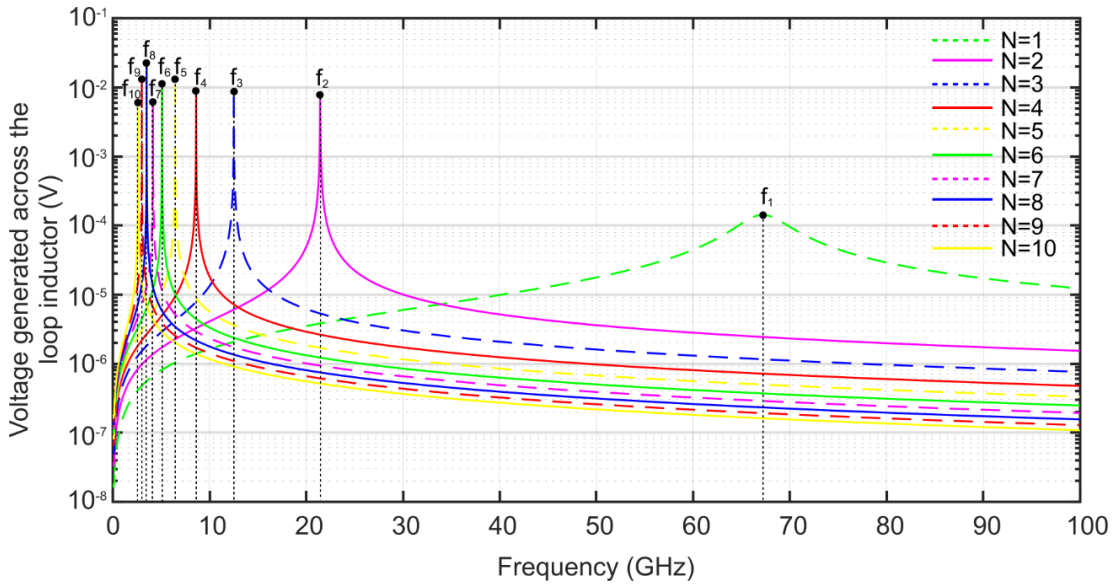

Figure 5.4. Frequency response of the loop inductors with different N values.

The spiral inductor in parallel to the MEMS capacitor forms an LC parallel circuit with a small resistance in series to the inductor and to the MEMS capacitor and resonates at a frequency following (5.6).

$$f_0 = \frac{1}{2\pi\sqrt{(L_{loop} + L_{wire})(C_{loop} + C_{MEMS})}} \tag{5.6}$$

TABLE 5.4. RESONANT FREQUENCY AT DIFFERENT N VALUES.

Number of turns, N	Resonant frequency (GHz)	Bandwidth, BW (MHz)
1	$f_1 = 67.22$	4990
2	$f_2 = 21.43$	15
3	$f_3 = 12.50$	1
4	$f_4 = 8.6$	0.8
5	$f_5 = 6.4$	0.5
6	$f_6 = 5.08$	0.4
7	$f_7 = 4.15$	0.3
8	$f_8 = 3.48$	0.2
9	$f_9 = 2.99$	0.15
10	$f_{10} = 2.6$	0.1

To flatten the frequency response (without resonance) of the LC parallel circuit over the desired range, a damping effect is induced by placing a resistor across the terminals of the loop inductor as shown in Figure 5.5. The desired flat frequency response of the LC circuit formed by the loop inductor with damping resistance and MEMS Pixel capacitor, can be obtained when the following two conditions are satisfied:

1) The inductive reactance of the loop along with the loop resistance should be quite higher than the damping resistance connected across the loop inductor as (5.7). Where, $X_L = X_{L_{loop}} + X_{L_{wire}}$, $R_{loop} = R_{AC} + R_{DC} + R_{Rad}$ and R_d is the damping resistance connected across the loop.

$$X_L + R_{loop} >> R_d \tag{5.7}$$

2) The capacitive reactance of the MEMS capacitor along with R_{series} and the capacitive reactance of C_{loop} should be far greater than the damping resistance as (5.8).

$$X_{C_{MEMS}} + R_{series} >> R_d ; X_{C_{loop}} >> R_d \tag{5.8}$$

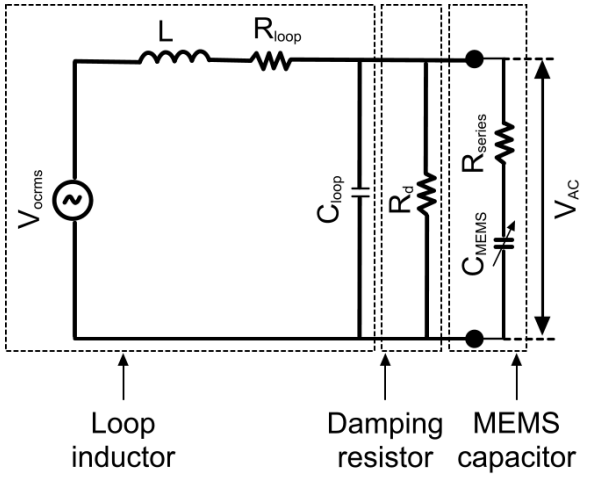

Figure 5.5. Equivalent circuit of wideband loop inductor.

Following (5.7) and (5.8), the damping resistance should be as small as possible to achieve flat frequency response over the desired frequency band, which means that the designed LC circuit needs to be operated in short circuit mode [40]. This wideband characteristic of the resultant LCR parallel circuit sacrifices the output voltage levels induced across the inductor. This trade-off trend is shown in the Figure 5.6., a voltage drop of more than 99% is observed when a resistance is connected across the inductor. Figure 5.6 shows that the designed circuit behaves like a bandpass filter with its lower cut-off frequency as expressed in (5.9) is determined by the total loop inductance $(L_{loop} + L_{wire})$ and total resistance $(R_{DC} + R_{AC} + R_d + R_{rad})$ [30].

$$f_l = \frac{(R_{DC} + R_{AC} + R_d + R_{rad})}{2\pi(L_{loop} + L_{wire})} \tag{5.9}$$

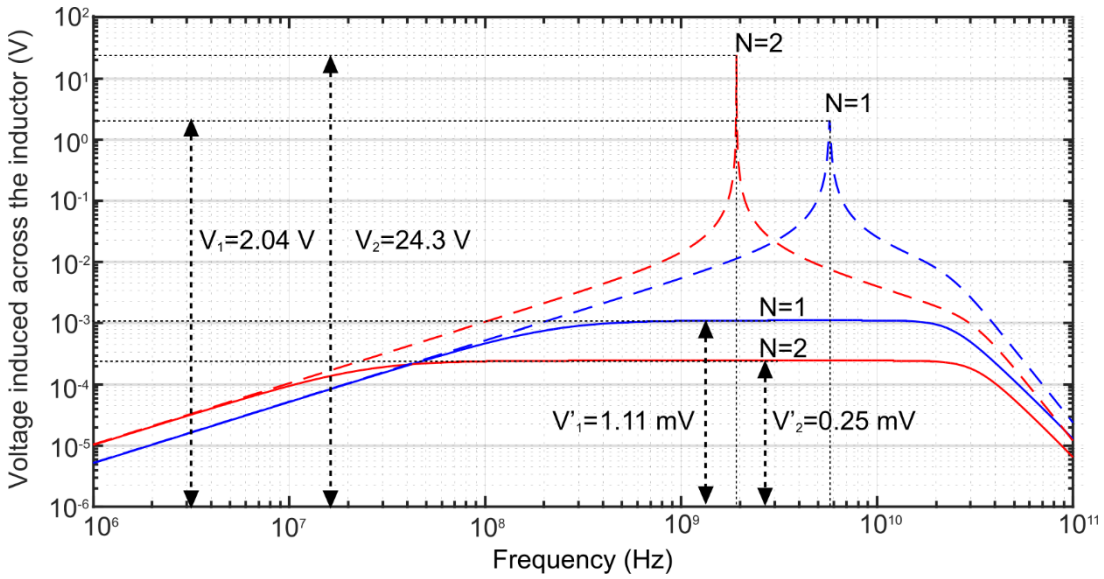

Figure 5.6. Frequency response of the loop inductor with and without damping resistance.

When a voltage is induced across the loop inductor in response to the radiation picked up and generates a loop current I_{loop} that can be expressed as (5.10), and reduced to equation (5.11) following (5.7) & (5.8).

$$I_{loop} = \frac{V_{ocrms}}{(X_L + R_{loop}) + (\frac{1}{X_{C_{loop}}} + \frac{1}{R_d} + \frac{1}{X_{C_{MEMS}} + R_{series}})} \tag{5.10}$$

$$I_{loop} \approx \frac{V_{ocrms}}{X_L + R_{loop}} \tag{5.11}$$

From (5.11), we can conclude that at low frequencies where R_{loop} dominates X_L, the loop inductor acts a resistor whereas, at high frequencies, the resistive part of the loop inductor is almost negligible compared to the inductive reactance. Thus,

following (5.11), at high frequencies both V_{ocrms} and X_L are proportional to the frequency, this makes loop current independent of frequency [30], thus we can observe flat frequency response when the loop is operated in short circuit condition, where $X_{C_{loop}}$, $X_{C_{MEMS}}$ are negligible due to the shorted damping resistance, R_d as per equation (5.10). The voltage generated across R_d can be expressed as (5.12),

$$V_{R_d} = R_d \times I_{loop} = V_{C_{loop}} = V_{AC} \tag{5.12}$$

5.2.2. Design specifications of Pixel inductor

Following (5.12), the voltage applied across the MEMS capacitor is equal to the voltage generated across R_d .Thus to generate enough capacitance change across the Pixel capacitor, the parameter that plays a vital role is the inductor loop current. From (5.11), since we are operating at high frequency, the magnitude of this loop current depends on V_{ocrms} and X_L which are functions of the physical size as (5.13).

$$I_{loop} \propto \frac{NA}{L} \tag{5.13}$$

From, Figure 5.6 and Figure 5.7, it is observed that in case of wideband operation of the loop inductor, the magnitude of the voltage generated across the damping resistance decreases with the increase in number of turns. The output voltage for a single turn square loop is 4.5 times than that of the voltage generated by a two-turn square loop. This is because, from (3.2), (3.6), and (5.13) doubling

N increases V_{ocrms} by 2 times and inductance by 4 times and the I_{loop} decreases by 2 times, which results in the reduction of voltage across the damping resistance. Thus, a single turn square loop has been selected for the proposed design.

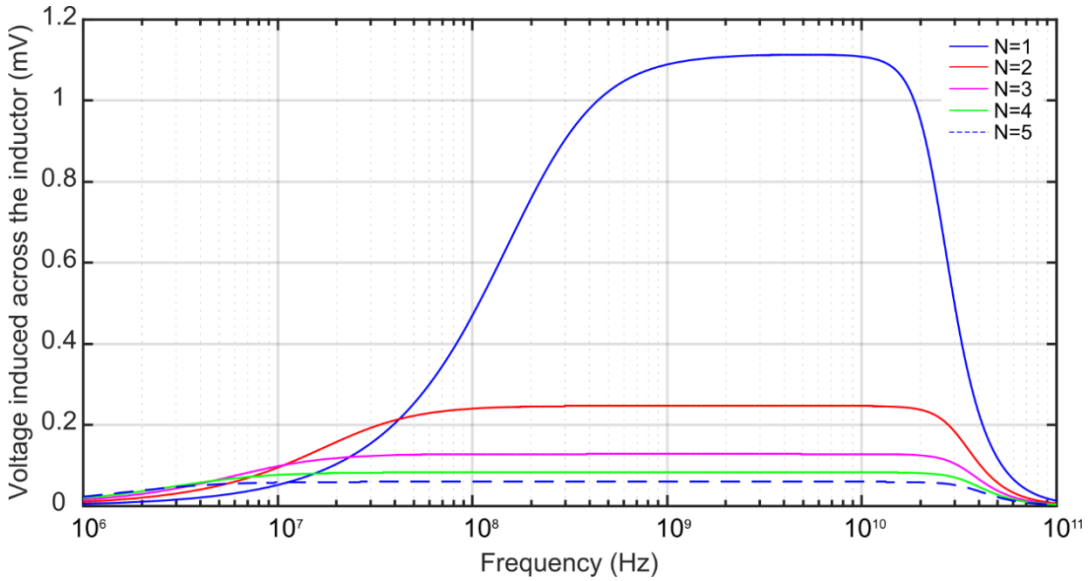

Figure 5.7. Voltage generated across the loop inductor, shunted with a resistance, as a function of N.

From (5.13), since N is chosen to be 1, the loop current depends on A/L ratio. Though the loop current increases with increase in area, large loop size sacrifices the resolution of the image generated. So, the choice of increasing the loop size can be omitted and the only way to obtain the desired output voltage level is by reducing the loop inductance. Loop inductance can be reduced by increasing the width of the conductor but from Figure 3.5a, it is observed that the increment in this case, is not significantly high. So, the alternate way to reduce the loop inductance is by using crossed parallel loops [40].

Crossed parallel loops as shown in Figure 5.8, are the loops connected in

parallel in such a way that the induced currents are added with minimal mutual coupling. From Figure 5.8, it is observed that the current direction of adjacent arms of the successive inductors is made to oppose each other to reduce the mutual inductance between them. With this configuration of loops, the effective inductance is lowered and the short circuit current is increased within the same area of operation [40].

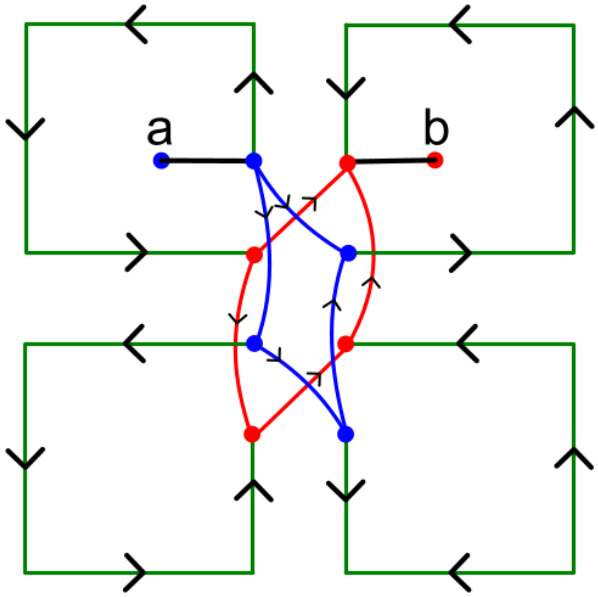

Figure 5.8. Parallel crossed loops with their current direction.

Using this technique of crossed parallel loops, for the same total area, a single loop is replaced by an array of small loops which are named as sub-Pixel loops. Circuit simulations are carried out in PSpice®, by varying the number of sub-Pixel loops (n_s), the length of the conductor (w) and, the width of the conductor (d). Different combinations of loops, for the same total area, are simulated as listed in Table 5.5. As it is evident from Table 5.5, with an increase in number of

sub-Pixel loops maintaining the same total area, there is a considerable increase in loop current.

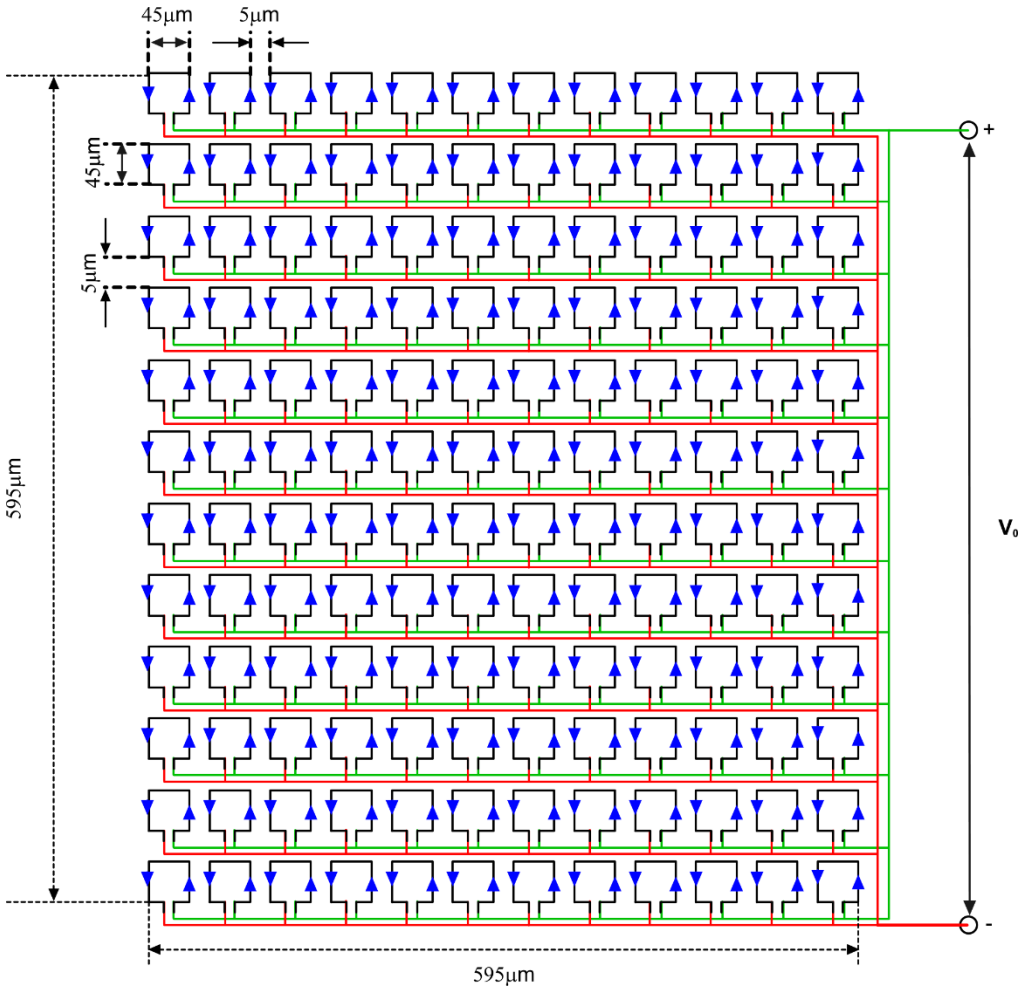

Figure 5.9. 12×12 Sub-Pixel matrix showing their connections (dimensions are not to scale).

Considering case 1, a loop area of 0.01 μm^2 , the reduction of loop inductance of about 8 times and 66 times is observed for 4 loops of each 0.0025 μm^2 and 16 loops of each 0.625 nm^2, while an increase in loop current is about 2 times and 4 times. From case 1, case 3 and case 4, halving the side length of the square loop, the inductance is reduced by 8 times and the loop current is increased by 2 times. With the increase in the ratio of loop length of the large loop to the sub-loop, their

ratio of loop currents is increased.

TABLE 5.5 COMPARISON OF LOOP INDUCTANCE, LOOP RESISTANCE AND LOOP CURRENT OF VARIOUS COMBINATIONS FOR THE SAME TOTAL AREA AT 4.1 GHz FREQUENCY.

	Loop Inductor	**Inductance** (nH)	**Resistance** (Ω)	**Current** (μA)
Case 1	• Single turn loop 100μm×100μm	28.010	15.066	4.322
	• 4 sub loops 50μm×50μm	3.463	1.871	8.765
	• 16 sub loops 25μm×25μm	0.424	0.234	17.947
Case 2	• Single turn loop 300μm×300μm	84.787	53.6796	12.797
	• 9 sub loops 100μm×100μm	3.112	1.674	38.90
	• 100 sub loops 30μm×30μm	0.082	0.045	133.580
Case 3	• Single turn loop 500μm×500μm	142	142.75	21.226
	• 4 sub loops 250μm×250μm	17.65	10.410	42.732
	• 25 sub loops 100μm×100μm	1.12	0.603	108.055
Case 4	• Single turn loop 600μm×600μm	170	230.673	25.419
	• 4 sub loops 300μm×300μm	21.197	13.420	51.188
	• 144 sub loops 50μm×50μm	0.096	0.052	315.533

Note: All the other parameters are kept constant and the current shown is through damping resistance of 5 Ohms.

Keeping these conclusions in mind, the optimal set of the parameters of the Pixel inductor is determined as shown in Table 5.6. Gold has been selected as the

material for the loop inductor due to its high conductivity and ease of microfabrication. The Pixel inductor has a total footprint area of 595 µm x 595 µm with total inductance of 86.382 pH. Each Pixel inductor has an array of 12×12 sub-Pixels (small loops) each with the size of 45 µm with a gap of 5 µm between adjacent sub-Pixel loops in an array. Each sub-Pixel loop has an inductance of 12.439 nH. To increase the induced voltage across the Pixel inductor, a magnetic core made of Fe-Co-B with high permeability of 1000 is chosen [41]. The connections among sub- Pixel loops are as shown in Figure 5.9.

TABLE 5.6 DESIGN PARAMETERS OF PIXEL INDUCTOR.

	Parameter	**Value**
Pixel Parameters	Pixel inductor area	595 µm × 595 µm
	Pixel Inductance	86.382 pH
Sub-Pixel parameters	Gap between the sub Pixel loops, g_s	5 µm
	Length of the square loop, w	45 µm
	Number of turns, N	1
	Width of the conductor, d	1 µm
	Number of sub Pixel, n_s	144
	Thickness of the conductor, t_d	1 µm
	Relative permeability of medium, μ_r	1000
	Sub Pixel inductance, L	12.439 nH
	Conductor (gold) resistivity, ρ	2.44×10^{-8} Ωm

5.2.3. Design specifications of the Pixel capacitor

The capacitance of the MEMS variable capacitor (Pixel capacitor) is changed according to the voltage generated across the resistor connected in parallel the loop inductor. As discussed in Chapter 3, the two-important design

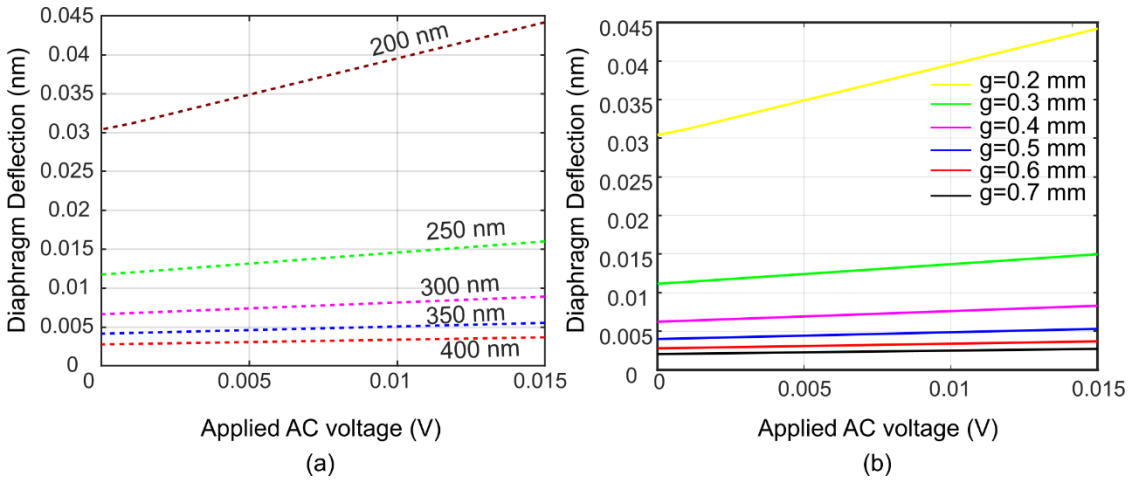

Figure 5.10. Diaphragm deflection with voltage, a) at different diaphragm thickness, b) at different airgap.

TABLE 5.7 PULL-IN VOLTAGE AT DIFFERENT DIAPHRAGM THICKNESS.

Thickness of the diaphragm (nm)	Pull-in Voltage (V)
150	0.108
200	0.146
250	0.214
300	0.290
350	0.365
400	0.440

goals of Pixel capacitor are to obtain adequate sensitivity to sense a very low voltage induced by the inductor when it is operated to collect echo signals from the

deeper tissues of the human body and to obtain a flat frequency response of the Pixel over a UWB frequency range of 3.1 GHz to 5.1 GHz. The sensitivity of the Pixel capacitor can be defined as the change in capacitance (ΔC) with respect to the change in voltage applied (ΔV).

TABLE 5.8 PULL-IN VOLTAGE WITH RESPECT TO AIRGAP.

Airgap (µm)	Pull-in Voltage (V)
0.1	0.063
0.2	0.146
0.3	0.275
0.4	0.42
0.5	0.56
0.6	0.78
0.7	0.9

To address the first goal, a very thin pure metal based diaphragm is used to achieve high sensitivity. A parametric FEM analysis has been carried out by varying the diaphragm thickness from 200 nm to 400 nm for the same applied voltage as shown in Figure 5.10a to determine the optimum thickness of the diaphragm that can generate the highest capacitance change. From Figure 5.10a, it is observed that as the thickness of the diaphragm decreases, its deflection to low voltage increases as its pull-in point reduces with the thickness which in shown in Table 5.7. The effect of airgap on diaphragm deflection as shown in Figure 5.10b and Table 5.8, shows the effect of the airgap on the pull-in point. From these observations, we can say that a higher sensitivity can be achieved by reducing the

thickness of the diaphragm and the height of the supporting dielectric posts.

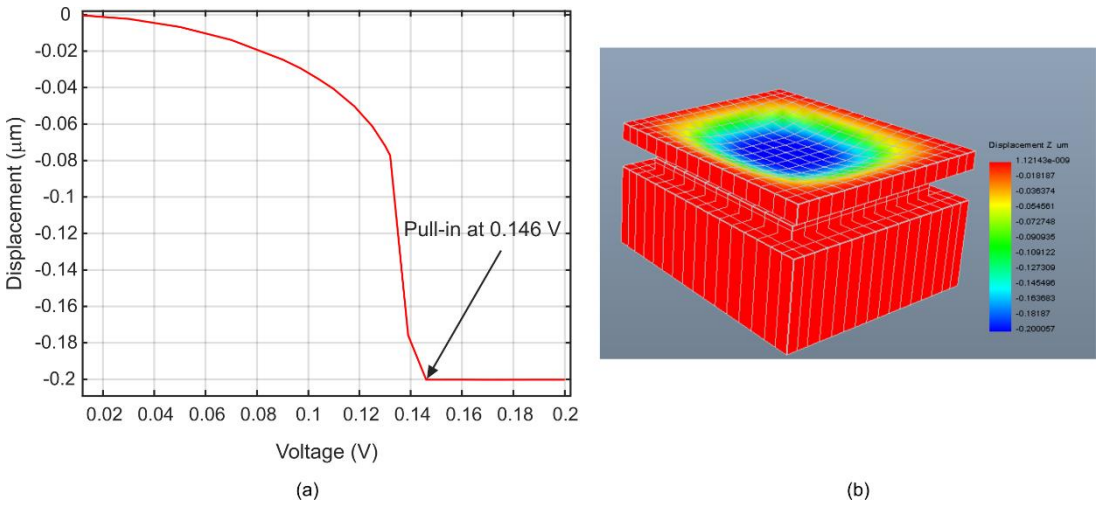

Figure 5.11. a) Pull-in voltage curve of the Pixel capacitor, b) Deflection of the diaphragm at pull-in voltage.

TABLE 5.9 STATE-OF-THE-ART CAPACITANCE SENSING READOUT CIRCUITS.

Reference	Capacitance resolution (aF)
[42]	0.04
[43]	5.40
[44]	95.0
[45]	0.50
[46]	1.0

To satisfy the second design goal, the Pixel variable capacitor is designed in a such way that the capacitance variation generated by the predicted range of magnetic field i.e., $10^{-2}\mathrm{Am}^{-1}$ to $10^{-7}\mathrm{Am}^{-1}$, doesn't alter the flat frequency response of the Pixel. Since, the voltage generated across the damping resistor is applied

across the Pixel capacitor, following (5.8), the damping resistor value is limited by the value of MEMS variable capacitance range. Hence the value of R_d is chosen according to the minimum measurable capacitance. Considering few of the available readout circuits in the literature as listed in Table 5.9, the minimum capacitance change measurable is chosen to be 1 aF in this work.

TABLE 5.10 PIXEL CAPACITOR DESIGN PARAMETERS.

Parameter	Value	Unit
Diaphragm side length $(2a)$	150	µm
Diaphragm thickness (Gold) (d_c)	200	nm
Dielectric spacer thickness , BCB: (g)	200	nm
Insulation layer thickness, BCB (d_i)	50	nm
DC bias voltage (V_{DC})	0.1	V
Sensitivity (S_c)	4.5	aF. µV^{-1}
Pull-in voltage $(V_{pull-in})$	0.146	V
Resonant Frequency (f_{res})	45.75	kHz
Tuning range (C_{max}/C_{min})	1.68:1	-

TABLE 5.11 MATERIAL PROPERTIES.

Property	BCB	Gold	Unit
Young's modulus, E	2.9	79	GPa
Poisson ratio, ν	0.34	0.44	-
Density, ρ_m	1050	19,300	Kg.m^{-3}
Relative permittivity, ε_r	2.65	6.9	-

To attain flat frequency response of the Pixel in the operating UWB range, the Pixel capacitance range is decided to be in the range of (1-2) pF. Following (5.8), the resistance R_d has been selected to be 3Ω. Now, the voltage generated across the resistor totally depends on the induced current. As discussed in the previous section, the Pixel inductor is designed in such a way that it generates the possible high loop current within the given area by reducing the number of turns and using crossed parallel loops. Taking these conclusions and fabrication issues into account, an optimal set of parameters are developed as shown in Table 5.10 and the material properties of the device are shown in Table 5.11.

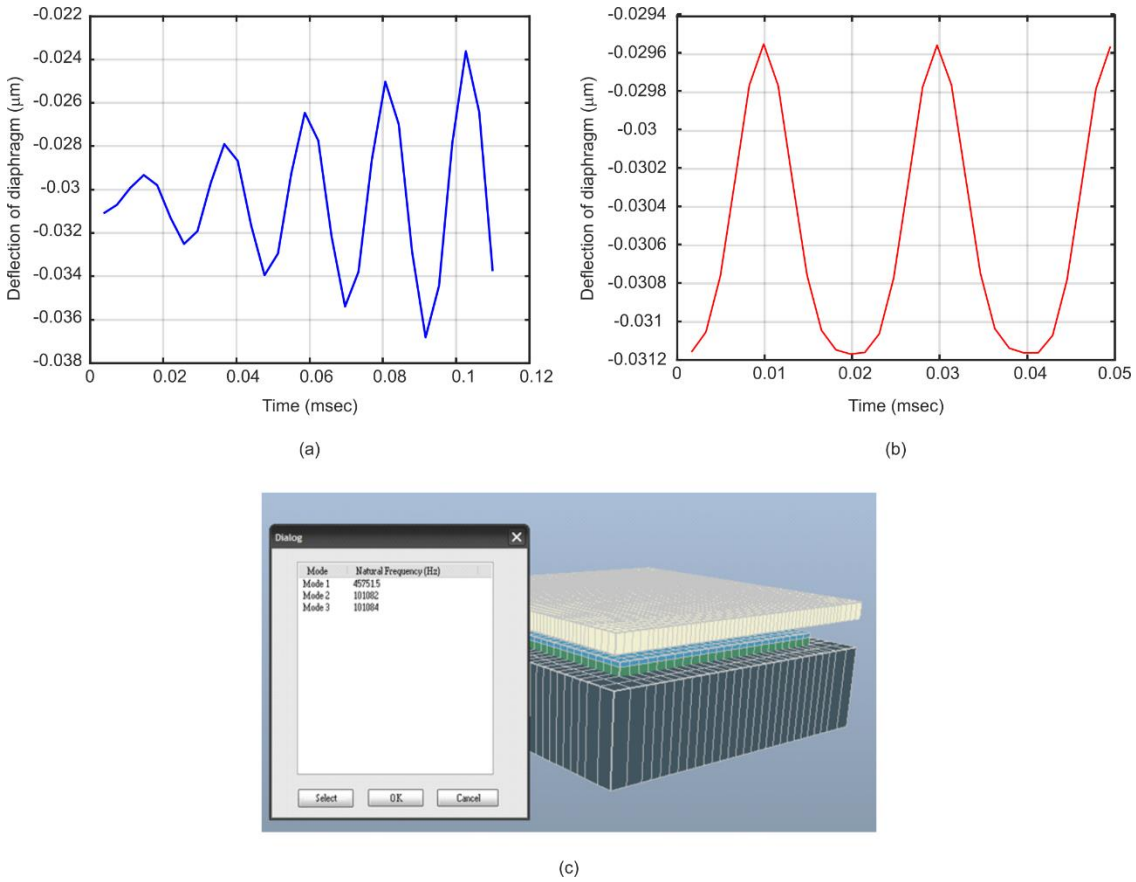

Figure 5.12. a) Diaphragm deflection when 1mV AC voltage at 45.75 KHz (mode1) is applied, b) Diaphragm deflection when 1mV AC voltage at 101.08 KHz (mode 2) is applied, c) IntelliSuite® capture showing Pixel capacitor's three modes of frequency.

The pull-in voltage curve of Pixel capacitor is shown in Figure 5.11a. From Figure 5.11, the pull in observed at 0.146 V and the DC bias is chosen to be 0.1 V. Since the AC operating voltages here are quite low, for better coupling of induced AC voltage to the diaphragm deflection, a lower DC bias voltage is beneficial so that it can be more comparable with the applied AC voltage according to (3.12).

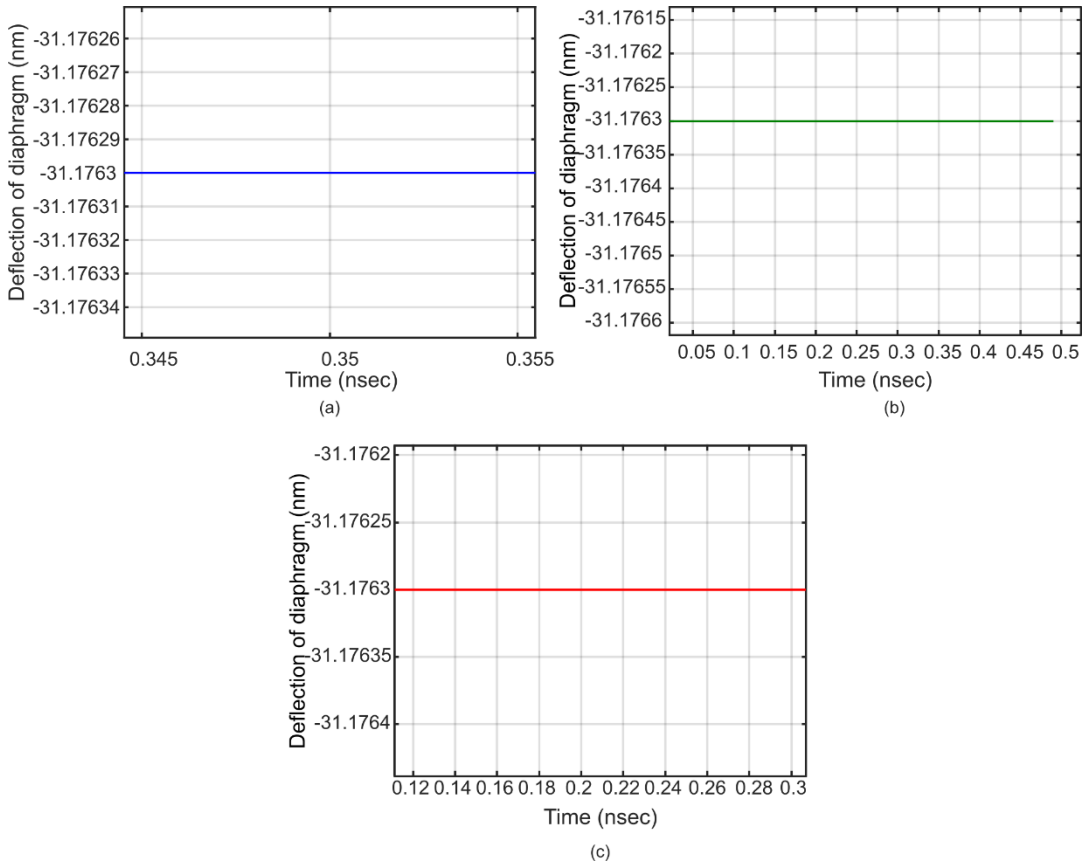

Figure 5.13. The deflection of the diaphragm when applied AC voltage (1 mV amplitude) is at, a) 3.1 GHz, b) 4.1 GHz, c) 5.1 GHz.

The mechanical resonance of the designed Pixel diaphragm is at 45.75 kHz as shown in Figure 5.12, which is far away from the operating frequency range with center frequency at 4.1 GHz, hence, the signal in (3.1 GHz - 4.1 GHz) range doesn't modulate the capacitance, only the RMS value of the signal had its

influence as shown in Figure 5.12 and Figure 5.13. Figure 5.13 shows that the Pixel capacitor is independent of the frequency but depends only on the RMS value of the AC voltage applied because the amount of deflection is constant and the oscillation of the diaphragm with respect to frequency is not observed at high frequency (Figure 5.13) unlike at the frequency near mechanical resonance (Figure 5.12).

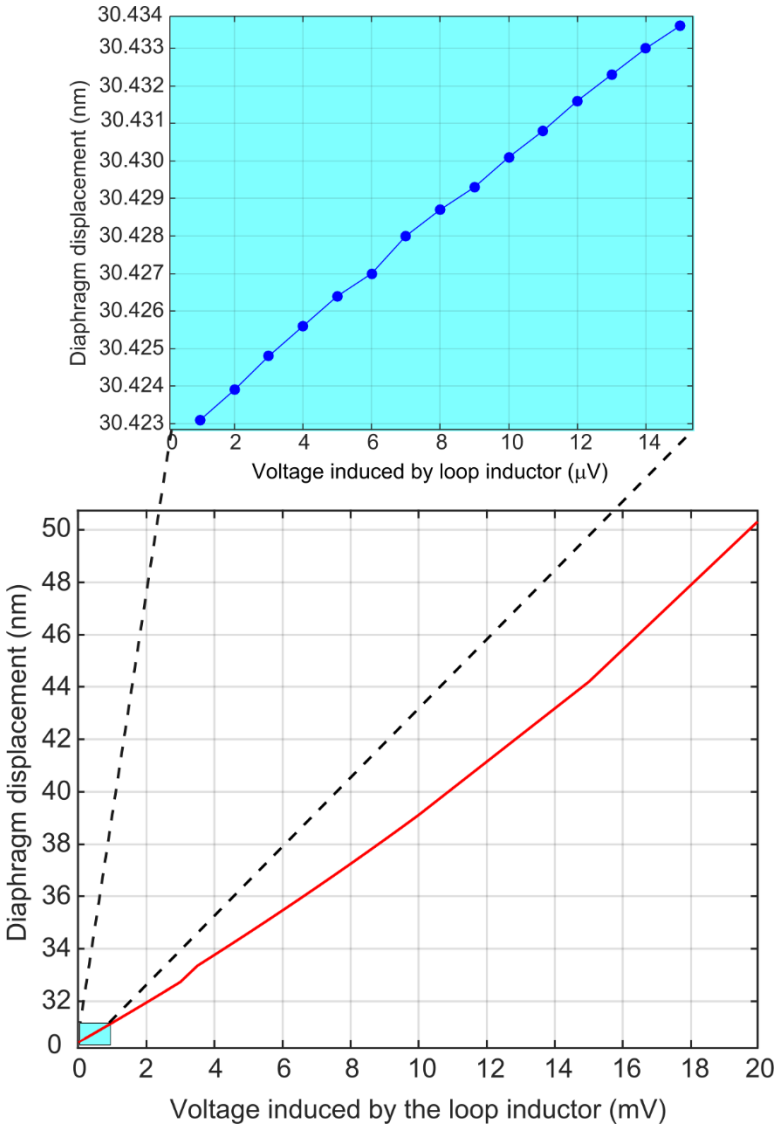

Figure 5.14. Diaphragm deflection with inductor induced AC voltage.

A device level Finite Element Method (FEM) simulation of proposed microwave Pixel capacitor is carried out in IntelliSuite® software. The deformation of the Pixel capacitor diaphragm for applied voltage was simulated using FEM simulator and is as shown in figure 5.14. From Figure 5.14, a linear operation of

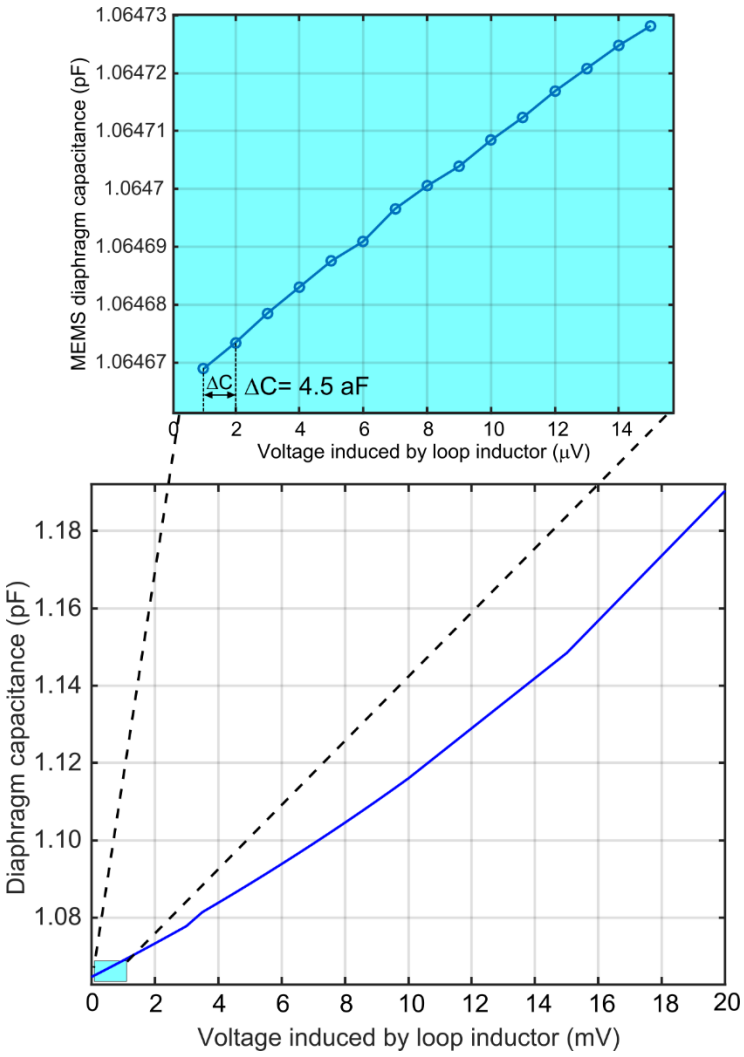

Figure 5.15. Capacitance generated with loop inductor induced voltage.

the device has been observed and a deflection variation of 0.8 pm is observed for 1 μV change in the loop inductor induced voltage, achieving a mechanical deflection sensitivity of 0.8 pm.μV^{-1}. The corresponding capacitance generated

across the Pixel capacitor is as shown in Figure 5.11. From Figure 5.11, a capacitance change of 4.5 aF is observed for one microvolt change in applied AC voltage.

The estimated magnetic field intensity levels of tissue interface reflections as shown in Table 5.1,5.2,5.3 are used to determine the voltage induced across the Pixel inductor, are shown in Figure 5.16. The corresponding capacitance generated across the Pixel capacitor is as shown in Table 5.12.

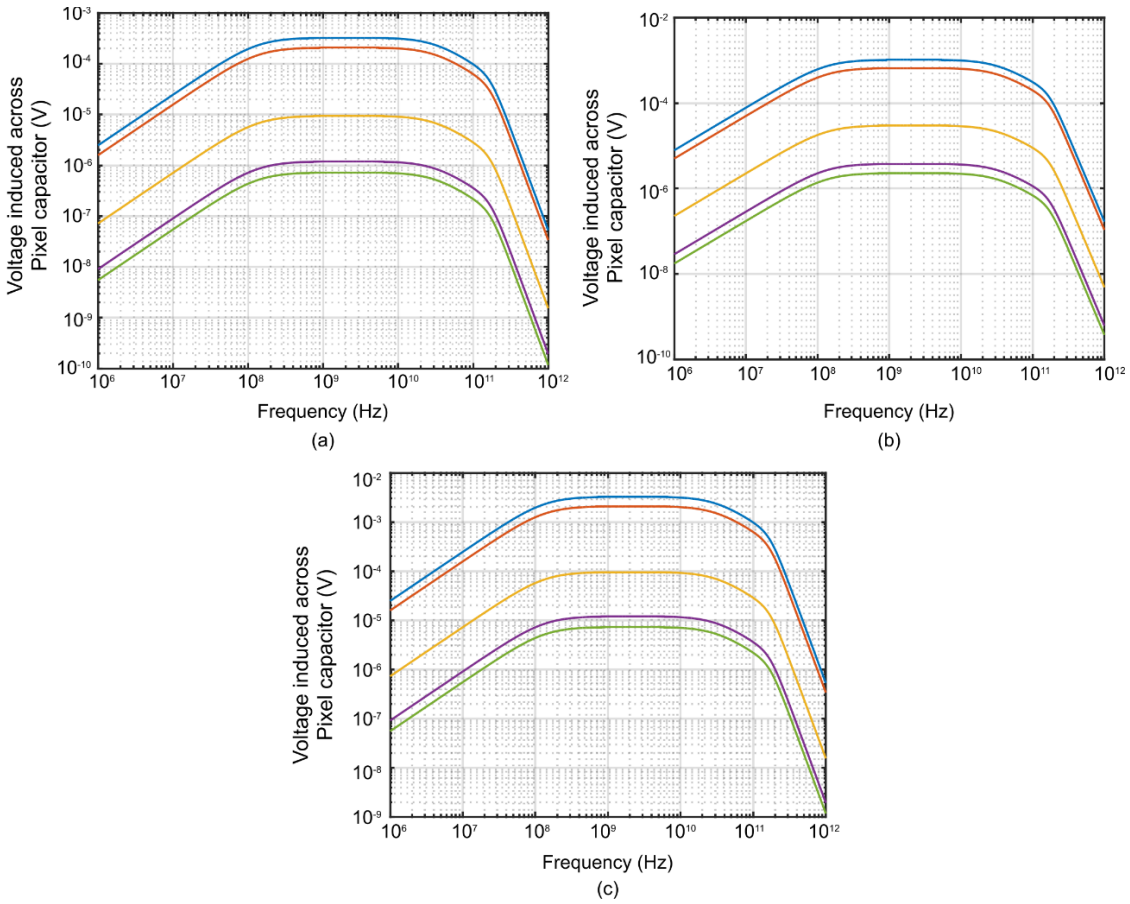

Figure 5.16. The voltage induced across the Pixel capacitor corresponding to the reflections from skin/fat, fat/muscle, muscle/cartilage, cartilage/lung and lung/heart when the transmit power is, a) 5 mW, b) 50 mW, c) 500 mW.

TABLE 5.12 PIXEL VOLTAGE AND CAPACITANCE CORRESPONDING TO THE TISSUE INTERFACE REFLECTIONS AT 5 mW,50 mW AND 500 mW.

Origin of reflection	Voltage generated across Pixel inductor and capacitor (μV)			Pixel capacitance generated (pF)		
	5 mW	50 mW	500 mW	5 mW	50 mW	500 mW
Skin/Fat	325	1030	3245	1.066038	1.069062	1.080212
Fat/Muscle	207	656	2075	1.065539	1.067449	1.073654
Muscle/Cartilage	9.397	29.46	95.26	1.064703	1.064786	1.065065
Cartilage/Lung	1.190	3.738	11.96	1.064669	1.064683	1.064716
Lung/Heart	0.722	2.26	7.262	1.064669	1.064673	1.064696

CHAPTER 6

FABRICATION OF PROPOSED MICROWAVE PIXEL

This chapter presents a step by step description of the process sequence to be followed to fabricate the proposed microwave Pixel array on glass wafer. The details of each fabrication step are provided with operating conditions, used materials, process type and a conceptual cross-sectional view has been provided

6.1. Fabrication steps

STEP 1: Wafer Cleaning

The fabrication process starts with the cleaning of a glass wafer FOTURAN® II from Schott North America. FOTURAN® II has been selected as the starting substrate due to its excellent stability of the dielectric constant at the operating UWB frequency range. Before the glass wafer is subjected to any microfabrication process, a cleaning process is necessary to clean oils and organic residues that may build up on the wafer surface. Cleaning of glass wafers involves a solvent clean, followed by a de-ionized water (DI) rinse, followed by a mild acid clean, DI rinse and blow dry [47]. The solvents used for the solvent cleaning are acetone and methanol, while hydrochloric acid (HCL) is used for mild acid clean stage [47]. The cleaned glass wafer cross section is shown in Figure 6.1.

Figure 6.1. Glass wafer after cleaning.

STEP 2: Deposition of metal

The second step includes deposition of the Gold (Au) layer, which is the bottom electrode of the Pixel capacitor, as shown in Figure 6.2. Since, gold doesn't adhere well to glass, a 3.5 nm seed layer of titanium is deposited using DC magnetron at 250 W and 5 mtorr with an approximate deposition rate of 0.1 nm/sec [48]. Following this step, a 100 nm thick AU layer was deposited by DC magnetron sputtering, with DC target at 150W, pressure at 5 mtorr. The deposition time is of 200 secs according to the accepted deposition rate of 0.5 nm/sec [48].

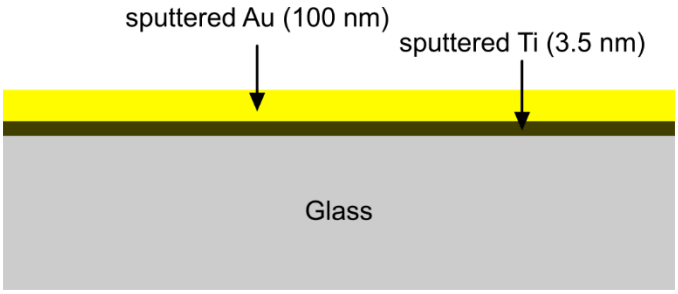

Figure 6.2. Metal deposition.

STEP 3: Photolithography to realize the bottom electrode of the capacitor

After deposition of the electrode layer, a Shipley 1805 photoresist has been spin deposited using a thin HMDS layer as the primer. After soft baking of the photoresist layer, the wafer was exposed to 450 nm wavelength UV light to carry out the photolithography (using contact mask aligner) and then the gold layer is patterned using ion beam etching, as shown in Figure 6.3, with a typical etch rate for gold is 0.12 µm/min at beam energy of 500 eV. Next to this, the photoresist was etched.

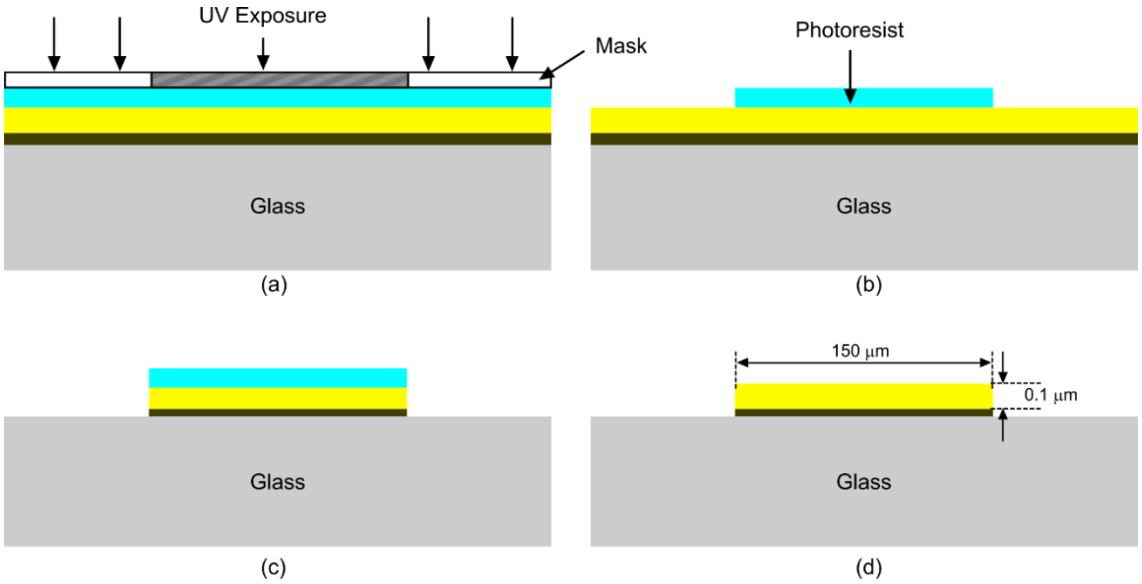

Figure 6.3. a) Spin on photoresist & exposure to UV with contact mask aligner, b) Photoresist develop, c) Ion beam etch of gold and titanium layers, d) Strip photoresist.

STEP 4: Deposition of BCB as an insulation layer and dielectric post

BCB is chosen as an insulating material and as a dielectric post. A thin BCB layer (Cyclotene™ 3022-35) of 3500 Å was spin deposited on the gold with 3.5 nm sputtered chromium as a seed layer to realize insulation layer on top of the bottom electrode to avoid breakdown and dielectric posts to realize the air gap between the capacitor electrodes as shown in Figure 6.4a.

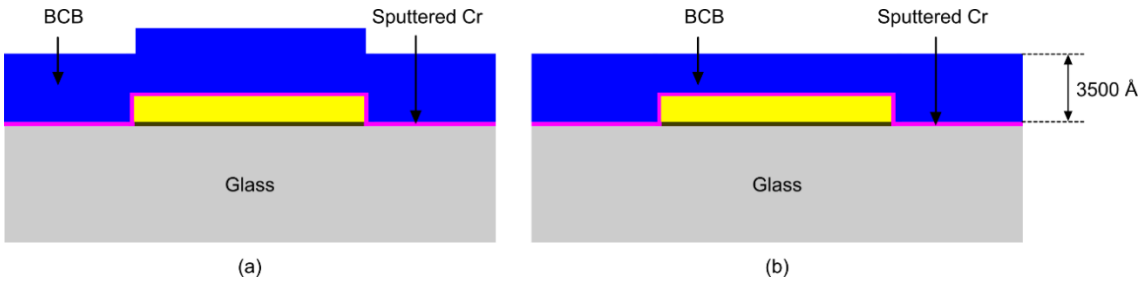

Figure 6.4. Cross-sectional view, a) Spin deposited BCB, b) after Planarization.

This step is followed by a Chemical mechanical planarization (CMP) of BCB for planarizing the surface as shown in Figure 6.4b

STEP 5: Photolithography to realize dielectric posts

To pattern BCB, a photoresist is spun and soft baked. A contact mask aligner is used to transfer the desired pattern onto the photoresist and 450 nm wavelength UV light is exposed and then the exposed Photoresist is washed away leaving a patterned photoresist as shown in Figure 6.5. This is followed by a Reactive Ion Etch (RIE) of BCB and then photoresist is stripped.

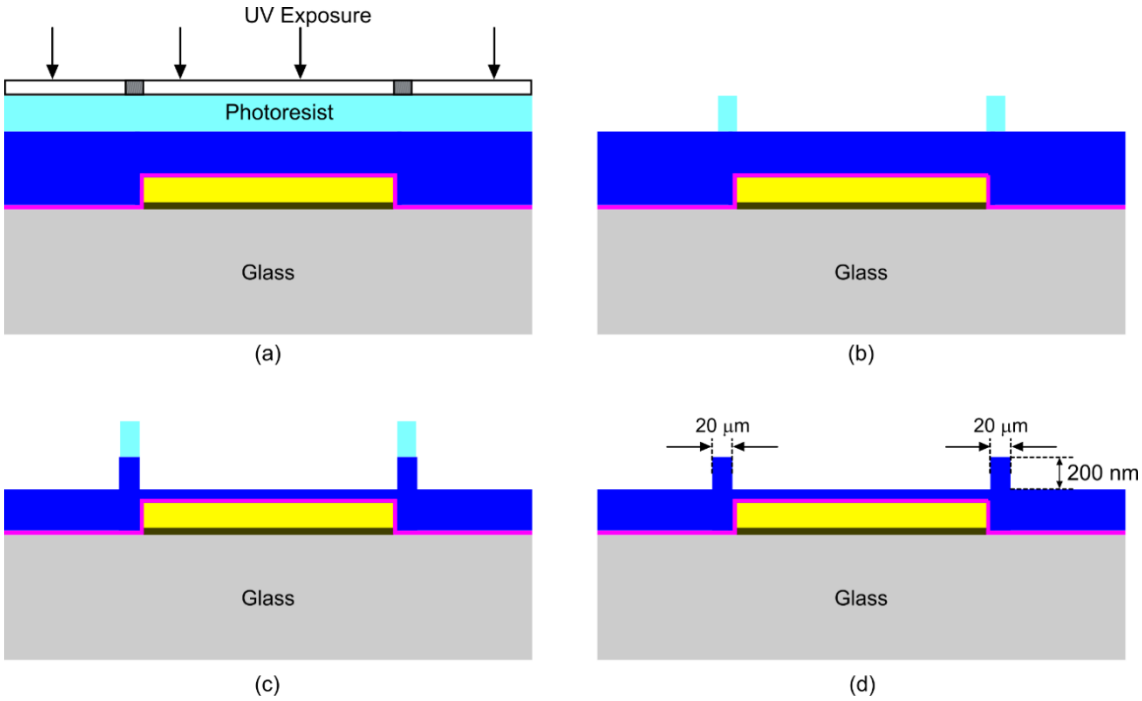

Figure 6.5. a) Photoresist exposure to UV, b) Photoresist develop, c) RIE etch of BCB, d) Removal of photoresist.

STEP 6: Deposition and pattern of sacrificial layer

A 200 nm thick SiO_2, has been deposited as a sacrificial layer by plasma-

enhanced chemical vapor deposition (PECVD) using Tetraethoxysilane (TEOS) and O_2 at 270°C and then photolithography using proximity mask aligner is done followed by patterning the oxide layer using RIE process with etch rate of 123 nm/min at 100 W [49]. The cross-sectional views of these steps are shown in Figure 6.6.

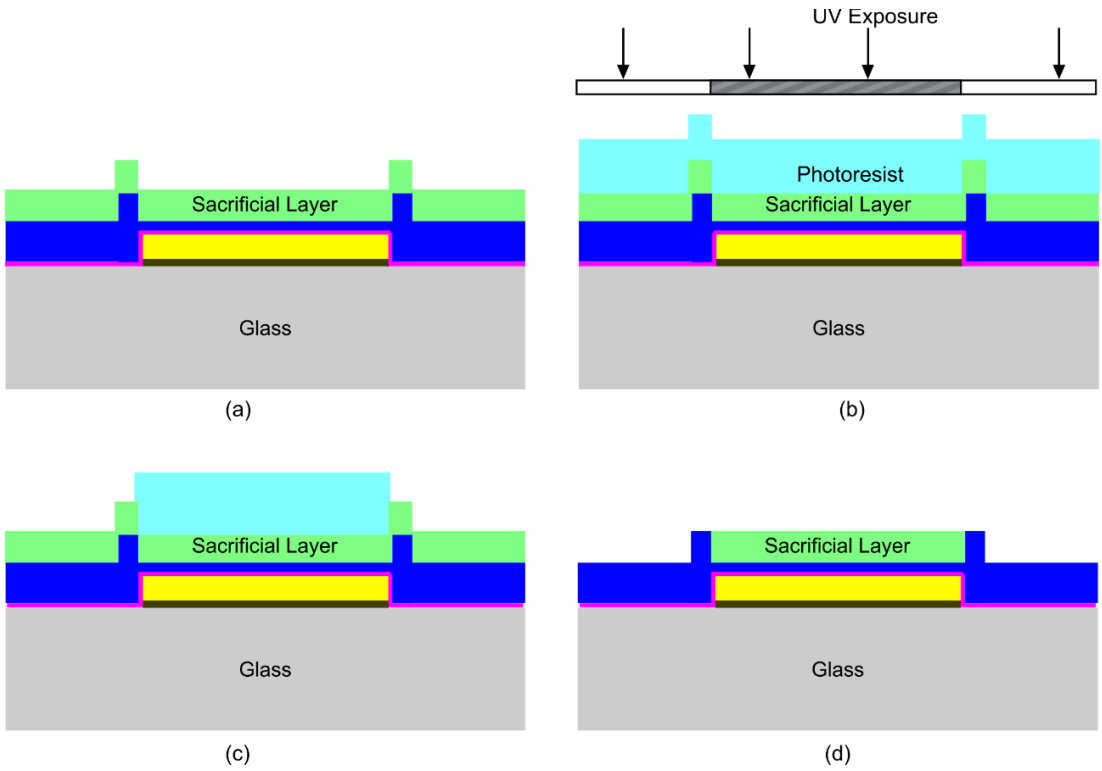

Figure 6.6. a) Deposition of SiO_2, b) Photoresist and UV exposure, c) Pattern photoresist, d) RIE etch of sacrificial layer.

STEP 7: Depositing and patterning gold layer for diaphragm

This step includes deposition of gold (Au) layer, which is the top electrode of the Pixel capacitor. Since gold cannot be deposited on SiO_2 and BCB, a 20 nm layer of Chromium is deposited as an adhesion layer. After that, 400 nm thick gold layer is deposited using electron-beam evaporation technique (Figure 6.6). The Chromium seed layer was deposited at 20% power to obtain a deposition rate of

3.0 Å/sec and Gold conductive layer was deposited at 30% power which gives a rate of 9.2 Å /sec. In order to avoid oxidation of Chromium, two deposition processes were done in one duty cycle. Then patterning the device with photoresist, gold and chromium layers are etched. Gold layer was etched using Transene™ TFA solution (8% I, 21% KI, 71% H_2O, etch rate 28 Å /sec). Then Chromium layer is etched using, Transene™1020 (10-20% Ceric ammonium Nitrate, 5-6% HNO_3, etch rate 40 Å /sec) as shown in Figure 6.7. Finally, the etch holes are created for sacrificial etch of SiO_2.

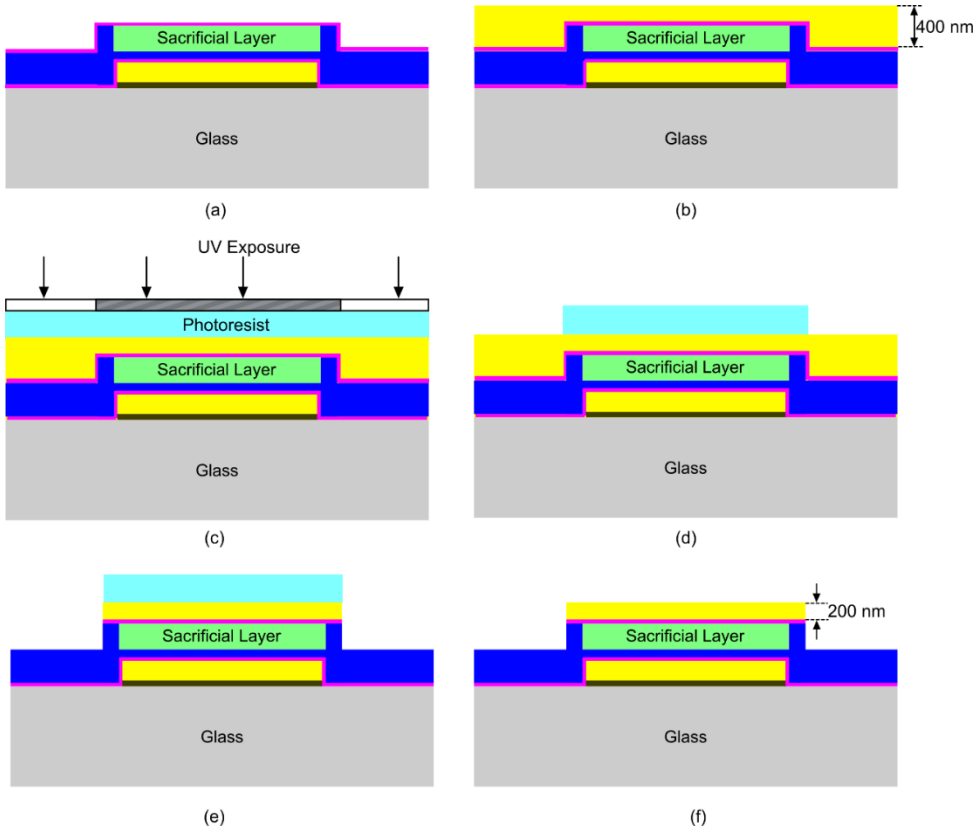

Figure 6.7. a) Deposition of 20 nm chromium, b) E-beam evaporation of gold, c) Photoresist spin and UV exposure, d) Photoresist develop, e) Etching of gold and chromium, f) Removal of photoresist.

STEP 8: Removal of sacrificial layer

In order to release the diaphragm, Transene™ Improved buffered oxide etch (BOE) solution (4-8% HF + NH_4F, etch rate of nearly 700Å/min) has been used to sacrificially etch the oxide layer for 171 seconds, which is followed by critical point drying (CPD) in a typical CPD dryer (Figure 6.8). Critical point drying is carried out to avoid stiction of the devices.

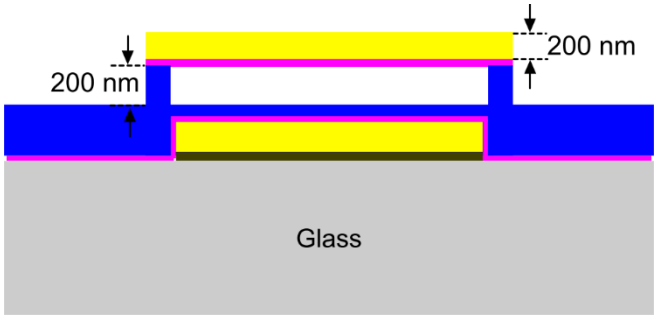

Figure 6.8. Release of diaphragm.

STEP 9: Silicon wafer with BCB spin coating at the bottom

Here starts the first process step to realize the Pixel inductor (a 12×12 array of sub-Pixel inductors). This begins with RCA (Radio Corporation of America) cleaning of silicon wafer for any organic coatings in a strong oxidant piranha solution i.e., a 7:3 mixture of concentrated sulphuric acid (H_2SO_4) and hydrogen peroxide (H_2O_2). Then organic residues are removed in a 5:1:1 mixture of water (H_2O), hydrogen peroxide (H_2O_2), and ammonium hydroxide (NH_4OH). As this step can grow a thin oxide on silicon, it is necessary to insert a dilute HF etch to remove this oxide when cleaning a bare silicon wafer and then ionic clean using a solution of 6:1:1 H_2O: H_2O_2: HCl. Then BCB layer of 2 µm is spin deposited at the bottom

of the wafer and then etched BCB using Reactive Ion Etch (RIE) technique as shown in Figure 6.9.

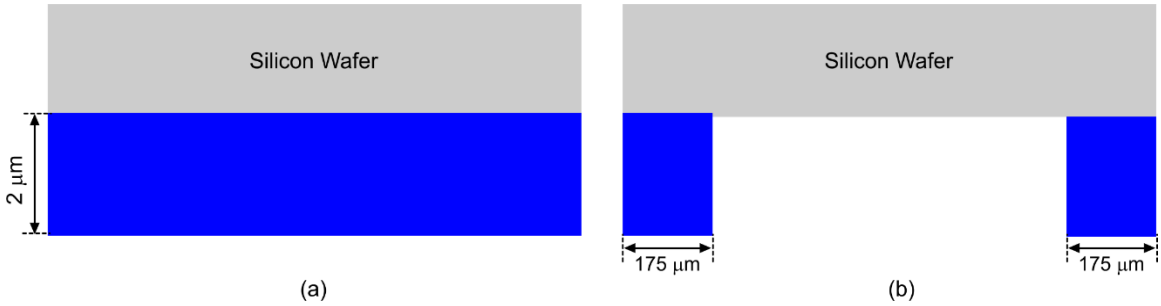

Figure 6.9. Silicon wafer spin deposited with BCB at the bottom, b) RIE etch of BCB layer.

STEP 10: Deposition and patterning of Sacrificial layer

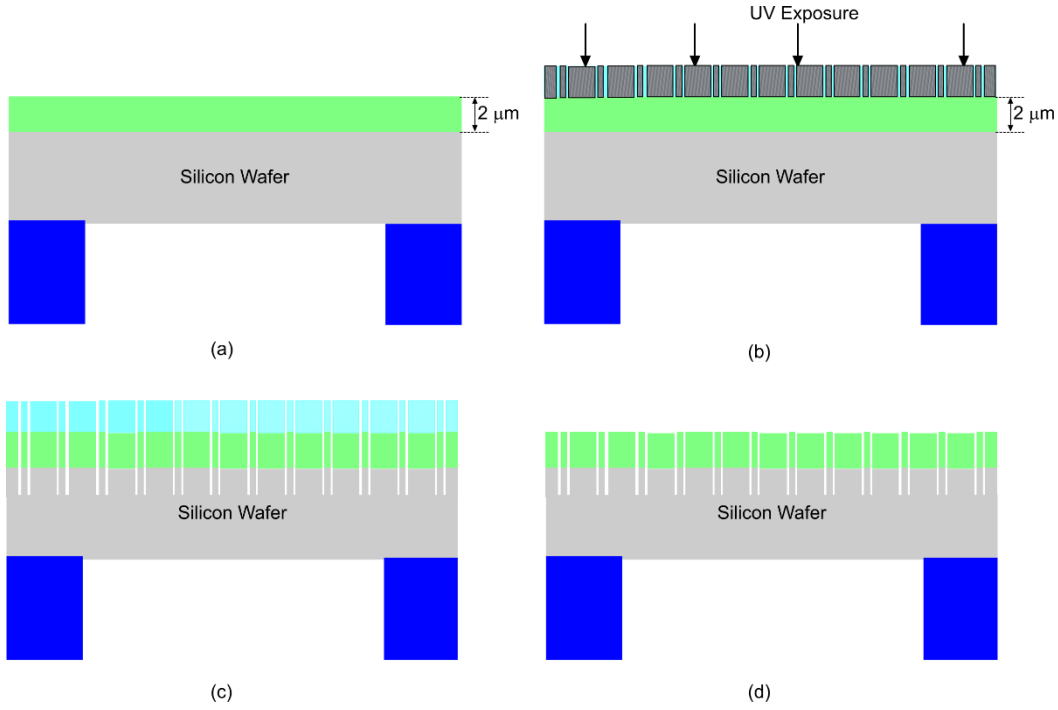

Figure 6.10. a) Deposition of SiO_2, b) Spin photoresist and UV exposure, c) Pattern photoresist, d) Removal of photoresist.

SiO_2 sacrificial layer has been deposited using plasma-enhanced chemical vapor deposition (PECVD) and then photolithography is done followed by

patterning the oxide layer using RIE process with etch rate of 123 nm/min at 100 W [49]. The silicon layer is then DRIE (Deep reactive ion etch) etched as shown in Figure 6.10.

STEP 11: Deposition and patterning of conducting layer

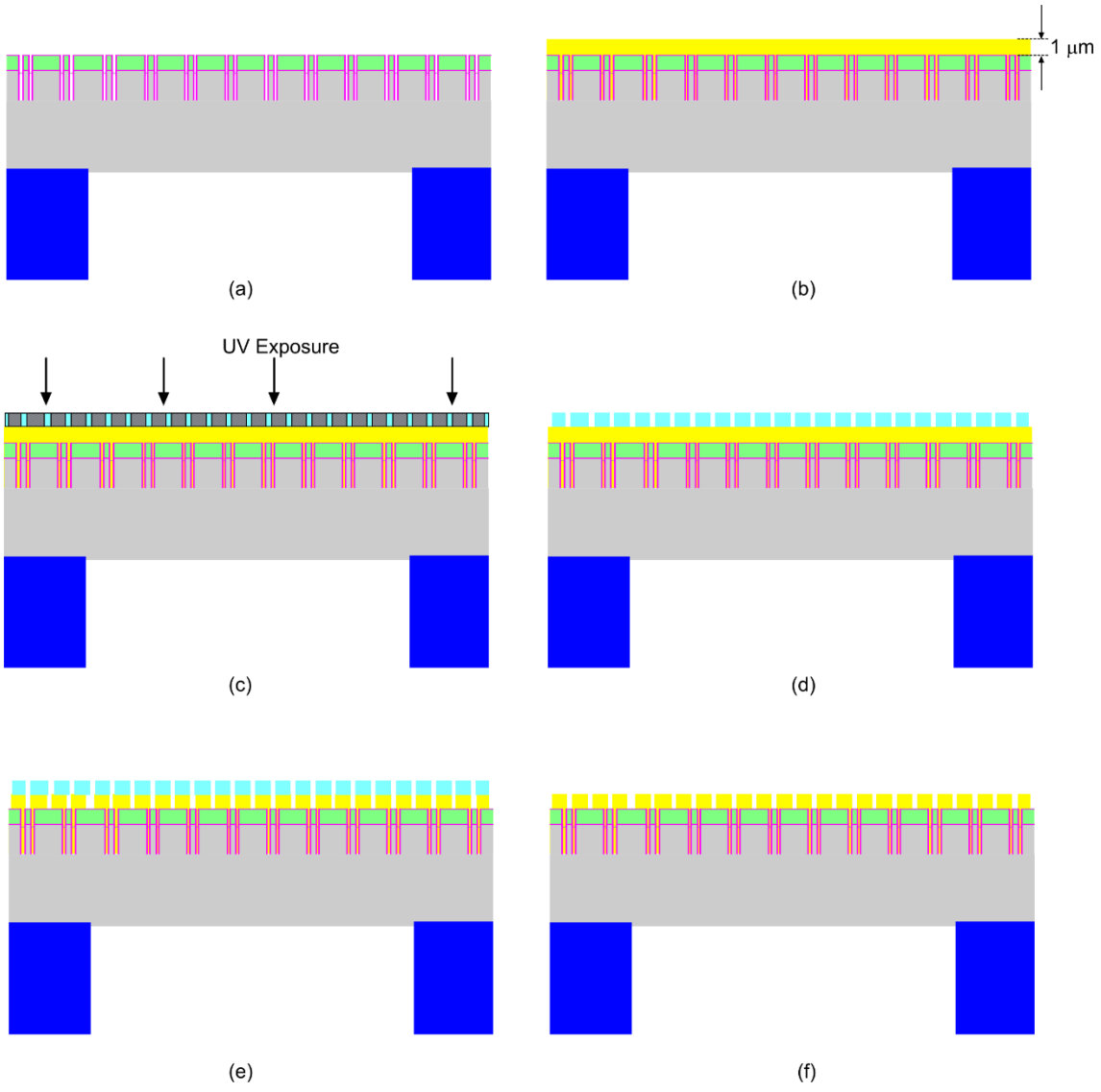

Figure 6.11. a) Deposition of chromium as seed layer, b) E-beam evaporation of gold, c) Spin photoresist and UV exposure, d) Pattern photoresist, e) patterning of gold, f) Strip photoresist.

This step includes deposition of gold (Au) layer to realize inductors. Since

gold cannot be deposited on SiO_2, a 5 nm layer of Chromium is deposited as an adhesion layer. After that, 1 µm thick gold layer is deposited using electron-beam evaporation technique as shown in Figure 6.11. The Chromium seed layer was deposited at 20% power to obtain a deposition rate of 3.0 Å/sec and Gold conductive layer was deposited at 30% power which gives a rate of 9.2 Å /sec. This step is followed by patterning the device with photoresist and then etching of gold layer using Transene™ TFA solution (8% I, 21% KI, 71% H_2O, etch rate 28 Å /sec).

STEP 12: Removal of sacrificial layer

In this step, sacrificial layer SiO_2 is etched away to release the inductors. Transene™ Improved buffered oxide etch (BOE) solution (4-8% HF + NH4F, etch rate of nearly 700Å/min) has been used to sacrificially etch the oxide layer, which is followed by critical point drying (CPD) in a typical CPD dryer (Figure 6.8).

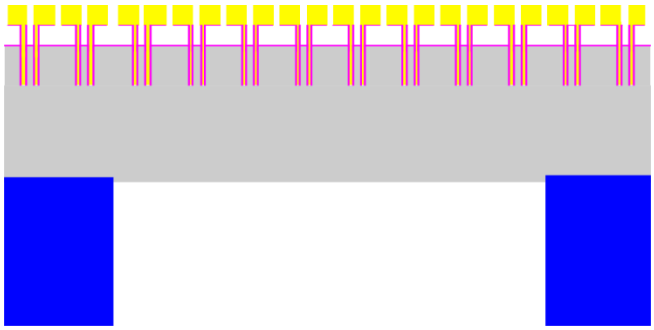

Figure 6.12. Release of 12×12 Pixel inductor array.

STEP 13: Deposition of magnetic material

This step involves realization of magnetic core for Pixel inductors. Due to high frequency characteristics and high permeability of 1000, Fe-Co-B is chosen

to be a magnetic material [41]. Fe-Co-B film of 3 μm thick is deposited by RF magnetron sputtering in Ar plasma at pressure of 8 mTorr and power of 450 W.

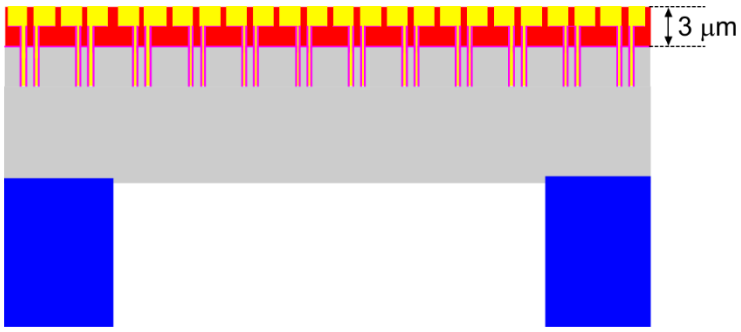

Figure 6.13. Deposition of Fe-Co-B film.

STEP 14: Etching of magnetic material

In this step, to realize each inductor wounded around the magnetic core, a dry etching of Fe-Co-B was carried out in inductively coupled plasmas of Cl_2/Ar mixture with an excitation frequency of 13.56 MHz and RF power up to 700 W. After the etching, the samples were rinsed with de-ionized (DI) water to remove the chlorine residues [50]. The cross-sectional view of the device after magnetic core etch is as shown in Figure 6.14.

STEP 15: Adhesive bonding of BCB -BCB to realize complete Pixel

The bonding surfaces of BCB Cyclotene™ of Pixel capacitor and Pixel inductor, as shown in Figure 6.15, were cleaned and agitated by putting them under 40 sccm flow of O_2 plasma and 10 sccm flow of CF_4 at chamber pressure of 100 mTorr and 90 W RF power for 30 secs [51]. Following this, both the wafers are placed in vaccum chamber with pressure of about 70 mtorr, to apply pre-bonding pressure on the wafers to be bonded and then final annealing is done at

temperature of 210°C [51].

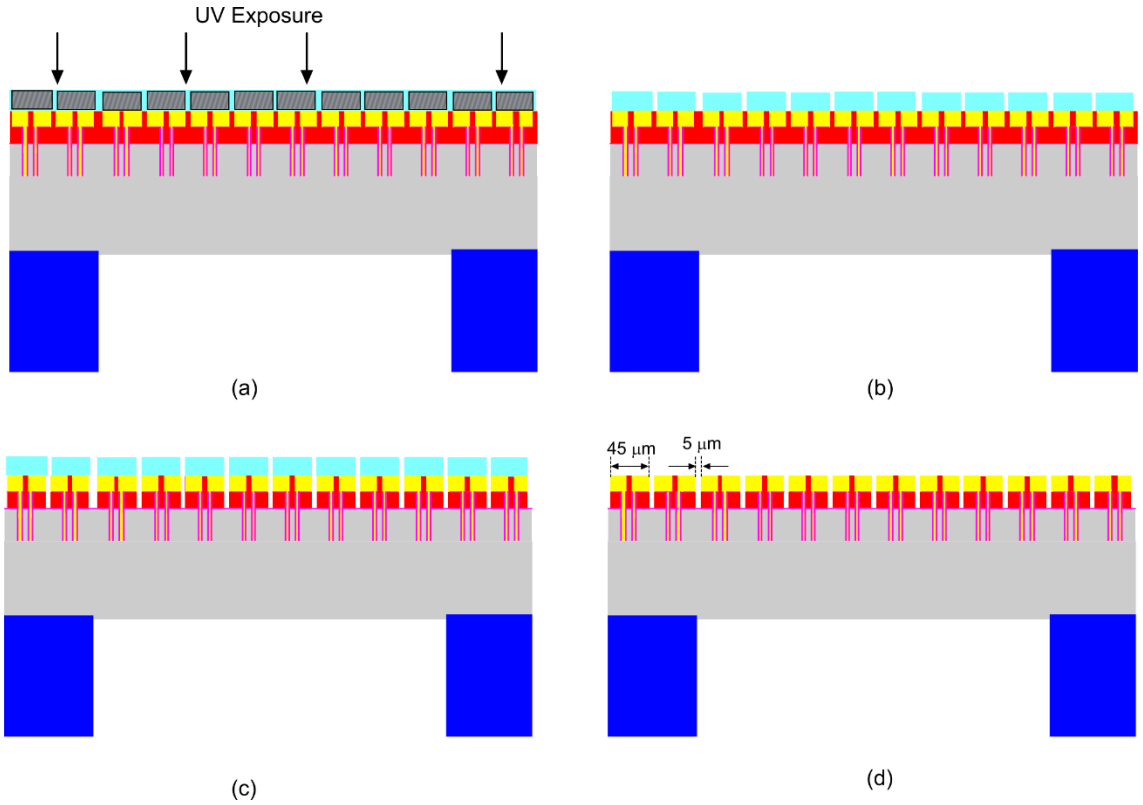

6.14. a) Spin photoresist and UV exposure with contact mask aligner, b) Develop photoresist, c) Etch magnetic core, d) Strip photoresist.

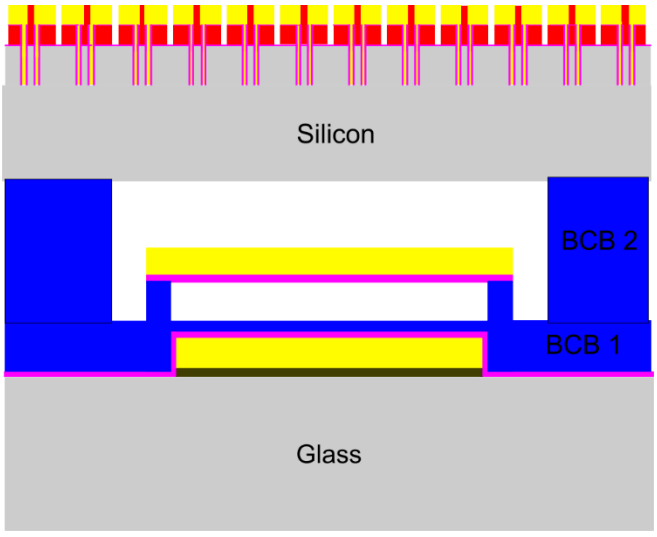

Figure 6.15. BCB- BCB adhesive bonding.

CHAPTER 7

CONCLUSIONS AND FUTURE WORK

7.1. Discussions and Conclusions

A Novel MEMS based microwave Pixel for use with an UWB radar for diagnostic medical imaging has been presented. The developed Pixel has been designed with 12×12 array of loop inductors connected in parallel to act as a single cross-parallel loop and a MEMS variable diaphragm capacitor. A 2-D array of such Pixels can generate a 2D voltage map corresponding to the dielectric properties distribution in a respective tissue layer inside the human thorax deep upto 4.2 cm. As the diseased and healthy tissues differ in their dielectric properties and conductivity, the generated dielectric constant based voltage map will be able to clearly identify any medical condition such as pneumothorax or breast cancer. The simulation of loop inductor array and MEMS variable capacitor are carried out separately, as the circuit level operation of loop inductor connected in parallel to MEMS variable capacitor is done using MATLAB®, OrCAD® PSpice® and then the output voltage generated through this simulation is fed to the MEMS Pixel capacitor simulated in IntelliSuite®. Thus, the overall simulation of the Pixel shows the capacitance generated across the Pixel capacitor due to the magnetic field picked up by the loop inductor.

The designed Pixel is capable of detecting the magnetic field intensity equal to or greater than 0.8 μAm^{-1} , generating a voltage equal to or greater than 1 µV, which generates a Pixel capacitance of 1.064668 pF. A Pixel capacitance change of nearly 4.5 aF is observed for every 1 µV change in Pixel inductor induced voltage, thus the sensitivity of proposed Pixel is 4.5 aF/0.8 μAm^{-1}. According to the mathematical model, the estimated magnetic intensity of each tissue interface reflection at transmit power of 5 mW, 50 mW and 500 mw are in the Pixel detectable range except for the lung/heart reflection in 5 mW case. But the diagnostic imaging to detect the phenumothorax condition can be done for all the three estimated power levels as shown in Table 7.1.

TABLE 7.1 PIXEL DETECTABILITY ANALYSIS FOR TRANSMIT POWER OF 5mW, 50mW, 500mW.

Depth	P_t=5 mW	P_t= 50 mW	P_t= 500 mW
	Pixel detection	Pixel detection	Pixel detection
Skin/Fat	YES	YES	YES
Fat/Muscle	YES	YES	YES
Muscle/Cartilage	YES	YES	YES
Cartilage/Lung (pneumothorax)	**YES**	**YES**	**YES**
Lung/Heart	NO	YES	YES

The proposed Pixel with a consideration of 1 aF as a minimum measurable capacitance change, can detect the reflections deep upto Lung/heart interface which is about 4.2 cm away from the skin surface for a typical adult (male)

according to [35]. The proposed design may be used for cardiac imaging in the case of newborn babies, since 4.2 cm deep into thorax of a baby can pass through the heart. The miniature size of the system due to MEMS technology, enable this device to use for capsule endoscopy to image internal body organs.

7.2. Future work

In the present thesis work, a MEMS based microwave Pixel is designed for diagnostic medical imaging. The research work can be extended further by:

1. 3D Simulation of complete Pixel array to study the effect of Pixel spacing and its effect on the image resolution.
2. Investigating the noise analysis of the Pixel system, to increase signal-to-noise (SNR) ratio in order to distinguish the reflected signal from the noise floor.
3. Analysis on mutual coupling of adjacent sub-Pixel loops and techniques to reduce this mutual effect.
4. Fabrication and experimental characterization of the proposed Pixel array for diagnostic imaging.
5. Study on a MEMS based microwave focusing lens to order to enable sub-wavelength resolution of the system ruling out the diffraction limit of the conventional systems.
6. Near field operation of the Pixel array.

Detection of Diaphragm Deflection using laser doppler techniques:

Successful realization of this Pixel array for imaging much more deeper tissues leads to a promising solution for the existing short coming of the available imaging techniques. However, this demands an extremely sensitive circuitry capable of detecting a minute change in capacitance less than Zeptofarad, to generate a detectable voltage output map. The possible solution to overcome this, could be a technique that can detect the diaphragm deflection down to sub picometer using laser doppler techniques. In this technique as shown in Figure 7.1, the diaphragm to be observed is illuminated with a laser light and the reflections from the diaphragm are processed to measure the deflection of the membrane based on the phase shift of the reflections. This technique may provide higher sensitivity to capture weak microwave signals when compared to capacitive sensing methods.

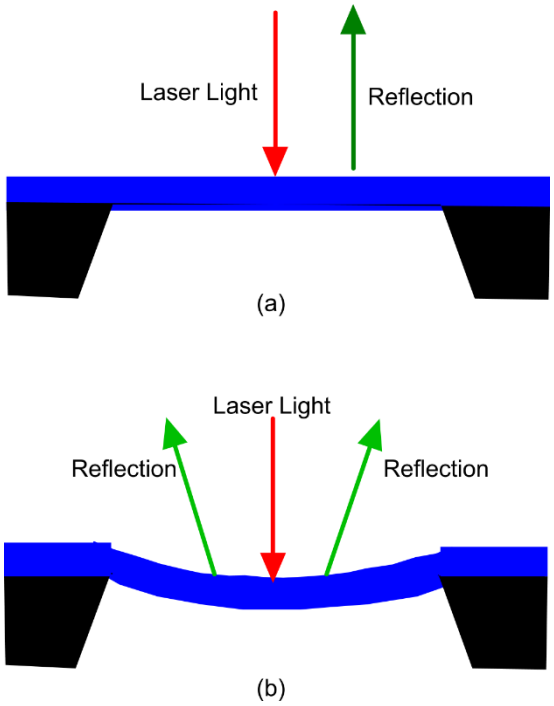

Figure 7.1. Laser light reflection from a) a non-deflected diaphragm b) a deflected diaphragm.

Laser assisted Microwave Radar Tomography: The developed microwave Pixel array has the potential for use in a manner similar to the photoacoustic tomography. A laser beam can be used to heat up the tissue and an UWB radar with the 2D pixel array can be used to generate a 3-D map of the heat deformed tissue layer. This may help to identify the developmental stages of a particular disease or the healing process.

Appendix A MATLAB® code for UWB signal attenuation in human tissues

```
clc;
clear all;
format long g;
%Complex permittivity of air%
relskin=zeros(size(3.1*10^9:0.1*10^9:4.1*10^9));
relfat=zeros(size(3.1*10^9:0.1*10^9:4.1*10^9));
relmuscle=zeros(size(3.1*10^9:0.1*10^9:4.1*10^9));
relcartilage=zeros(size(3.1*10^9:0.1*10^9:4.1*10^9));
rellung=zeros(size(3.1*10^9:0.1*10^9:4.1*10^9));
relheart=zeros(size(3.1*10^9:0.1*10^9:4.1*10^9));
i=1
%complex permittivity of skin%
% parameters from [http://niremf.ifac.cnr.it/docs/DIELECTRIC/AppendixC.html]
for f=4.1e9

w=2*pi*f;
e=4;
del(1)=32;
tau(1)=7.234*10^-12;
alf(1)=0;
del(2)=1100;
tau(2)=32.481*10^-9;
alf(2)=0.2;
sig=0;
del(3)=0;
tau(3)=159.155*10^-6;
alf(3)=0.2;
del(4)=0;
tau(4)=15.915*10^-3;
alf(4)=0.2;
y=0;
for n=1:4;
a=1i*w*tau(n);
x(n)=(del(n)/(1+a^(1-alf(n))));
y=y+x(n);
end;
eps=8.854*10^-12;
relskin(i)=e+y+(sig/(1i*w*eps))
%relative permittivity of fat%
e=2.5;
del(1)=3;
tau(1)=7.958*10^-12;
alf(1)=0.20;
del(2)=15;
tau(2)=15.915*10^-9;
alf(2)=0.1;
sig=0.01;
del(3)=3.3*10^4;
tau(3)=159.155*10^-6;
```

```
alf(3)=0.050;
del(4)=1*10^7;
tau(4)=7.958*10^-3;
alf(4)=0.010;
y=0;
for n=1:4;
a=1i*w*tau(n);
x(n)=(del(n)/(1+a^(1-alf(n))));
y=y+x(n);
end;
eps=8.854*10^-12;
relfat(i)=e+y+(sig/(1i*w*eps));
%relative permittivity of muscle%
e=4;
del(1)=50;
tau(1)=7.234*10^-12;
alf(1)=0.1;
del(2)=7000;
tau(2)=353.678*10^-9;
alf(2)=0.1;
sig=0.2;
del(3)=1.2*10^6;
tau(3)=318.310*10^-6;
alf(3)=0.1;
del(4)=2.5*10^7;
tau(4)=2.274*10^-3;
alf(4)=0;
y=0;
for n=1:4;
a=1i*w*tau(n);
x(n)=(del(n)/(1+a^(1-alf(n))));
y=y+x(n);
end;
eps=8.854*10^-12;
relmuscle(i)=e+y+(sig/(1i*w*eps));
%relative permittivity of cartilage%
e=4;
del(1)=38;
tau(1)=13.263*10^-12;
alf(1)=0.150;
del(2)=2500;
tau(2)=144.686*10^-9;
alf(2)=0.150;
sig=0.150;
del(3)=1*10^5;
tau(3)=318.310*10^-6;
alf(3)=0.1;
del(4)=4*10^7;
tau(4)=15.915*10^-3;
alf(4)=0;
y=0;
for n=1:4;
a=1i*w*tau(n);
x(n)=(del(n)/(1+a^(1-alf(n))));
y=y+x(n);
end;
```

```
eps=8.854*10^-12;
relcartilage(i)=e+y+(sig/(1i*w*eps));
%relative permittivity of lung%
e=2.5;
del(1)=18;
tau(1)=7.958*10^-12;
alf(1)=0.1;
del(2)=500;
tau(2)=63.662*10^-9;
alf(2)=0.1;
sig=0.03;
del(3)=2.5*10^5;
tau(3)=159.155*10^-6;
alf(3)=0.2;
del(4)=4*10^7;
tau(4)=7.958*10^-3;
alf(4)=0;
y=0;
for n=1:4;
a=1i*w*tau(n);
x(n)=(del(n)/(1+a^(1-alf(n))));
y=y+x(n);
end;
eps=8.854*10^-12;
rellung(i)=e+y+(sig/(1i*w*eps));
%relative permittivity of heart%
e=4;
del(1)=50;
tau(1)=7.958*10^-12;
alf(1)=0.1;
del(2)=1200;
tau(2)=159.155*10^-9;
alf(2)=0.05;
sig=0.05;
del(3)=4.5*10^5;
tau(3)=72.343*10^-6;
alf(3)=0.220;
del(4)=2.5*10^7;
tau(4)=4.547*10^-3;
alf(4)=0;
y=0;
for n=1:4;
a=1i*w*tau(n);
x(n)=(del(n)/(1+a^(1-alf(n))));
y=y+x(n);
end;
eps=8.854*10^-12;
relheart(i)=e+y+(sig/(1i*w*eps));

i=i+1
end
c=299795637.7;
d=[1.5*10^-3;9.6*10^-3;13.5*10^-3;11.6*10^-3;5.78*10^-3;8*10^-3] % Thickness of tissue layer
for i=1
    etaskin(i)=(120*pi)./sqrt(relskin(i)) ;% Complex impedance of Skin
    etafat(i)=(120*pi)./sqrt(relfat(i)) ;% Complex impedance of Fat
```

```
    etamuscle(i)=(120*pi)./sqrt(relmuscle(i)) ;% Complex impedance of Muscle
    etacartilage(i)=(120*pi)./sqrt(relcartilage(i)) ;% Complex impedance of Cartilage
    etalung(i)=(120*pi)./sqrt(rellung(i)) ;% Complex impedance of Lung
    etaheart(i)=(120*pi)./sqrt(relheart(i)) ;% Complex impedance of Heart
    skins(i)=1i*w*(sqrt(relskin(i))./c);  % complex propagation constant of Skin
    fats(i)=1i*w*(sqrt(relfat(i))./c);% complex propagation constant of Fat
    muscles(i)=1i*w*(sqrt(relmuscle(i))./c);% complex propagation constant of Muscle
    cartilages(i)=1i*w*(sqrt(relcartilage(i))./c);% complex propagation constant of Cartilage
    lungs(i)=1i*w*(sqrt(rellung(i))./c);% complex propagation constant of Lung
    hearts(i)=1i*w*(sqrt(relheart(i))./c);% complex propagation constant of Heart
end
for i=1
    % ABCB parameters of transmission matrix
    Askin(i)=cosh(skins(i).*d(1));
    Bskin(i)=etaskin(i)*sinh(skins(i).*d(1));
    Cskin(i)=(sinh(skins(i).*d(1))/etaskin(i));
    Dskin(i)=cosh(skins(i).*d(1));

    Afat(i)=cosh(fats(i).*d(2));
    Bfat(i)=etafat(i)*sinh(fats(i).*d(2));
    Cfat(i)=(sinh(fats(i).*d(2))/etafat(i));
    Dfat(i)=cosh(fats(i).*d(2));

    Amuscle(i)=cosh(muscles(i).*d(3));
    Bmuscle(i)=etamuscle(i)*sinh(muscles(i).*d(3));
    Cmuscle(i)=(sinh(muscles(i).*d(3))/etamuscle(i));
    Dmuscle(i)=cosh(muscles(i).*d(3));

    Acartilage(i)=cosh(cartilages(i).*d(4));
    Bcartilage(i)=etacartilage(i)*sinh(cartilages(i).*d(4));
    Ccartilage(i)=(sinh(cartilages(i).*d(4))/etacartilage(i));
    Dcartilage(i)=cosh(cartilages(i).*d(4));

     Alung(i)=cosh(lungs(i).*d(5));
    Blung(i)=etalung(i)*sinh(lungs(i).*d(5));
    Clung(i)=(sinh(lungs(i).*d(5))/etalung(i));
    Dlung(i)=cosh(lungs(i).*d(5));

     Aheart(i)=cosh(hearts(i).*d(6));
    Bheart(i)=etaheart(i)*sinh(hearts(i).*d(6));
    Cheart(i)=(sinh(hearts(i).*d(6))/etaheart(i));
    Dheart(i)=cosh(hearts(i).*d(6));
end

for i=1
    % Transmission matrix of each tissue layer

T1=[Askin(i),Bskin(i);Cskin(i),Dskin(i)];
       T2=[Afat(i),Bfat(i);Cfat(i),Dfat(i)];
       T3=[Amuscle(i),Bmuscle(i);Cmuscle(i),Dmuscle(i)];
       T4=[Acartilage(i),Bcartilage(i);Ccartilage(i),Dcartilage(i)];
       T5=[Alung(i),Blung(i);Clung(i),Dlung(i)];
       T6=[Aheart(i),Bheart(i);Cheart(i),Dheart(i)];
       TB=T2*T3*T4;%LUNG IS LAST%
TC=T3*T4*T5;%HEART%
TD=T4*T5;
```

```
TE=T5;
TF=T6;
% refelction coefficient upto the depth
ETALB=((etalung(i).*TB(1,1))+TB(1,2))/((etalung(i)*TB(2,1))+TB(2,2));
ETALC=((etaheart(i).*TC(1,1))+TC(1,2))/((etaheart(i)*TC(2,1))+TC(2,2));
ETALD=((etaheart(i).*TD(1,1))+TD(1,2))/((etaheart(i)*TD(2,1))+TD(2,2));
ETALE=((etaheart(i).*TE(1,1))+TE(1,2))/((etaheart(i)*TE(2,1))+TE(2,2));
ETALF=etaheart(i);
%total power attenuation%
NUM=(2*sqrt(real(120*pi))*sqrt(real(ETALF)));
Ttotal=T1*T2*T3*T4*T5;
DEN=((ETALF*Ttotal(1,1))+Ttotal(1,2)+(120*pi*ETALF*Ttotal(2,1))+(120*pi*Ttotal(2,2)));
totalpowerattenuation=(abs(NUM/DEN))^2;
TOTALdb=10*log10(totalpowerattenuation)

%power attenuation upto cartlage_lung interface%
NUM=(2*sqrt(real(120*pi))*sqrt(real(ETALE)));
Ttotal=T1*T2*T3*T4;
DEN=((ETALE*Ttotal(1,1))+Ttotal(1,2)+(120*pi*ETALE*Ttotal(2,1))+(120*pi*Ttotal(2,2)));
totalpowerattenuation1=(abs(NUM/DEN))^2;
cartilagelungdb=10*log10(totalpowerattenuation1)

%power attenuation upto muscle_cartlage interface%
NUM=(2*sqrt(real(120*pi))*sqrt(real(ETALD)));
Ttotal=T1*T2*T3;
DEN=((ETALD*Ttotal(1,1))+Ttotal(1,2)+(120*pi*ETALD*Ttotal(2,1))+(120*pi*Ttotal(2,2)));
totalpowerattenuation2=(abs(NUM/DEN))^2;
musclecartilagedb=10*log10(totalpowerattenuation2)

%power attenuation upto fat_muscle interface%
NUM=(2*sqrt(real(120*pi))*sqrt(real(ETALC)));
Ttotal=T1*T2;
DEN=((ETALC*Ttotal(1,1))+Ttotal(1,2)+(120*pi*ETALC*Ttotal(2,1))+(120*pi*Ttotal(2,2)));
totalpowerattenuation3=(abs(NUM/DEN))^2;
fatmuscledb=10*log10(totalpowerattenuation3)

%power attenuation upto skin_fat interface%
NUM=(2*sqrt(real(120*pi))*sqrt(real(ETALB)));
Ttotal=T1;
DEN=((ETALB*Ttotal(1,1))+Ttotal(1,2)+(120*pi*ETALB*Ttotal(2,1))+(120*pi*Ttotal(2,2)));
totalpowerattenuation4=(abs(NUM/DEN))^2;
skinfatdb=10*log10(totalpowerattenuation4)
end
```

REFERENCES/BIBLIOGRAPHY

[1] Statistics Canada. (2013). *Leading causes of death by sex (Both sexes),* [Online]. Available: http://www.statcan.gc.ca/tables-tableaux/sum-som/l01/cst01/hlth36a-eng.htm.

[2] Q. M. Murphy, “Radar tomography: a new concept in medical imaging,” *Annals of Dentistry*, Vol. *53*, no. *1*, pp. *5-14*, 1994.

[3] L. Fernandez *et al*., "Radio frequency power sensor based on MEMS technology with ultra low loss," *18th IEEE International Conference on Micro Electro Mechanical Systems*, 2005, pp. *191-194*.

[4] MaRS Market Insights. (2009). *Life sciences a bright future for diagnostic imaging in Ontario*. [Online]. Available: https://www.marsdd.com/mars-library/a-bright-future-for-diagnostic-imaging-in-ontario/.

[5] S. Semenov, “Microwave Tomography: Review of the Progress towards Clinical Applications,” *Philosph. Trans. Series A, Math., Phys, and Eng. Sci.,* vol. *367*, no.*1900*, pp. *3021–3042*, 2009.

[6] Northwell health. (2013). *North Shore University Hospital Unveils New 640-Slice CT Scanner; Offers Most Advanced Cardiac Imaging*. [Online]. Available: https://www.northwell.edu/about/news/north-shore-university-hospital-unveils-new-640-slice-ct-scanner-offers-most-advanced.

[7] Goel, *et al*. *High-resolution CT*, [Online]. Available: http: //radiopaedia.org/articles/high-resolution-ct.

[8] N. Savage, “The World's Most Powerful MRI Takes Shape,” *IEEE Spectrum*, Oct 2013, [Online]. Available: http: //spectrum.ieee.org/biomedical/imaging/the-worlds-most-powerful-mri-takes-shape.

[9] J. H. Kang, and J. Chung, “Molecular-genetic imaging based on reporter gene expression,” *J. Nucl. Med.,* Vol. *49*, no. *6*, Suppl. *2*, pp. *164S-179S*, Jun 2008.

[10] “First report and order, revision of part 15 of the commission’s rules regarding ultra wideband transmission systems,” FCC, Washington, DC, ET Docket 98-153, 2002.

[11] C. N. Paulson *et al.,* “Ultra-wideband Radar Methods and Techniques of Medical Sensing and Imaging,” *Smart Medical and Biomedical Sensor Technology III. Proc. of the SPIE*, Volume *6007*, pp. *96-107*, 2005.

[12] A. Vander Vorst *et al.,* “RF / Microwave Interaction with Biological Tissues,” *Wiley-IEEE Press*, New Jersey, 2006.

[13] J. D. Taylor, “Ultrawideband Radar Future Directions and Benefits,” *PIERS Proc.,* Stockholm, Sweden, Aug. 12-15, 2013, pp. *1575-1578.*

[14] L. Jofre, *et al.,* “UWB tomographic radar imaging of penetrable and impenetrable objects,” *Proc. IEEE*, vol. *97*, no*. 2*, pp. *451–464*, Feb. 2009.

[15] X. Wang, *et al.,* “Radar Sensing Using Ultra Wideband – Design and Implementation,” in *Ultra Wideband -Current Status and Future Trends*, Intech, 2012, Ch.*3*.

[16] S. Y. Semenov and D. R. Corfield, “Microwave Tomography for Brain Imaging: Feasibility Assessment for Stroke Detection,” *Int. J. of Antennas and Propagation*, vol. *2008*, Article ID 254830, 8 pages, 2008.

[17] J. Pan, “Medical Applications of Ultra-Wideband (UWB),” 2008, [Online]. Available: http://www1.cse.wustl.edu/~jain/cse574-08/ftp/uwb/index.html.

[18] Monroy Estrada, G. (2014). Relationship of blood pressure with the electrical signal of the heart using signal processing. TECCIENCIA, 9(17), 9-14.

[19] A. D. Droitcour, “Non-Contact Measurement of Heart and Respiration Rates with a Single-Chip Microwave Doppler Radar,” PhD. Dissertation, Stanford Unv., 2006.

[20] I. Immoreev and T.H. Tao, “UWB radar for patient monitoring,” *IEEE Aerosp. Electron. Syst. Mag.,* vol. *23*, no. *11*, pp. *11–18*, Nov. 2008.

[21] G. Peronnet, *et al.*, "A microwave diffraction tomography system for biomedical applications," in *13th European Microwave Conf. Proc.,* Nurnberg, West Germany, Sept. 5-6, 1983, pp*. 529-533.*

[22] ICNIRP, “Guidelines for limiting exposure to time-varying electric, magnetic, and electromagnetic fields (up to 300GHz),” *Health Physics*, vol. *74*, no. *4*, pp. *494–523*, 1998.

[23] J. SACHS, “Ultra-Wideband Sensing – An Overview,” in *Handbook of Ultra-Wideband Short-Range Sensing: Theory, Sensors, Applications*, 1st ed. Weinheim, Germany, Wiley, 2013.

[24] C. Gabriel, *et al.,* “The dielectric properties of biological tissues: I. literature survey,” *Physics in Medicine and Biology*, vol. *41*, 1996.

[25] Y.J Chang, “The NPAC Visible Human Viewer,”. Syracuse University, NY.

[26] C. Gabriel, “Compilation of the Dielectric Properties of Body Tissues at RF and Microwave Frequencies,” Physics Dpt., King's College London, London, UK, Tech. Rep. AL/OE-TR-1996-0004, Jan. 1996.

[27] Xia. X and Takamaro. K, "Study on the breast cancer detection by UWB microwave imaging," *2008 Int. Conf. on Microwave and Millimeter Wave Tech.*, Nanjing, 2008, pp. *1707-1710*.

[28] Bidhendi. H, *et al.,* (2014) Ultra-Wideband Imaging Systems for Breast Cancer Detection. In*: Yuce M. (eds) Ultra-Wideband and 60 GHz Communications for Biomedical Applications. Springer*, Boston, MA.

[29] I. Gresham *et al*., “Ultra-wideband radar sensors for short-range vehicular applications,” in *IEEE Trans. on Microwave Theory and Techniques*, vol. 52, no. 9,

pp. 2105-2122, Sept. 2004.

[30] L. Lionet (2013, June 11). *Magnetic Loop Antenna Theory* [Online]. Available https://sidstation.loudet.org/antenna-theory-en.xhtml.

[31] H. Nieminen *et al*., “Microelectromechanical capacitors for RF applications”, *Journal of Micromechanics and Microengineering*, vol.12, no. 2, pp. 177-186, 2002.

[32] D. Balasubramanyam, *et al*., “Form Bandpass Filters On Glass Substrates”, Microwaves and Rf, vol. 48,,2009.

[33] R. Manwar, *et al*., “Fabrication and characterization of a high frequency and high coupling coefficient CMUT array”, Microsystem Technologies, 2016, pp. *1-13*.

[34] M. Rahman, *et al*., “An improved analytical method to design CMUTs with square diaphragms”, *IEEE Transactions on Ultrasonics, Ferroelectrics, and Frequency Control*, vol. *60*, no. *4*, pp. *834-845*, April 2013.

[35] E. M. Staderini, "UWB radars in medicine," in *IEEE Aerospace and Electronic Systems Magazine*, vol. *17*, no.*1*, pp. *13-18*, Jan 2002.

[36] P. T. Theilmann1, *et al*., “Computationally Efficient Model for UWB Signal Attenuation due to Propagation in Tissue for Biomedical Implants,” *Progress In Electromagnetics Research B*, Vol. *38*, pp. *1–22*, 2012.

[37] M. Ketata, *et al*., "The Attenuation Calculation of the Energy Signal of a Gaussian Pulse Propagating in the Human Body to Detect the Heart Beat", *International Review on Modelling and Simulations (I.RE.MO.S)*, vol. *6*, no. *3*, pp. *937-945*, June 2013.

[38] C. G. Bilich, "Bio-Medical Sensing using Ultra Wideband Communications and Radar Technology: A Feasibility Study," *2006 Pervasive Health Conference and Workshops*, Innsbruck, 2006, pp.*1-9*. doi: 10.1109/PCTHEALTH.2006.361671.

[39] B. R. Mahafza, “Radar Cross Section”, in *Radar Systems Analysis and Design*

Using MATLAB, 2nd ed. Huntsville, AL, CRC press, 2000, sec. 2.5.

[40] Levkov C. L. (2011, June 13). *Wideband Active Small Magnetic Loop Antenna* [Online]. Available http://www.lz1aq.signacor.com/docs /wsml/wideband-active-sm-loop-antenna.htm.

[41] J. Shim *et al.,* "Nanocrystalline Fe–Co–Ni–B thin film with high permeability and high-frequency characteristics," *J. of Magnetism and Magnetic Materials*, vol. *290,* pp*. 205-208,* 2005.

[42] N. Y. Sutri, *et al*., "A monolithic, low-noise, capacitive readout interface circuit for CMOS-MEMS resonator-based gravimetric chemical gas sensors," *AFRICON 2015*, Addis Ababa, 2015, pp. 1-7.

[43] J. Perez Sanjurjo, *et al.,* "A Capacitance-To-Digital converter for MEMS sensors for smart applications," *sensors (Basel)*, vol. 17, no. 6, p. 1312, July 2017.

[44] T. Yin, *et al.,* "A low-noise readout circuit for MEMS vibratory gyroscope," *2008 3rd IEEE International Conference on Nano/Micro Engineered and Molecular Systems,* Sanya, 2008, pp. *124-127*.

[45] J. Shiah, *et al.,* "A low-noise parasitic insensitive switched-capacitor CMOS interface circuit for MEMS capacitive sensors," in *New Circuits and Systems Conference (NEWCAS), 2011 IEEE 9th International*, 2011, pp. *470-473*.

[46] F. Gozzini, *et al.,* "An instrument-on-chip for impedance measurements on nanobiosensors with attoFarad resolution" in *International Solid-State Circuits Conference Digest of Technical Papers*, San Francisco, CA, 2009; pp. *346–347*.

[47] M. Bachman, "Cleaning procedures for glass substrates.",1999 Available: http://sharepoint.creol.ucf.edu/ebeam/Shared%20Documents/Standard%20Operating%20Procedures%20(Univ.%20of%20California,%20Irvine)/glass-cleaning.pdf.

[48] Amy. P, "Minimization of the surface roughness of gold films for Casimir force

measurements," Chan Lab, University of Florida, Aug. 2006.

[49] W. Derwin, "Reactive Ion Etching of PECVD Silicon Dioxide (SiO_2) Layer for MEMS Application," Army research laboratory, Adelphi, MD, Tech. Rep. ARL-TR-3269, July 2004.

[50] Park. H, et al., "Inductively coupled plasma etching of Ta, Co, Fe, NiFe, NiFeCo, and MnNi with Cl2/Ar," *In Korean Journal of Chemical Engineering*, Vol. *21*, No*. 6*, pp. *1235-1239*, 2014.

[51] A. Bakhtazad, *et.al.*, "Fabrication and characterization of sealed cavities realized by adhesive wafer bonding with dry etched Cyclotene™," *Microsystem Technologies*, pp. *2435-2442*, 2015.

VITA AUCTORIS

NAME:	Sujitha Vejella
PLACE OF BIRTH:	Andhra Pradesh, India
YEAR OF BIRTH:	1992
EDUCATION:	Bachelor of Technology, Electrical and Electronics Engineering, Shri Vishnu Engineering College, AP, India, 2014. Master of Science in ECE, University of Windsor, Windsor, Ontario, Canada, 2017.